İSTANBUL TECHNICAL UNIVERSITY ★ INSTITUTE OF SCIENCE AND TECHNOLOGY

MECHANICAL BEHAVIOR OF MATERIALS UNDER HIGH STRAIN RATE

M.Sc. Thesis by
Mech. Eng. Emre ÖZLÜ
(503011098)

Date of submission: 30 June 2003

Date of defence examination: 30 May 2003

Supervisor (Chairman): Prof. Dr. Mehmet DEMİRKOL

Members of the Examining Committee: Prof. Dr. Zahit MECİTOĞLU

Assoc. Prof. Erol ŞENOCAK

JUNE 2003

ISTANBUL TECHNICAL UNIVERSITY ★ INSTITUTE OF SCIENCE AND TECHNOLOGY

DYNAMICAL BEHAVIOR OF MATERIALS UNDER HIGH STRAIN RATE

M.Sc. Thesis by
Mech. Eng. Emre ÖZLÜ
(503011098)

Department: Mechanical Engineering
Programme: Manufacturing

Supervisor: Prof. Mehmet DEMİRKOL

JUNE 2003

ACKNOWLEDGEMENTS

I would like to express my gratitude to my thesis supervisor Prof. Mehmet Demirkol, for his support and guidance throughout the study.

I would also like to thank the following people for their technical support. The discussions with Prof. Ahmet Aran and Assoc. Prof. Erol Şenocak were invaluable. Further, I would like to thank Hakan Tanrıöver for his advises, literature support and patience for my visits and questions.

Finally, I would like to express my grateful thanks, howsoever formal it may appear, my mother and father for their moral support and encouragement.

TABLE OF CONTENTS

LIST OF TABLES

LIST OF FIGURES

Page No

NOTATION

A, B, C	Johnson-Cook material deformation model constants
D_1, D_2, D_3, D_4, D_5	Johnson-Cook material fracture model constants
E_b	Modulus of Elasticity of pressure bars
$E_{specimen}$	Modulus of Elasticity of specimen
E_{sb}	Modulus of Elasticity of striker bar
m	Strain rate sensitivity
n	Strain hardening exponent
S_1, S_2, S_3, γ_0	Mie-Gruneisen constants
$\varepsilon_I(t)$	input bar incident strain
$\varepsilon_R(t)$	input bar reflected strain
$\varepsilon_T(t)$	transmitted strain
ν	Poisson's Ratio

MALZEMELERİN YÜKSEK DEFORMASYON HIZLARINDAKİ DAVRANIŞLARI

ÖZET

Bu çalışmanın amacı, malzemelerin yüksek şekil değişimi hızlarındaki davranışlarının modellenmesi için bir metodoloji oluşturulması ve elde edilen bu davranış modelinin balistik bir penetrasyon modeli üzerinde uygulanmasıdır.

Bilindiği gibi, malzemelerin davranışları, uygulanan deformasyonun hızına bağlı olarak değişir. Katıya kuvvetin uygulandığı zamanla, katının dengeye ulaştığı zaman arasındaki süre kısa ise, deformasyon statik kabul edilebilir. Yani kuvvet uygulandıktan, denge oluşuncaya kadar geçen dürede katı her ''t'' anında dengede kabul edilir. Fakat, deformasyon hızı yüksekse, oluşan gerilme aynı anda bütün parçada hissedilemez. Katının bir bölümü deformasyona uğrarken, başka bir bölümü gerilmeyi henüz hissetmez. Bu durumda oluşan dinamik deformasyon, parçada dalgalar halinde yayılır. Bunlara gerilme dalgaları denir. Elastik, plastik ve şok dalgaları olmak üzere üç tip gerilme dalgası vardır. Elastik dalga teorisi, özellikle bir boyutlu elastik dalga yayılımı konusu, oldukça iyi anlaşılmıştır. Fakat plastik dalgalar, malzemelerin şekil değişim hızına geçmişine bağımlılığından dolayı oldukça güç modellenebilmektedir. Şok dalgaları bu tezin konusu içinde yer almamaktadır.

Şekil değişim hızı, kristal kafesteki deformasyon mekanizmalarını da etkilemektedir. Düşük şekil değişimi hızlarında ve yüksek sıcaklıklarda, uzun aralıklı engeller baskındır. Bu engeller ısıl aktivasyonla aşılamadığından, ısıl-olmayan aktivasyon mekanizması bu aralıktaki deformasyondan sorumludur. Bu aralıkta akma gerilmesi sıcaklık ve şekil değişimi hızından bağımsızdır. Yüksek şekil değişim hızlarında ve daha düşük sıcaklıklarda, kısa-aralıklı engeller ön plana çıkar ve dislokasyonlar ısıl aktivasyonla bu mekanizmaları geçebilirler. Bu aralıkta akma gerilmesi sıcaklık ve şekil değişim hızından etkilenir. Daha yüksek şekil değişim hızlarında ($<3500\ s^{-1}$), ''phonon''ların ve elektronların dislokasyonlarla olan etkileşimleri deformasyonu etkiler. Buna ''phonon sürüklenmesi'' adı verilmektedir. Bu aralıkta akma gerilmesi şekil değişim hızıyla alineer ve oldukça fazla bir artış göstermektedir.

Dislokasyon dinamiği yardımıyla, uygulanan kuvvet karşısında malzemenin gösterdiği davranış matematiksel olarak modellenebilir. Bu modellere bünye denklemleri denir. Bu şekilde elde edilen bünye denklemlerine fiziksel-tabanlı bünye denklemleri adı verilir. Zerilli-Armstrong modeli bu tip bir deformasyon modelidir. Diğer tip bünye denklemleri ampirik bünye denklemleridir. Bu tip denklemlerin çıkarılımında, eldeki verilerin bir denkleme uydurulması amaçtır. Johnson-Cook modeli bu tipe bir örnektir.

Malzemeleri yüksek deformasyon hızlarında test etmek için bir çok metod vardır. Fakat, bu metodların hiç biri henüz standart hale gelmemiştir. Diğerlerinin içinde ''split Hopkinson pressure bar (SHPB)'' deneyi üzerinde en çok çalışılmış olanıdır. Bu deneyde numune iki uzun çubuğun arasına sıkıştırılır. Bir gaz tabancasıyla ateşlenen vurucu bir çubuk, giriş çubuğuna çarptırılarak giriş dalgası yaratılır. Bu elastik giriş dalgası giriş çubuğu boyunca yayılır ve numuneye geldiğinde bir kısmı yansır bir kısmı ilerlemeye devem eder. Bu dalgalar giriş ve çıkış çubuklarına yerleştirilen strain gage'ler yardımıyla ölçülebilir. Burada dikkat edilmesi gereken nokta, sadece numunenin plastik şekil değişimine uğradığıdır. Bu ölçülen verilerle malzemenin gerilme-birim şekil değişimi diyagramı elde edilebilir. SHPB deneyi tek boyutlu elastik dalga yayılımı üzerine kurulmuştur. Deney sırasında bu durum

sağlanmalıdır. Ayrıca numune uniform deformasyon sağlanması ikinci bir zorunluluktur.

Çalışmada metaller için, gerekli varsayımlar ve tasarım kriterleri göz önüne alınarak , bir SHPB deney standı tasarımı yapılmıştır. Sonra bir SHPB çıktısından gerilme-birim şekil değişimi diyagramının nasıl elde edildiği gösterilmiştir. Çeşitli sıcaklık ve şekil değişim hızlarında elde edilen veriler (bu veriler bir makaleden alınmıştır) lineer-olmayan regresyon analizi kullanılarak Johnson-Cook modeline uydurulmuş ve sabitler elde edilmiştir. Ölçülen ve Johnson-Cook modeliyle belirlenen akma gerilmeleri oldukça yakın sonuçlar vermiştir.

DYNAMICAL BEHAVIOR OF MATERIALS UNDER HIGH STRAIN RATE

SUMMARY

The aim of this thesis is to search a methoddology to model the high-strain rate response of metallic materials and application of the obtained model in a case study, namely ballistic penetration problem.

It is known that, when the rate of deformation increases the behavior of materials is changed considerably. If the time between the applied load and the equilibration of the solid is relatively short, then the deformation can be considered as quasi-static and it is known that the solid is in equilibrium at every time stept during deformation. However when the rate of deformation increases the whole body cannot sense the stress at the same time. While one portion felt the stress, another portion is still in its initial equilibrium. Dynamic deformation in the solid propagates as a wave. These waves are called stress waves. There are three types of stress waves, namely elastic, plastic and shock waves. The theory of elastic waves is well understood (particularly one-dimensional elastic wave propagation), however the theory of plastic wave propagation is relatively difficult to construct a model and understand fully due to strain rate history dependence of the materials.

The deformation mechanisms in the lattice also depend on strain rate. At low strain rates and relatively high temperatures long-range barriers become important, since these barriers can't be overcome by thermal activation. The athermal activation mechanisms are responsible in this range and the flow stress is independent of strain rate and temperature. At high strain rates and lower temperatures short-range barriers are the dominant barriers. In this case dislocation can overcome this barriers and the flow stress is dependent on strain rate and temperature due to thermal activation. At higher strain rates (i.e. higher than 3500 s^{-1}), the interaction of phonons and electrons with dislocations affects the deformation, which is called phonon drag. In this range dramatic and linear increase of the flow stress with the strain rate is observed.

With the help of dislocation dynamics, the behavior of materials under applied loads can be modeled mathematically and they are generally called as constitutive equations. This type of constitutive equations is known as physically-based constitutive equations. Zerilli-Armstrong model can be a good example for this type of constitutive equations. Other type of the constitutive equations is empirical constitutive equations. The development of this type of constitutive equations depends on fitting the data to the material behavior. A good example of this type is Johnson-Cook model.

There are several mechanical testing method applicable at high rates of strains. None of them has been standardized yet. Among the others Split Hopkinson Pressure Bar (SHPB) is the most studied and developed one. In SHPB test the specimen is sandwiched between to pressure bars. The incident wave is generated by a propelled striker bar with a gas gun. When the striker bar hits the specimen an elastic incident wave propagates through the bar. When the wave meets specimen, one part is reflected and the other is transmitted. The magnitude of transmitted and reflected waves can be measured by strain gages attached on the bars. In SHPB testing only the specimen is being deformed plastically. By using the measured properties of reflected and transmitted waves, the stress-strain diagram of the

material can be obtained. SHPB experiment depends on one-dimensional elastic wave propagation. So during the test this situation should be ensured. Also uniform deformation of the specimen is very important for obtaining true results.

A SHPB apparatus for metals was designed ensuring assumptions and design criteria. The construction of SHPB test system could not be realized. But using the methodology in determining stress-strain diagram from SHPB test and the data which is available in the literature, Johnson-Cook deformation model was tested by using non-linear regression analysis. A good agreement was found between the measured and predicted flow stresses of metallic materials.

1. OBJECTIVE

The objective of this study is to design a methodology to model the behavior of materials under high deformation rates and application of this data. Below the steps to reach the goals can be seen

- Design of an experiment to test materials at high rates of strain.
- Obtain stress strain diagram at a specific temperature and strain rate.
- Obtain the constitutive deformation model for the material testing.
- Numerical solution of a ballistic penetration problem using the obtained constitutive equation.

2. INTRODUCTION: DEFORMATION AND WAVES

The dynamic behavior of materials is an area of study in many scientific fields. When the materials are subjected to rapidly changing loads, the behavior can differ from those under static or quasi-static situations. An illustrative example can be the behavior of a sand bag, which was usually used at wars, on different situations. Soft, free-flowing sand is effective against impacts of a velocity on the order of 1500 m/s. On the other hand, a simple knife can defeat the sand bag. But, a solid wood or steel enclosure, if not excessively thick, can easily be perforated by a bullet, where a knife would never penetrate them. In Figure 2.1 schematic description of the scientific fields that are of importance in the study of dynamic processes can be seen.

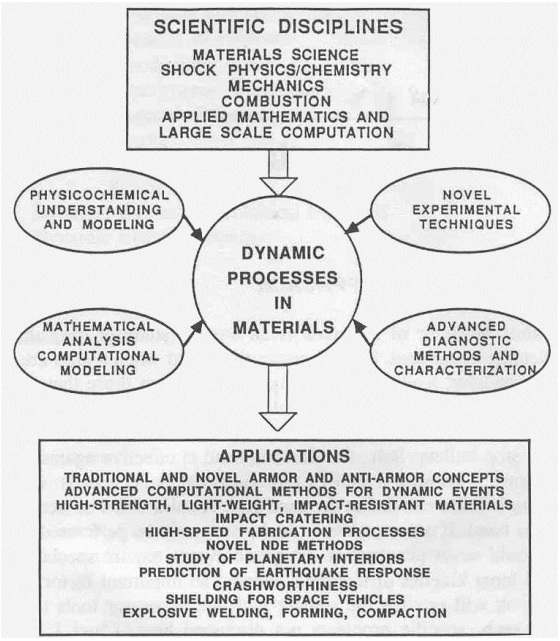

Figure 2.1 Schematic representation of the contributing sciences (disciplines) and principal applications of dynamic processes in materials

In dynamic events, inertia and inner kinetics of materials become an important factor. In all applications, the simple equation relating the kinetic energy with the velocity of a mass is of paramount importance:

$$E_c = \frac{1}{2} m v^2 \qquad (2.1)$$

The kinetic energy of a mass increases with the square of its velocity. The energy delivered by an object of mass m to a target can be expressed as

$$dE = Fdl \tag{2.2}$$

where dl is the length over which this force F will act. This kinetic energy is transformed into damage in projectile and target.

Another concept, which is very important, is that the fundamental difference between static (or quasi-static) and dynamic deformation. In quasi-static deformation, at any time, static equilibrium is satisfied, namely, any point in the body has a summation of forces acting on it close to zero. When the deformation is applied at a very high rate, one portion of the body is stressed while other portion has not experienced this stress yet. In other words, stress has to travel through the body. Stress and its associated strain or deformation travels in bodies at specified velocities (depends on material properties which will be detailed later). These are called **waves**, since they have usually well-established velocities. Thus, dynamic deformation often involves wave propagation, whereas quasi-static deformation can be considered as a sequence of states of equilibrium that can be treated by the well-known equations of mechanics of materials (summation of forces equal to zero; summation of moments equal to zero; compatibility of strains, constitutive relations)[1].

As a sum up, in rigid dynamics it is assumed that, when a force is applied to any one point on a body, the resultant stresses set every other point in motion instantaneously, and the force can be considered as producing linear acceleration of the whole body. In the theory of elasticity, on the other hand, the body is considered as in equilibrium under the action of applied forces, and the elastic deformations are assumed to have reached their static values. These treatments are sufficiently accurate for problems in which the time between applied force and the setting up of equilibrium is short compared with the observation time.

However, when dealing with the forces, which are applied for only very short periods of time, or are changing rapidly, the effect must be considered in terms of the propagation of *stress waves*. Mainly, there are three types of stress waves that are described below[1, 2]

2.1. Elastic Waves

2.1.1. Lattice dynamics

The application of an external force to a body is, by definition, a dynamic process. However, when the rate of change of the applied forces is slow, one can consider the process of deformation as a sequence of steps in which the body can be considered in static equilibrium as described above. Figure 2.2(a) shows how the distance between atoms changes upon the application of an external force. For each stages of deformation shown in Figures 2.2 (b) and (c), the body can be considered under static equilibrium and the methods of mechanics of materials can be applied to determine the internally resisting stresses. Hence, a section made at AA or BB will yield identical stresses.

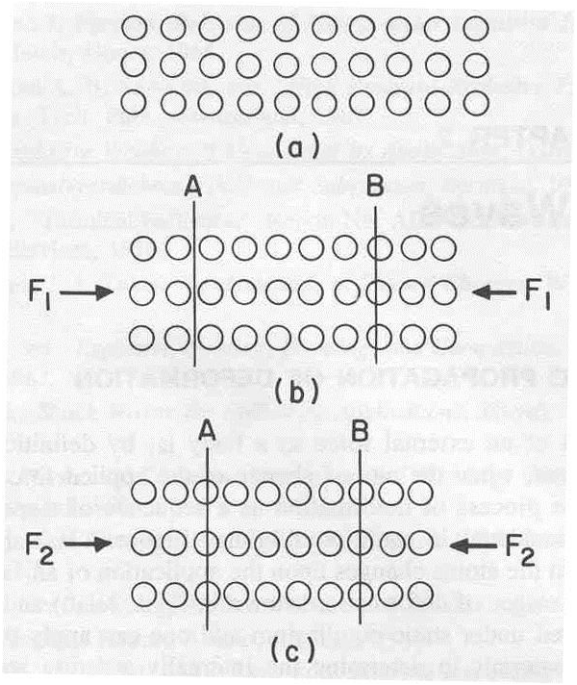

Figure 2.2 Quasi-static elastic deformation of a simple two-dimensional array of atoms ($F_2 > F_1$).

However, the internal stresses are not instantaneously transmitted from the force application region to the different regions of the body. The stresses (and strains) are transferred from atom to atom at a certain specific velocity. Figure 2.3 shows the application of a force at a rate dF/dt such that the stresses (and attendant strains) vary from section to section. While section BB has effected from the applied force at time t, section AA has already effected from external force F.

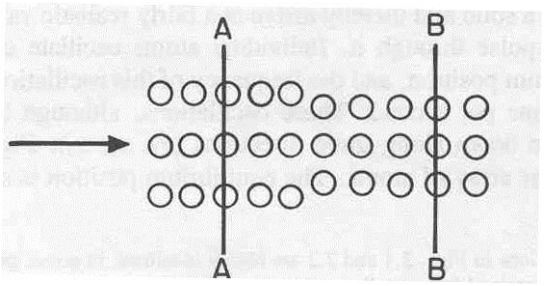

Figure 2.3 Dynamic elastic deformation of an idealized array of atoms

At an atomistic level, the wave can be defined as the succession of impacts between adjacent atoms. Each atom, upon being accelerated to a certain velocity, transmits all of its momentum to its neighbors.

Individual atoms oscillate continuously about their equilibrium position, and the frequency of this oscillation is approximately 10^{13} oscillations per second. These oscillations, although three dimensional, can be broken down along three dimensions. Figure 2.4 shows an idealized array of atoms. The equilibrium position is shown by the solid lines, and the extreme positions along the three axes are shown by dashed lines. This field of study is called **lattice dynamics** and the oscillations are not independent, but are coupled in waves called **phonons**. Thus when the atom is impacted on the left, this atom will transmit this impact to its neighbor on the right.

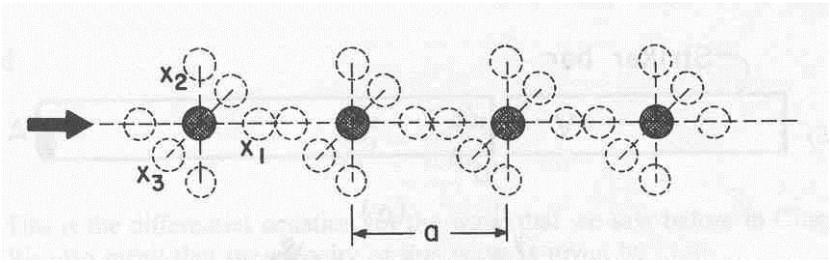

Figure 2.4 Transmission of disturbance from atom to atom

All wave propagation equations can be derived by assuming that the material is a continuum (mass uniformly distributed in space), since they are direct consequence of Newton's second law. Nevertheless, these atoms are connected by interatomic forces that can be assumed as minute spring connecting spheres (atoms). Momentum is transferred from sphere to sphere at a rate that provides the velocity of propagation of disturbances.

When the force on the left is applied, there will be a time lag involved in the transmission of this push equal in average to the period of vibration (10^{-13} s). The atoms in the middle will continue the process, transmitting the disturbance to the

atom on the right. If the distance between two atoms is known, the order of magnitude of velocity can be derived. For a solid metal (iron) it can be taken approximately 3 A (or $3x10^{-10}$ m). Thus,

$$V = \frac{a}{t} = 3x10^{-10}\,x10^{13} = 3x10^{3}\,m/s$$

This is very close to the velocity of propagation of an elastic wave in iron (3500 m/s). This simple reasoning explains the physical sequence of momentum transfer at the atomic level. [1]

2.1.2. The velocity of the elastic wave in cylindrical bar

Figure 2.5 shows a striker bar impacting a long cylindrical bar at velocity V. A compressive stress wave is produced in the bar that travels from left to right. At time t the front of this disturbance is at x. Strains and inertia along the direction transverse to the bar Oy is neglected. Firstly consider a section AB and A'B at the front of the wave at time t. The section A'B is distant $x + \delta x$ from the origin. Applying Newton's second law to AA'B B we obtain:

$$F = ma \tag{2.3}$$

$$\left[A\sigma - A\left(\sigma + \frac{\partial \sigma}{\partial x}\delta x\right)\right] = A\rho\delta x\frac{\partial^2 u}{\partial t^2} \tag{2.4}$$

$$\frac{\partial \sigma}{\partial x} = \rho\frac{\partial^2 u}{\partial t^2} \tag{2.5}$$

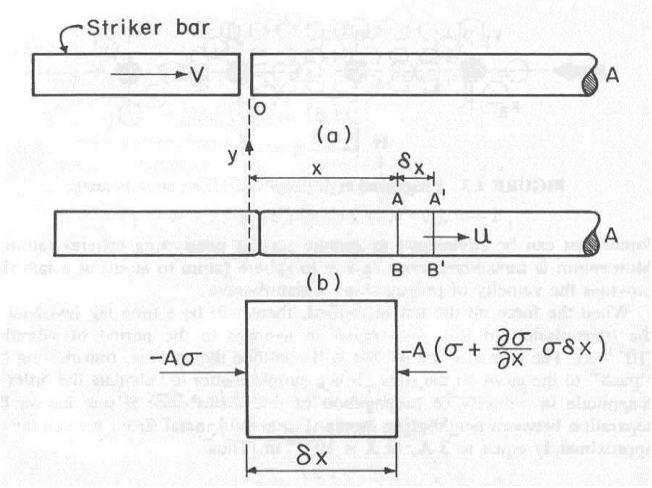

Figure 2.5 Propagation of wave in bar produced by impact of striker bar (a) prior to impact and (b) after impact

Since the deformation is elastic, assuming Hooke's law to hold:

$$\frac{\sigma}{\varepsilon} = E \tag{26}$$

where ε is the strain, defined as $\partial u / \partial x$. The minus sign is due to the compressive strain. Thus,

$$\frac{\partial}{\partial x}\left(E \frac{\partial u}{\partial x} \right) = \rho \frac{\partial^2 u}{\partial t^2} \tag{27}$$

and

$$\frac{\partial^2 u}{\partial t^2} = \frac{E}{\rho} \frac{\partial^2 u}{\partial x^2} \tag{28}$$

This is the general differential equation for the wave. The velocity of this wave in this situation is given by;

$$C_0 = \sqrt{\frac{E}{\rho}} \tag{29}$$

It should be noted that an elastic dilatational wave in an unbounded medium travels at a velocity slightly higher than C_0. For a metal with $\upsilon = 0.3$, this wave velocity is $1.2 C_0$.

The propagation of elastic waves in cylindrical bars is very important for the analysis of Hopkinson bar experiments. When a cylindrical bar impacted with a cylindrical projectile of length L, a rectangular pulse of length $2L$ propagating through the bar is expected if the bar and projectile are of the same material. This is shown schematically in Figure 2.6. The impact produces compressive waves propagating at velocities C_0 into projectile and target. As the compressive wave reaches the end of the projectile, it reflects back. This determines the length of the pulse, $\Lambda = 2L$. The velocity of the interface, equal to the partide velocity, can be calculated from the conservation of momentum equation (momentum prior to impact equals momentum after impact):

Prior to impact: $\rho_0 A_0 L V$

After impact: $\rho_0 A_0 L \Lambda U_p = 2\rho_0 A_0 L U_p$

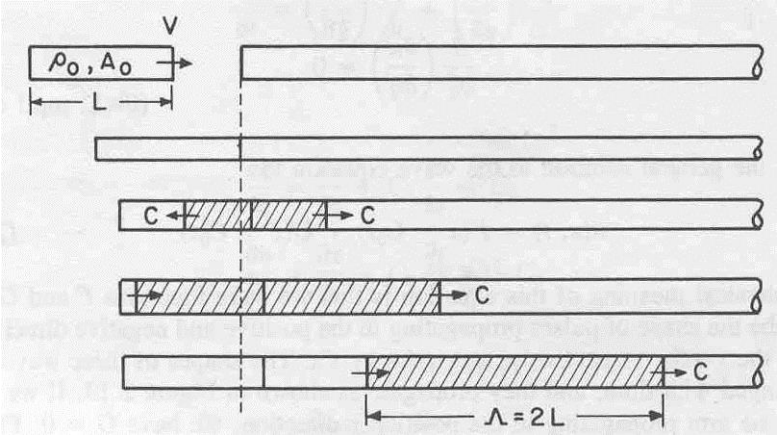

Figure 2.6 Cylindrical projectile impacting cylindrical bar.

Thus,

$$U_p = \frac{V}{2}$$

The stresses generated by the impact at a velocity V is given by $\sigma = \rho C U_p$; substituting the upper equation yields

$$\sigma = \frac{1}{2}\rho C V \qquad (2.10)$$

The expected pulse shape is rectangular, with duration (at a fixed point) of $2L/C$. Gages placed on the cylinder surface allows obtaining reliable records of the stress pulses.[1]

2.1.3. Types of elastic waves

Different types of elastic waves can propagate in solids, depending on how the motion of the particles of the solid is related to the direction of propagation of the waves themselves and on the boundary conditions. The most common types of elastic waves in solids are;

a) *Longitudinal (or irrotational) Waves:* In finite and semi-infinite media, they are also known as ''dilatational'' waves. These waves correspond to the motion of

the particles back and forth along the direction of wave propagation such that the particle velocity (U_p) is parallel to the wave velocity (U). If the wave is compressive, they have the same sense; if it is tensile, they have opposite senses. An example of a longitudinal elastic wave is illustrated in Figure 2.7(a). This wave is produced by the impact of a hammer on the left-hand side of the long cylinder. Equation 2.9 gives the velocity of the wave. Figure 2.7 (b) shows, schematically, the impact of a hammer on a semi-infinite body.

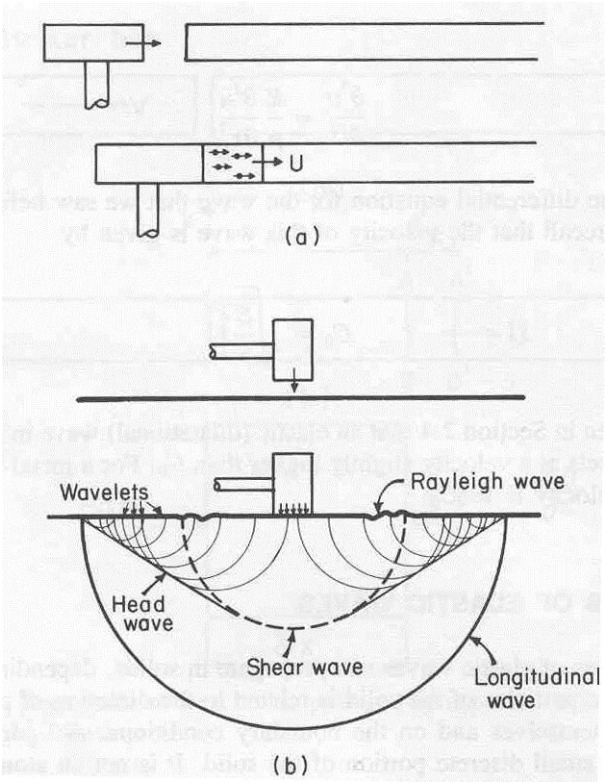

Figure 2.7 (a) Hammer impacting slender body; (b) hammer impacting semi-infinite body; notice formation of longitudinal, shear, and Rayleigh waves. Interaction of longitudinal wave with free-surface forms wavelets that comprise head wave [1].

b) *Distortional (or shear) Waves:* If the motions of the particles conveying the wave are perpendicular to the direction of the propagation of the wave itself, then a distortional wave occurs. All longitudinal strains (ε_{11}, ε_{22} and ε_{33}) are zero. An example of distortional wave is illustrated in Figure 2.8. When a bar is subjected to a torsional distortion, the region between the end and the clamp will store elastic energy. Upon release of the clamp, a pulse will travel in the bar, toward the right. This is a distortional wave, and the particle is perpendicular to the wave propagation direction (U_p is perpendicular to U).

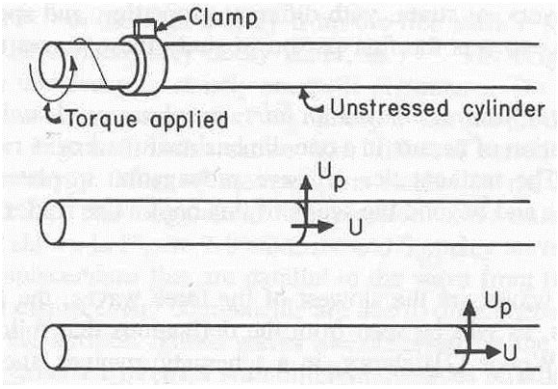

Figure 2.8 Wave and particle motion in release of torsional energy; when clamp is released, particle displacement (on cross-sectional plane) travels along longitudinal axis [1].

c) Surface Waves: Surface waves are analogous to waves on the surface of water. Objects floating on the water act as markers for the particles of water and move both up and down and back and forth, tracing out elliptical paths as the water moves by. This type of wave is restricted to the region adjacent to the surface, and particle velocity decreases very rapidly (exponentially) as one moves away from it. The particles describe elliptical trajectories. Surface waves (called Rayleigh waves in solids) are a particular case of interfacial waves when one of the materials has negligible density and elastic wave velocity.

d) Interfacial (Stoneley) Waves: When two semi-infinite media with different properties are in contact, special waves form at their interface.

The surface waves are the slowest of the three waves; the fastest are longitudinal waves Figure 2.9 shows, in a schematic manner, the amplitudes of the longitudinal, shear, and Rayleigh waves in half space. The shear wave undergoes a change in particle motion sense; at a point vertically below the load application region this particle velocity and, consequently, the shear wave amplitude are zero. The horizontal and vertical components of the particle motions as a function of distance from the surface in the Rayleigh wave are also shown. The exponential decay of the horizontal component, on the right side, is clearly seen. Also the waves decay at different rates.

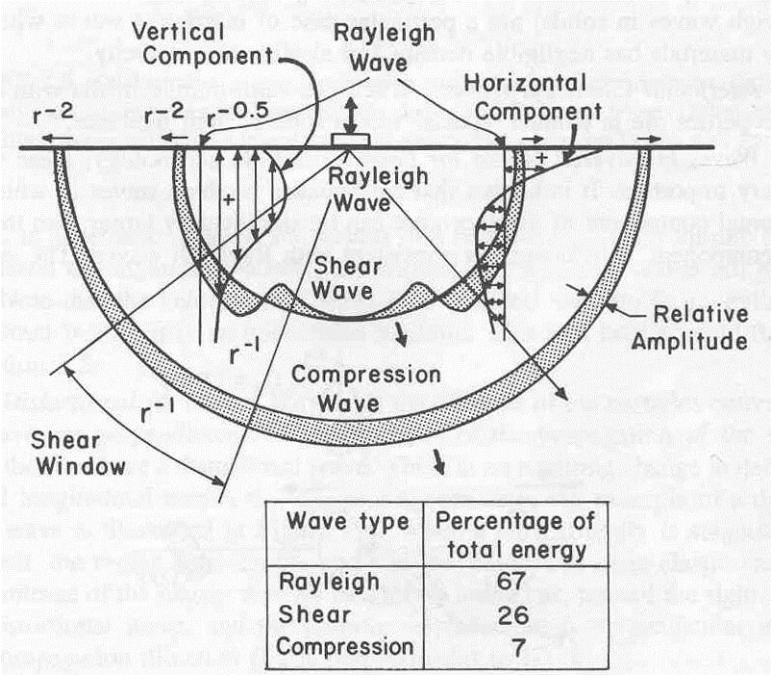

Figure 2.9 Distribution of displacement and energy in dilatational, shear, and surface waves from a harmonic normal load on a half-space of υ=0.25 [1].

2.2 Plastic Waves

When the stress in a ductile material exceeds the elastic limit, plastic deformation sets in. This occurs both in quasi-static and dynamic deformation. If a pulse is transmitted to a material that has an amplitude exceeding the elastic limit, this pulse will decompose into an elastic and plastic wave. There are mainly three classes of plastic waves, which are as follows;

a) *Plastic waves in Rods, Wires, and Bars:* The classical example of this situation is the impact of a long plastic rod against a rigid target. If the lateral dimensions of the rod (diameter) is small, a state of uniaxial stress is established. The study of this type of plastic wave is carried out in this chapter.

b) *Plastic waves in Semi-infinite Bodies:* When the lateral strains (perpendicular to the direction of propagation of the stress front) are zero, a state of uniaxial strain is established and the resulting plastic wave has a very sharp front: it is therefore called a shock wave.

c) *Plastic Shear Waves:* Torsional waves in bars or shear waves in semi-infinite bodies can, if their amplitude is sufficiently high, generate plastic deformation.

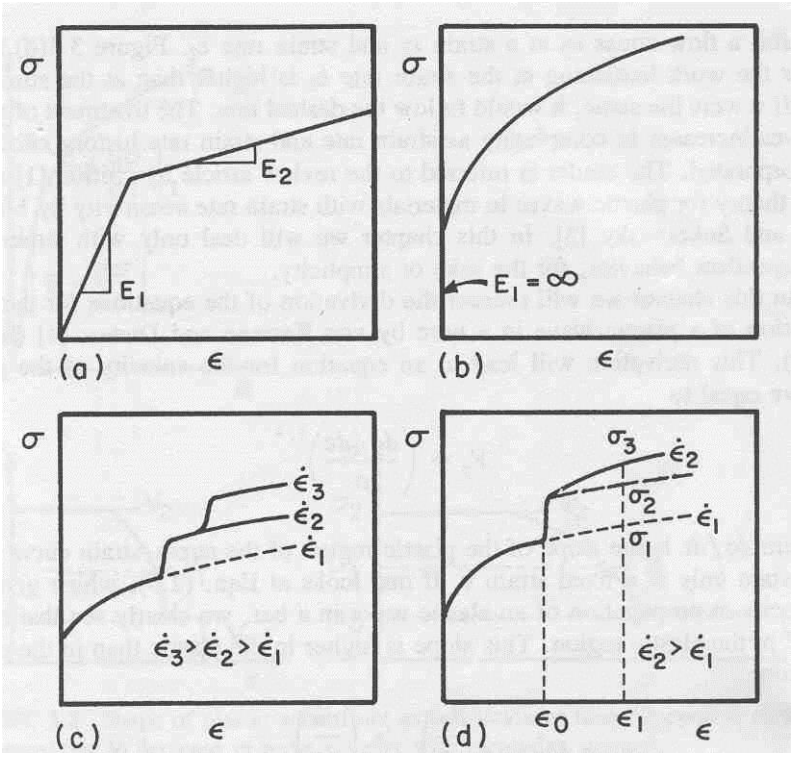

Figure 2.10 Stress-Strain curves for ductile materials: (a) bilinear elastoplastic; (b) power law work hardening; (c) strain-rate dependent flow stress; (d) strain rate history dependence of flow stress.

Material strength is strain and strain rate dependent, as exemplified by Figure 2.10. For metals, the stress-strain curve is often represented by a bilinear function [Figure 2.10(a)] where the first stage is elastic and the second stage is plastic. The stress-strain curve in many metals approaches more closely a power function of the type;

$$\sigma = \sigma_0 + k\varepsilon^n \qquad (2.11)$$

where the strain hardening exponent n<1 [Figure 2.10(b)] The strain dependence of the flow stress is schematically illustrated in Figure 2.10(c): If the strain rate is changed during the test, the flow stress is accordingly changed. This dependence of flow stress on strain rate is often represented by

$$\sigma = \sigma_0 + k\varepsilon^n \dot{\varepsilon}^m \qquad (2.12)$$

where m is the strain rate sensitivity and usually varies between zero and unity for metals. An additional factor that often has a noticeable effect is the strain rate history. Figure 2.10(d) shows how this effect can change the mechanical response of a material. If the strain rate of a material is changed from $\dot{\varepsilon}_1$ to $\dot{\varepsilon}_2$ at a strain ε_1,

the flow stress changes from σ_1 to σ_2. However, if the strain rate change occurred earlier, at a strain of ε_0, the work hardening rate of the material could have been modified by the higher strain rate. In that case, the material would exhibit a flow stress σ_3 at a strain ε_1 and strain rate $\dot{\varepsilon}_2$. Figure 2.10(d) shows how the work hardening at the strain rate $\dot{\varepsilon}_2$ is higher than at the strain rate $\dot{\varepsilon}_1$. If it were the same, it would follow the dashed line. The treatment of plastic waves increases in complexity as strain rate and strain rate history effects are incorporated.

The equations for the propagation of a plastic wave in a wire, which has derived by Karman and Duwez [3], lead to an equation for the velocity of the plastic wave equal to

$$V_p = \sqrt{\frac{d\sigma / d\varepsilon}{\rho}} \tag{2.13}$$

where $d\sigma/d\varepsilon$ is the slope of the plastic region of the stress-strain curve. V_p is constant only at a fixed strain ε. Comparing with the elastic wave propagation velocity equation, it is clearly seen that $d\sigma/d\varepsilon$ is E in the elastic region. Since this slope is higher in the elastic than in the plastic region;

$$\left(\frac{d\sigma}{d\varepsilon}\right)_{el} > \left(\frac{d\sigma}{d\varepsilon}\right)_{pl} \tag{2.14}$$

Thus, the velocity of plastic waves is lower than the velocity of elastic waves. [1, 4]

2.3. Shock Waves

As mentioned above shock waves are kind of plastic waves, where the strain perpendicular to the applied load can be neglected, while impacting a rod onto a semi-infinite body. To obtain this kind of wave front higher velocities should be ensured. Since this is not a subject in this thesis, reader can refer to [1-6] for further knowledge.

3. PLASTIC DEFORMATION AT HIGH STRAIN RATES

High strain rate plastic deformation of metals is a common phenomenon. Firstly, it is involved in many metal-forming processes, such as machining, drawing and forging, etc. Typical machining processes are turning, drilling, and milling. Secondly high strain rate deformation is also seen in the crash accidents of motor vehicles, airplanes, and space vehicles. Thirdly, high strain rate deformation of metals is associated with many aspects of battlefields. This application includes penetration of targets, shaped charges and fragmentation of warheads.

High strain rate plastic deformation is always accompanied with temperature rise of the deformed body, where as a constant temperature maintained in static deformation. The increment of temperature in the deformed material for a given strain depends on its thermal and physical properties, such as density, heat capacity and thermal conductivity. When the deformation time is much shorter than the thermal relaxation, this deformation can be considered as adiabatic. Other common features of high strain rate deformation are the formation of deformation twins and shear localization. Twinning and adiabatic shear localization is not included in this thesis.

3.1. Dislocation Dynamics

Plastic flow of fully dense solids can be considered as a kinetic process in which the deviatoric parts of the stress field drive dislocations and other defects (e.g. vacancies) to move. These defects are called the carriers of deformation. Strain rate thus reflects the flux of the deformation carriers, especially the flux of dislocations. [7]

In reality, difficulties exit in connecting individual dislocation behavior with macroscopic deformation, because of collective movement of mobile dislocations and interactions among these dislocations. However there still exit some clues from macroscopic deformation to explore the function of dislocations. The stress-strain relations are one of those clues and will be discussed below

3.1.1. The effect of strain rate on stress-strain curves

In general, the stress is a function of strain, strain rate, the temperature, and the structure of material. In order to illustrate the strain rate effect in a wide range of strain rates, Campbell and Ferguson [1] introduced four deformation processes in temperature and strain rate spectrum: (i) athermal, (ii) thermally activated, (iii) twinning, and (iv) viscous drag. Figure 3.1 shows the relationship between lower yield stress and shear strain rate for 0.12 %C steel; shown in the figure are (i) athermal, (ii) thermally activated, and (iv) viscous drag (or dislocation damping).

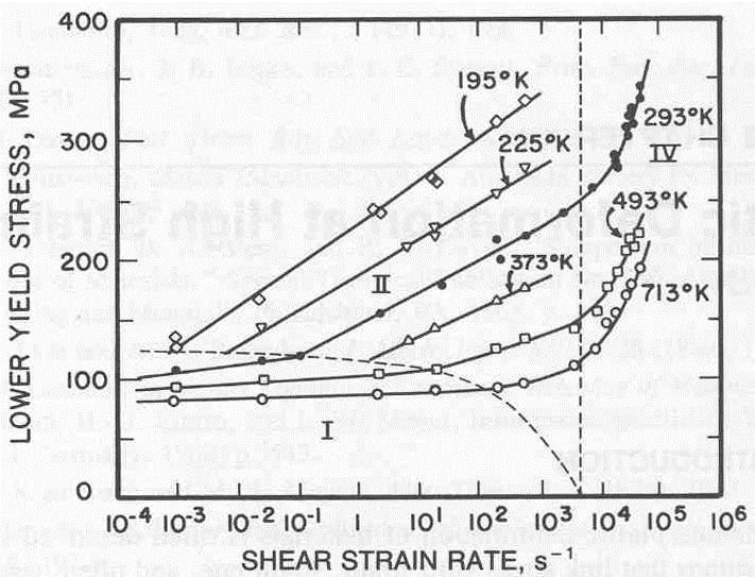

Figure 3.1 The relation between lower yield stress and shear strain rate of 0.12%C steel; (I) athermal, (II) thermally activated, and (IV) dislocation damping process at strain rates ≥ 5000/s [1].

Also both BCC and FCC metals exhibit a stress increase with the increase of strain rate [8, 9]. However BCC metals usually exhibit stronger temperature and strain rate dependence of flow stress than FCC metals. This behavior is attributed to the rate-controlling mechanism of the thermal component of the flow stress [7].

Figure 3.2 presents the resistance to dislocation motion as a function of dislocation velocity. There exist different regimes of dislocation motion, corresponding to different strain rates. These regimes are athermal, thermally activated, viscous drag and relativistic effects. In the athermal zone the flow stress is insensitive to strain rate and plastic flow is not thermally activated. It mainly takes place in the low strain rates and high temperature zone, and it is due to long-range barriers that are related to grain boundaries, precipitates, and second phase partides.

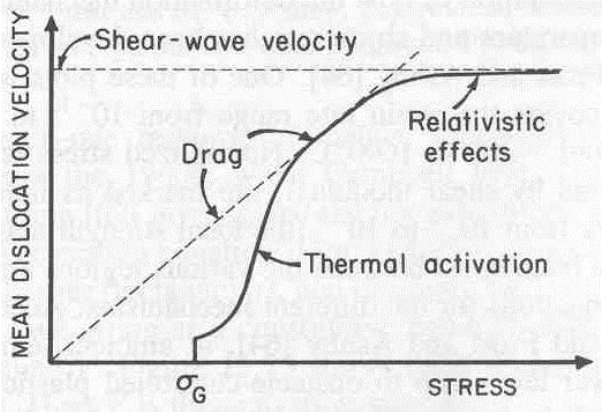

Figure 3.2 Three regimes of dislocation response [1].

In the thermally activated regime, thermal activation energy is required to assist dislocations overcoming the short-range barriers, such as Peierls-Nabarro stress barriers, interaction of forest dislocations, cross-slip and climb of dislocations. In BCC metals, overcoming of Peierls-Nabarro stress is dominant factor. In FCC metals, however, forest dislocations are most important barriers [7].

At very high strain rates, Ferguson et al [10] suggested that viscous drag on dislocations is the rate-controlling mechanism and its effect increases rapidly with strain rate. When dislocation velocity asymptotically approaches the shear-wave velocity of the material, relativistic effect then has to be taken into account.

It has been suggested that the plasticity of BCC metals is controlled by the screw dislocation mobility [7,8]. The mobility of a dislocation can be controlled by interactions with many types of defects, e.g., other dislocations, impurities, solute atoms, precipitates, point defects etc. However, the structure of the dislocation itself is an even important factor. Actually the Peierls barrier in BCC metals is critically dependent on the character of the dislocation. Non-screw (edge and mixed) dislocations have relatively low Peierls stresses. On the other hand, the screw dislocations behave relatively sessile at low temperatures and it is also responsible for certain asymmetries in the mechanical behavior.

3.1.2 General description of the mechanical response

The results presented in Figure 3.1 allow a general description of the types of response shown by many metals and alloys at different strains and temperatures. Region I corresponds to low strain rates and high temperatures, where the flow stress is essentially constant and independent of temperature and strain rate. The controlling mechanism of flow is the long-range friction stress due, for example, to the presence of large precipitates. Thermal vibrations in the lattice are unable to

assist in overcoming these barriers. This ''athermal'' friction stress increases with increasing alloy content and predominates in highly-alloyed materials which, in consequence, appear less sensitive to strain rate.

At lower temperatures and higher strain rates the short-range barriers to flow, such as dislocation interaction, become relatively more important. Here thermal vibrations can assist in overcoming the barriers, and flow becomes sensitive to temperature and strain rate.

On the other hand the mechanical responses described above differ for FCC, BCC and other types of metals. More details on the athermal regime are presented in the review article by Harding [11]. But there is general agreement that in Region II, i.e. for strains up to ~5000/s, thermal activation is the rate controlling mechanism. At strain rates above this, however, a change in controlling mechanism is generally thought to occur. If the data in Region IV of Figure 3.1 are plotted as shown in Figure 3.3, an approximately linear dependence of flow stress directly on strain rate rather than on the algorithm of strain rate, is observed (implying that flow at these strain rates is viscous in nature). It is usual, therefore, to associate the change in mechanical response at strain rates above ~5000/s with a change from thermal activation to phonon drag as the rate controlling mechanism [10].

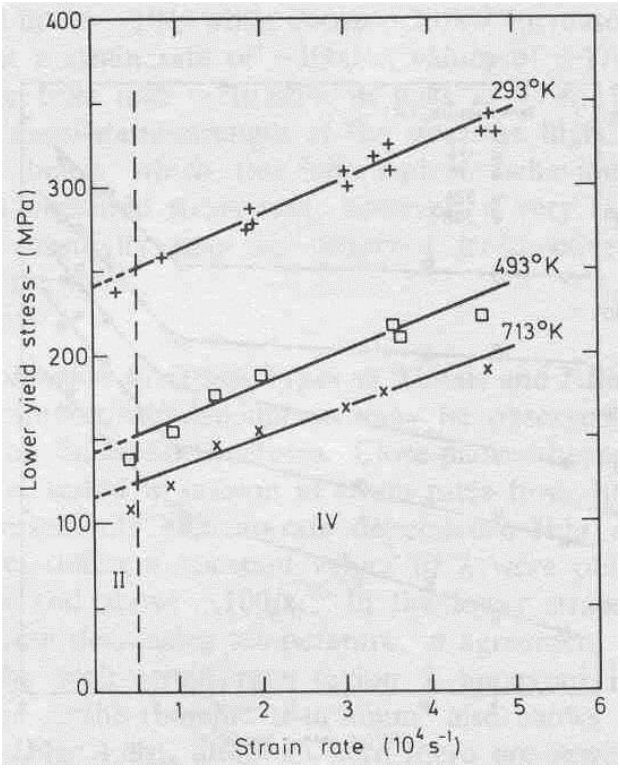

Figure 3.3 Strain rate sensitivity in mild steel at very high strain rates [1].

On the other hand Lindholm [12] has suggested that in aluminum there is a transition to a second thermally activated mechanism while for copper his results could be represented without any dramatic increase in strain rate sensitivity up to a strain rate approaching 10^5 /s. In contrast, Follansbee [11, 13], also working on copper and using Split Hopkinson Pressure Bar at the highest strain rates, found clear evidence (Figure 3.4a) for a dramatic increase in strain rate sensitivity of the flow stress at 15% strain, over the strain range from 10^3 to $3x10^4$ /s. From an analysis of their results in terms of dislocation dynamics they conclude that only upper end of this strain range does the dislocation velocity approach the drag-controlled limit. Below this results correspond to a transition zone between the regions where thermal activation and dislocation drag are rate controlling. At even higher strain rates, approaching 10^7 /s, Huang and Clifton [11], have found almost an order of magnitude increase in the shear flow stress over that 10^3/s (Figure 3.4b), from which they also concluded that above ~10^4 /s dislocation motion is governed by the intrinsic resistance of the clear lattice [14, 15].

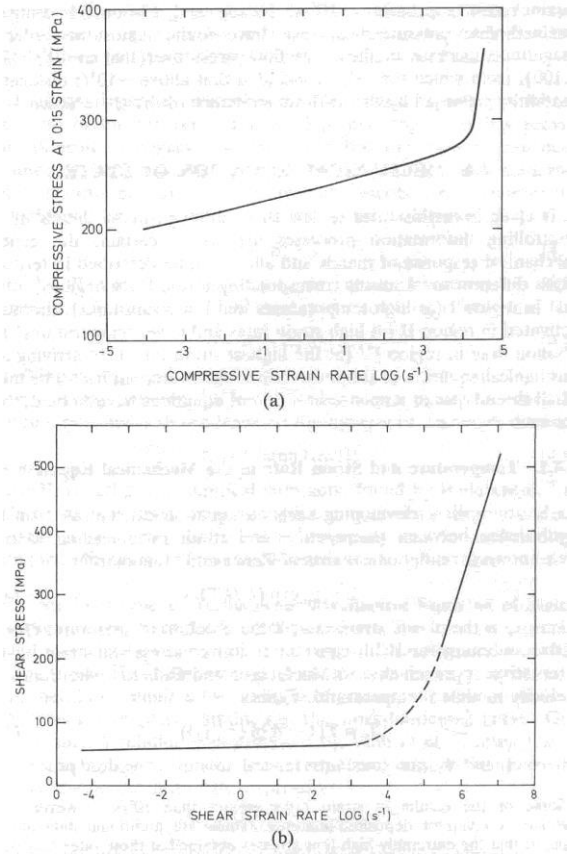

Figure 3.4 Strain rate sensitivity in copper at very high strain rates; (a) Compression tests at strain rates approaching 10^5/s, (b) Inclined-plate pressure shear tests at strain rates up to 10^7/s [11].

Also it should be emphasized that when the strain rate increases, the deformation process changes gradually from fully isothermal to fully adiabatic, because there is not enough time for the heat generated in the deformation to escape out of the body. This give rise, in some cases, to adiabatic shear instabilities that have a profound effect on the mechanical response of the material. These adiabatic shear bands will not be treated in this study.

3.2. Thermally Activated Dislocation Motion

A dislocation continuously encounters obstacles as it moves through the lattice. Some of these obstacles are shown in Figure 3.5. These obstacles make the movement of dislocations more difficult. Figure 3.5 shows an array of obstacles: solute atoms (interstitial and substitutional), vacancies, small-angle grain boundaries, vacancy clusters, inclusions, precipitates, and so on. Dislocations themselves can oppose the movement of dislocations.

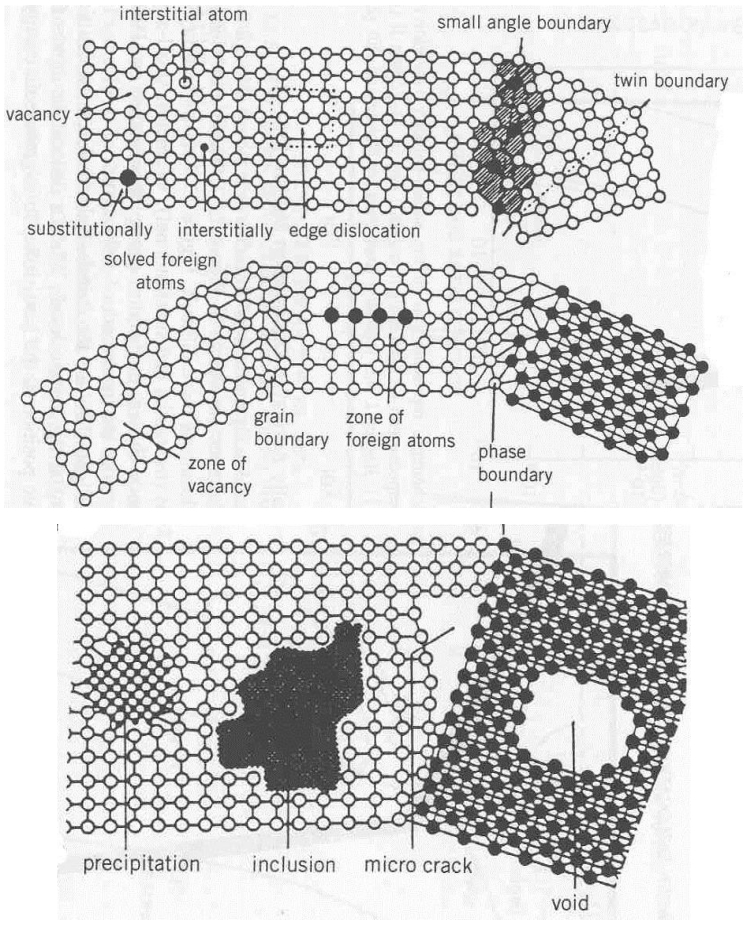

Figure 3.5 Different types of defects in crystalline materials.

Not shown in Figure 3.5 are the Peierls-Nabarro forces, which are opposing the movement at the atomic level. When a dislocation moves from one equilibrium position to the next, it has to overcome an energy barrier, that is, force has to be applied to it. Figure 3.6 shows the Peierls-Nabarro barrier. The stress required to move the dislocation without any other additional external help is the Peierls-Nabarro stress τ_{PN}. Position 2 is an unstable equilibrium position.

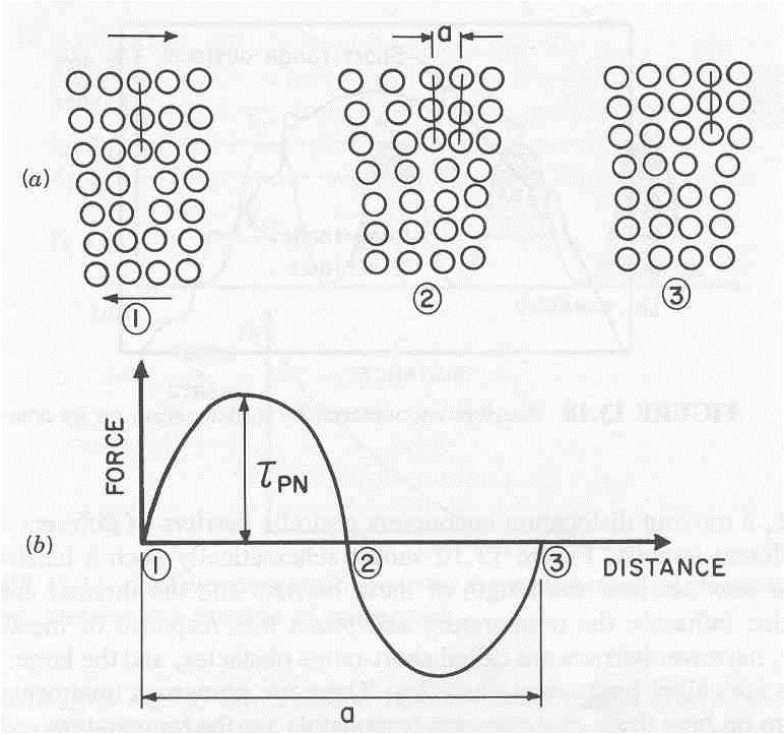

Figure 3.6 Peierls-Nabarro force: (a) movement of dislocation from one equilibrium position to next; (b) applied stress vs. distance.

The wavelength of these barriers is equal to the periodicity of the lattice. Shown in Figure 3.7 is an array of dislocations intersecting a slip plane. The dislocations that ''stand up'' and through which the moving dislocation has to move are called forest dislocations.

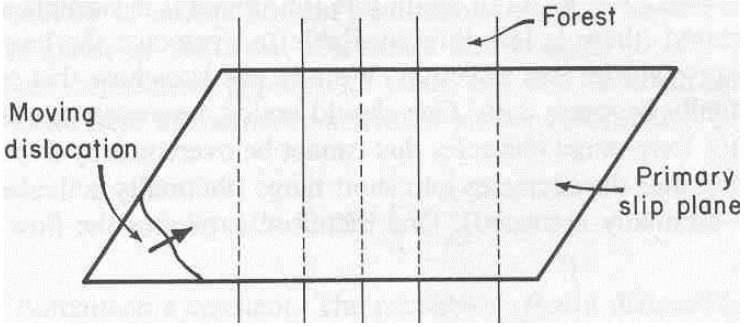

Figure 3.7 Dislocation cutting through a dislocation forest.

Thus a moving dislocation encounters periodic barriers of different spacing and different lengths. Figure 3.8 shows schematically such a barrier field. It is important to emphasize the influence of the length of these barriers and the thermal energy of the lattice, the temperature and strain rate response of metals. The smaller, narrower barriers are called short-range obstacles, and the larger, wider barriers are called long-range obstacles. There are numerous treatments in the literature on how these obstacles are responsible for the temperature and strain rate sensitivity of crystalline materials.

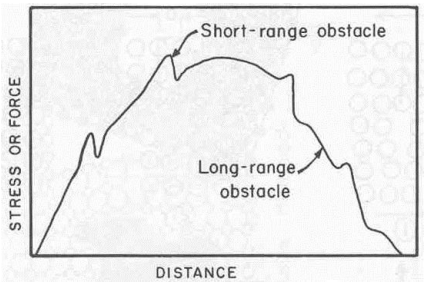

Figure 3.8 Barriers encountered by a dislocation on its course.

Thermal energy increases the amplitude of vibration of atoms. This energy can help the dislocation to overcome obstacles, as shown in Figure 3.9. The barrier is shown at four temperatures $T_0(=0)$, T_1, T_2, T_3, ($T_0 < T_1 < T_2 < T_3$). The thermal energies $\Delta G_1, \Delta G_2, \Delta G_3$ have been shown by hatching. Note that the area under a force-distance curve is an energy term. The effect of thermal energy is to decrease the height of the barrier by successively increasing amounts as the temperature increases. Figure 3.9(b) shows the stress required to move the dislocation past that specific obstacle as a function of temperature. The effective height of the barrier decreases as the temperature rises. The effect of strain rate (or velocity) is similar: as the strain rate is increased, there is less time available to overcome the barrier and the thermal energy will be less effective. The stress eventually becomes zero.

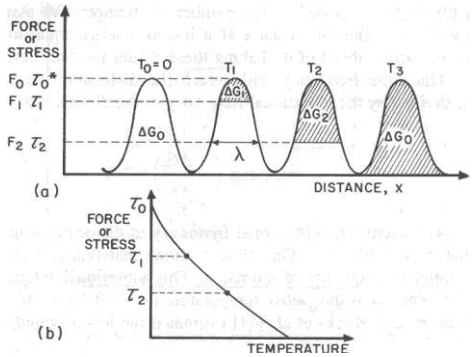

Figure 3.9 (a) Overcoming of barriers by thermal energy; (b) stress required to overcome obstacles as a function of temperature.

It should be noticed that (Figure 3.8) there are long-range obstacles that can't be overcome by thermal energy; thus, one classifies the obstacles into short range (thermally activated) and long range (non-thermally activated). Therefore the flow stress of a material can be expressed as

$$\sigma = \sigma_G(structure) + \sigma^*(T, \&structure) \tag{3.1}$$

The term σ_G is due to the athermal barriers (long range) determined by the structure of the materil. The term σ^* is due to the thermally activated barriers, that is, the barriers that can be overcome by thermal energy. The principal short-range barrier is the Peierls-Nabarro stress, which is very important for BCC metals. The Peierls-Nabarro stress is also the rate controlling mechanism for ceramics. For FCC and HCP metals, dislocation forests are the primary short-range barriers at lower temperatures. The different nature of these barriers is extremely important and is responsible for the major differences in strain rate sensitivity between FCC and BCC metals. In ceramics, the Peierls-Nabarro stresses are so high that these barriers are not overcome at roomtemperature. The strong ionic and covalent bonds as well as their high directionality (bond angles fixed by electronic structure) are responsible for these extremely high Peierls-Nabarro stresses. Therefore, they fail by an alternative mechanism (crack nucleation and growth). But this case is not included in this study.

The probability of an equilibrium fluctuation in energy greater than a given value ΔG is given by statistical mechanics and is equal to;

$$p_B = \exp\left(-\frac{\Delta G}{kT}\right) \tag{3.2}$$

where k is Boltzmann's constant. The probability that a dislocation will overcome an obstacle can be considered as the ratio of the number of successful jumps over the obstacle divided by the number of attempts. We assume that a dislocation will overcome the obstacle if it has an energy equal to or higher than the energy barrier ahead of it. Taking these values per unit time, we have frequencies. Thus the frequency with which the dislocation overcomes the obstacle, υ_1, divided by the vibrational frequency of the dislocation, υ_0, is equal to p_B,

$$\upsilon_1 = \upsilon_0\left(-\frac{\Delta G}{kT}\right) \tag{3.3}$$

Kocks [1] discuss the vibrational frequency of dislocations in detail and conclude that it is ~10^{11} s^{-1}. One should notice that this is 100 times less than the vibrational frequency of atoms, υ. This vibrational frequency, υ, is equal to kT/h, where T is the Debye temperature. If the space between obstacles is l, Kocks [1] estimated the lower bound of υ_0 to be

$$\upsilon_0 = \upsilon \frac{b}{4l} \tag{3.4}$$

This is the ground frequency of a dislocation with wavelength $4l$.

It is convenient to divide the time Δt taken by a dislocation to move a distance Δl between two obstacles into a waiting time in front of obstacles (t_w), and a running time between obstacles (t_r). Thus;

$$\Delta t = t_r + t_w \tag{3.5}$$

The average waiting time t_w is governed by the probability that an obstacle will be overcome by an adequately large thermal fluctuation of the free activation energy ΔG. From Equation 3.3;

$$t_w = \frac{1}{\upsilon_0} \exp \frac{\Delta G}{kT} \tag{3.6}$$

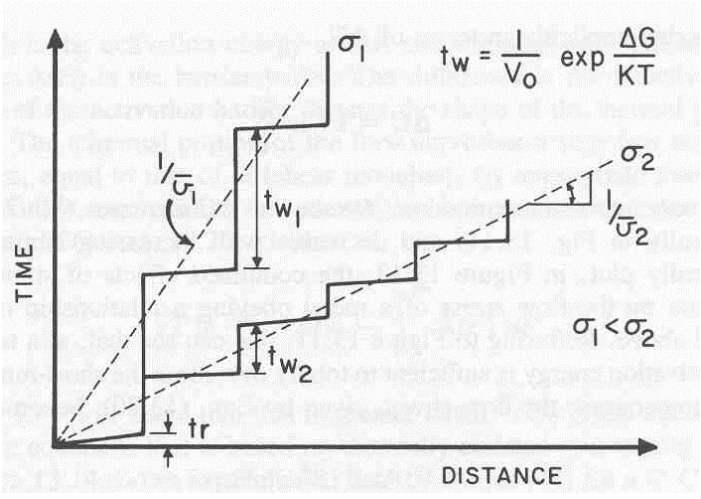

Figure 3.10 Distribution of running and waiting times for dislocation at two stress levels σ_1 and σ_2 ($\sigma_1<\sigma_2$).

Figure 3.10 shows the distribution of running and waiting times for dislocations at two stress levels, σ_1 and σ_2; the waiting times are lower at the higher stress level, σ_2, and thus the mean velocity $\bar{\upsilon}$ is higher. In Figure 3.10, $t_w >> t_r$. This seems to be the case in actuality and Equation 3.5 becomes

$$\Delta t \cong t_w \tag{3.7}$$

After using Equations 3.6, 3.7 and rearrangements we obtain;

$$\Delta G = kt \ln \frac{\dot{\varepsilon}}{\varepsilon} \tag{3.8}$$

It is clearly seen that ΔG increases with T (as shown in Figure 3.9) and decreases with increasing strain rate.

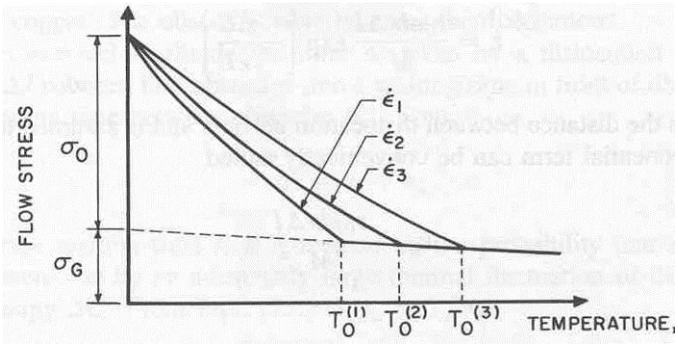

Figure 3.11 Flow stress as a function of temperature for different strain rates; thermal and athermal components of stress indicated.

It is schematically plotted, in Figure 3.11, the combined effects of strain rate and temperature on the flow stress of a metal obeying a relationship of the type described above. Referring to Figure 3.9, one can see that, at a temperature T_3, the activation energy is sufficient to totally overcome the short-range barrier. At this temperature, the flow stress, given by Equation 3.1, becomes

$$\sigma = \sigma_G + \sigma^* = \sigma_G \tag{3.9}$$

Thus, the thermal component of stress becomes zero. At 0 K, on the other hand, the activation energy is zero, and the flow stress is

$$\sigma = \sigma_G + \sigma_0 \tag{3.10}$$

where σ_0 is the thermal component of stress. In Figure 3.11, the thermal and athermal components of flow stress are marked. At 0 K, as well as above T_0 (which is strain rate dependent), the flow stress is strain rate independent. Between 0 K and T_0, the thermal component of flow stress is given by the formulation below. One has to calculate ΔG from the activation barrier. In Figure 3.9, it can be seen that ΔG is the hatched area. This area is equal to;

$$\Delta G = \Delta G_0 - \int_0^{F^*} \lambda(F) dF \qquad (3.11)$$

where ΔG_0 is the activation energy at 0 K and the integral is the non hatched area. Here, $\lambda(F)$ is the barrier width. The difference is the effective barrier. The shape of the activation barrier dictates the shape of the thermal portion of the curve. The athermal portion of the flow curve has very low temperature dependence, equal to that of G (shear modulus). By appropriate manipulation of Equation 3.11, one obtains the relationship between stress and strain rate.

$$kT \ln \frac{\dot{\varepsilon}}{\varepsilon} = \Delta G_0 - \int_0^{F^*} \lambda(F) dF \qquad (3.12)$$

This is the foundation for constitutive equations that are based on thermally assisted overcoming of obstacles [1, 16].

3.3. Dislocation Drag Mechanism

When a phonon incident at a dislocation has a shear stress component on the slip plane in the slip direction, then the phonon drives the dislocation into forced oscillations. Electrons are also scattered by dislocations.

In general term, dislocation drag mechanism becomes important when the strain rate is higher than 3000/s [17]. A moving dislocation interacts with, and scatters, phonons and electrons. If it is not affected by other obstacles, the velocity of the dislocation is equal to

$$v_{dis} = \frac{\tau b}{B} \qquad (3.13)$$

As the temperature increases, the phonon density rises. It has been found that the drag coefficient, B, increases linearly with temperature [7]:

$$B = B_e + B_p\left(\frac{T}{300}\right) \tag{3.14}$$

where B_e is the electron drag coefficient, and B_p is the phonon drag coefficient at 300 K. There are three approaches for the measurement of B: direct observation of dislocation motion during a stress pulse, internal friction measurement, and high-strain-rate tensile or compression test.

However, in high-strain-rate deformation, such as shock loading, it is found that dislocation generation rate is the controlling factor in the strain rate. Follansbee supported this dislocation generation theory with the application of mechanical threshold stress to the region of dramatic increase of strain rate sensitivity. The linear dependence of dynamic flow stress on applied strain rate was matched by a similar linear dependence of mechanical threshold stress on strain rate. Therefore, when the mechanical threshold stress was used to define the constant structure condition instead of plastic strain, no dramatic increase in rate-sensitivity characteristic of the region was observed.

Zerilli and Armstrong [18] introduced viscous drag into the Zerilli-Armstrong equation to model the plastic deformation of copper, and compared the predictions with the experimental data from Regazzoni [7]. They concluded that viscous drag is an unlikely mechanism for the upturn in flow stress at strain rates of 10^3 - 10^4 / s. Instead, it is associated with an enhanced accumulation rate of dislocations. Johnson and Tonks [7] reported the detection of dislocation drag effects in copper at strain rates greater than 10^4 / sec by shock waves of the peak pressure of 3 and 5.4 GPa. Their results show that dislocation drag is important only at small plastic strains and high strain rates.

3.3.1. Further topics in dislocation drag mechanism

In region II of Figure 3.12 the velocity of dislocations is proportional to the applied stress. It is well known that dislocation motion causes a temperature increase.

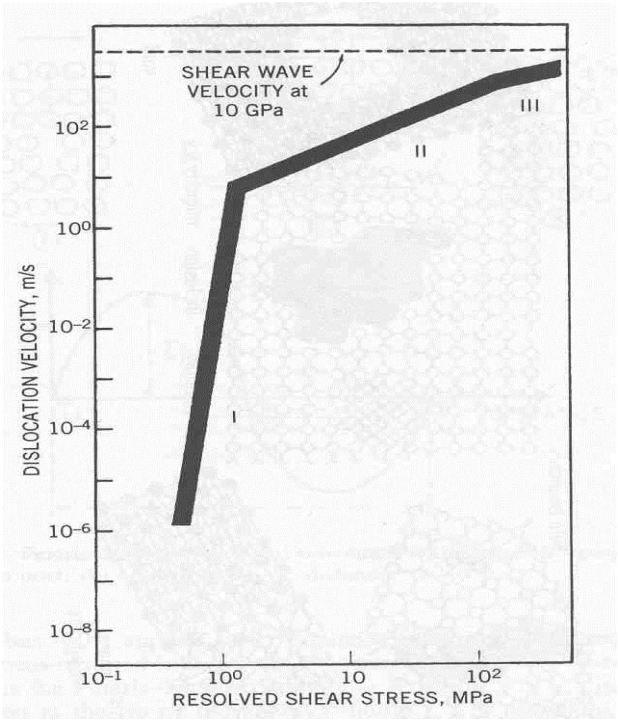

Figure 3.12 Schematic representation of the stress-velocity behavior of Nickel [1].

The cold rolling of a piece of Ni increases its temperature substantially. It is also known that the energy stored in the material after deformation (as defects) is only a small portion of the energy spent to deform it. The energy of the substructure (residual) is usually only 5-20% of the total energy. So 90% of the energy is dissipated by forces opposing the applied stresses. They can be expressed as a viscous behavior of the solid. To a first approximation, the solid can be assumed to act as Newtonian viscous material with respect to the dislocation. Hence,

$$f_v = Bv \tag{3.15}$$

where B, the viscous damping coefficient, is independent of v for a Newtonian fluid. Under the application of a certain external stress, the dislocation will accelerate until it reaches a steady-state velocity. The force on an edge dislocation moving under the action of a shear stress τ is;

$$F = \tau b \tag{3.16}$$

where b is the dislocation Burgers vector. With Equation 3.16, equilibrium will be reached when;

$$\tau b = Bv \tag{3.17}$$

With $\dot{\varepsilon} = (1/M)\rho b v$ (from dislocation dynamics) and substituting $\tau = \sigma/2$

$$\sigma = \frac{2BM}{\rho b^2}\dot{\varepsilon} \qquad (3.18)$$

where, M is the orientation factor (taken as 3.1 for BCC crystals, 2.75 for FCC crystals). Thus, the flow stress should be proportional to the strain rate if dislocation drag mechanisms are operative.

The drag mechanisms that are not thermally activated are the interaction of the dislocation with thermal vibrations (phonon drag) and with electrons (electron viscosity); additionally, they also include relaxation effects in the dislocation core. A phonon is an elastic vibration propagating through the crystal. It is quantitized because the lattice is discrete and not continuous. These mechanisms will be described briefly below

- *Phonon Viscosity:* A change in the compressive stress will trigger an increase in the modulus of rigidty. This increase in modulus relaxes with time, as the phonons approach equilibrium. In detail, it was pointed out that since a dislocation is surrounded by a strain field which changes at a given point as the dislocation moves along, one should expect a conversion of dislocation energy to thermal energy by the same mechanisms that damp moving sound waves, namely, electron and phonon viscosity.
- *Phonon Scattering:* There are several ways by which phonon-scattering mechanisms can operate. One of these is the scattering of phonons by the dislocation strain field in a manner similar to the refraction of light. Another is the absorption of energy from phonons by dislocations, with subsequent vibrations by dislocations.
- *Thermoelastic Effect:* A moving dislocation alternatively strains adjacent regions in tension and compression; these regions show temperature decreases and increases, respectively. An irreversible process of heat flow ensues, increases the entropy, and depletes the dislocation of some of its energy.
- *Electron Viscosity:* The free electrons in a metal will affect the dislocation motion in the same way as phonon viscosity.
- *Anharmonic Radiation:* A dislocation, when undergoing positive or negative acceleration, emits elastic waves. This corresponds to an outflow of energy. Thus, the dislocation, although accelerating between two equilibrium positions, give off energy.

• *Glide Plane Viscosity:* There seems to be a certain consensus with respect to the relative importance of the various drag mechanisms under various conditions. They are given below [1]:

Covalent bonding: At low stress levels ($< G/100$) the motion is thermally activated (e.g., overcoming of Peierls stresses) and is stopped at low temperatures. However, stresses alone, when high enough ($>G/100$), cause motion at low temperatures.

Ionic bonding: At low stress levels and high temperature, phonons are responsible for the drag.

Metals: At high temperatures, phonons cause drag; at low temperatures, electrons cause drag. At high stresses, for both metals and salts, the viscosity increases because of relativistic effects.

Granato [1] adds that, for materials not containing an electronic cloud (covalent and ionic bonding), drag by radiation is the mechanism operating at low temperatures. They also comment on the interaction between dislocations and point defects if these are moving slowly enough. This belongs to the group of thermally activated mechanisms.

From Figure 3.13 [19] it can be seen that the measurements are in fair agreement with the sum of three dislocation mechanisms that are discussed above.

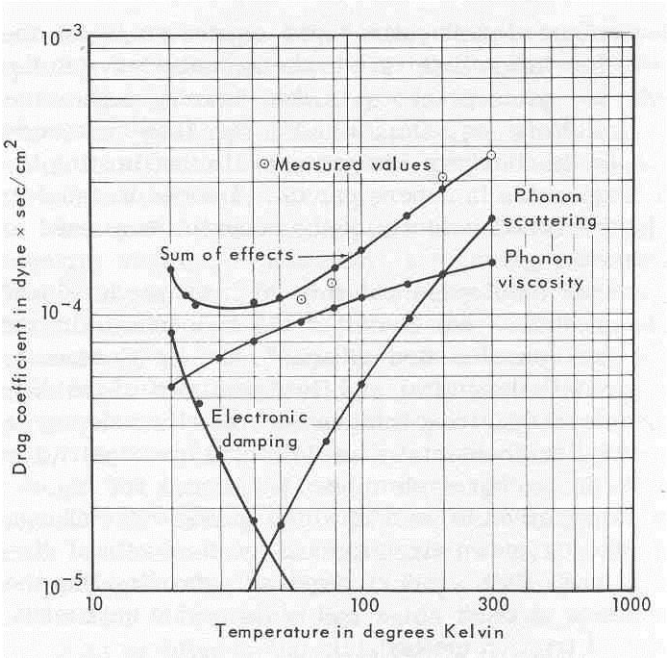

Figure 3.13 Measured drag coefficient for lead and the three components of dislocation drag [19].

4. CONSTITUTIVE RELATIONSHIPS AT HIGH STRAIN RATES

The mathematical formulation describing the macroscopic response of a material to applied force is known as constitutive relation, or equation. In the most general form, a constitutive equation relates the stress of a material to the strain, strain rate, temperature, and loading history experienced by the material. It is not possible, however, for a single relationship to completely describe the deformation behavior of a material for all combinations of loading conditions and histories. Depending on the intended use, availability of experimental data, and the desired accuracy of the description, a decision must be made as to the amount of effort to be invested. Typically, the effort required to describe the material behavior is proportional to the degree of accuracy with which the governing physical mechanisms are modeled.

The availability of current high-speed computers allows for the implementation of more complicated, physically based constitutive relations into codes for solving problems involving deformation of materials at high strain rates. The ability to accurately describe material behavior for a wide range of loading conditions and to predict the mechanical response outside of the measured condition is growing in demand. Despite this, most of the constitutive relations implemented into computer codes describe only the effects of strain hardening, and take some account of thermal softening, but few relations presently account for strain rate effects.

Three most widely used relations that do account for strain rate effects are the Johnson-Cook, the Zerilli-Armstrong, and the mechanical threshold stress (MTS) constitutive relations. The Johnson-Cook and the Zerilli Armstrong constitutive relations are relatively simple, one dimensional models that account for the effects of strain, strain rate, and thermal softening on flow stress and utilize a von Mises yield criterion. They both describe the material hardening behavior based on the well known power-law function introduced by Ludwick. That is;

$$\sigma = \sigma_0 + K\varepsilon^n \tag{4.1}$$

The Johnson-Cook constitutive relation is an empirical relation that is relatively simple to calibrate for a given material. That is, very few stress-strain curves covering the loading conditions are required to determine the parameters. It is

relatively easy to implement into computer codes, inexpensive to use and produces reasonably accurate predictions for a range of materials if loading conditions do not exceed those used to determine the material parameters.

The Zerilli-Armstrong constitutive relations are semi-empirical models based on the concept of dislocation dynamics. Separate relations were developed to describe the deformation behavior FCC and BCC materials. A subsequent relation was introduced for HCP materials, which generally exhibit behavior between that of BCC and FCC materials. Overall, the Zerilli-Armstrong relation tend to give a slightly better correlation, but is steel relatively easy to implement into computer codes and inexpensive to use. Similar to the Johnson-Cook relation, however, it is not very accurate when used outside of the range of loading conditions that it was calibrated for, or for large strain calculations.

The MTS relation is a more advanced and physically-based model that relates the macroscopic mechanical response of a material to microscopic properties. It accounts for the evolution of sub-structures as a function of plastic deformation and loading history. It generally is more accurate than both the Johnson-Cook and Zerilli-Armstrong relations, and once it is calibrated for a particular material it can be used to accurately predict deformation outside the range of calibration loading conditions. This has been attributed to the form used to represent the work hardening behavior in the MTS relation. Rather than use a power law form, which yields a continuously increasing stress for increases in strain, a function is selected that ''saturates'' to a maximum stress level for increasing strain. This concept was based on the observation that at large strains most metallic materials tend to approach a finite ''saturation stress'', or approach a constant, but small hardening rate at large strains. However, it should be noted that the form of the equation used to describe the work hardening behavior is not strictly physically-based and, therefore, the MTS relation is also semi-empirical. The main disadvantages of the MTS relation are that it requires an extensive experimental database to determine the material parameters, it is more difficult to incorporate into computer codes and more computationally expensive [20].

Another classification of constitutive relations that are used in problems involving plastic deformation at high strain rates are unified viscoplastic relations. The main disadvantage of viscoplastic relations are that they are more difficult to incorporate into codes and require iterative solutions making them computationally expensive. Consequently they have seen limited use in codes utilized for high strain rate material modeling and not be treated in this study.

4.1. Johnson-Cook Constitutive Relationship

The Johnson-Cook constitutive relation is a one-dimensional, empirically based relation that describes the variation of flow stress, $\bar{\sigma}$, with respect to strain, strain rate and temperature as,

$$\bar{\sigma} = (A + B\bar{\varepsilon}_p^{\,n})(1 + C\ln \dot{\varepsilon}^*)(1 - T_h^{\,m}) \tag{4.2}$$

where $\bar{\varepsilon}_p$ is the effective plastic strain, $\dot{\varepsilon}^*$ is a non-dimensional, effective plastic strain rate, and T_h is a form of homologous temperature. The parameters A, B, C, m, n are material constants obtained from fitting experimental data and are defined as follows:

The non-dimensional strain rate is defined as;

$$\dot{\varepsilon}^* = \frac{\dot{\varepsilon}}{\dot{\varepsilon}_0} \tag{4.3}$$

Where $\dot{\varepsilon}_0$ is a reference strain rate, typically taken to be 1 s^{-1}, and the homologous temperature is defined as,

$$T_h = \frac{(T - T_{room})}{(T_{melt} - T_{room})} \tag{4.4}$$

where T is the absolute temperature of the specimen. T_{room} represents room temperature and T_{melt} is the melting temperature. It should be noted that all of the temperatures are in units of degrees K.

The Johnson-Cook relation is essentially a modified form of the over-stress type of models introduced by Malvern, Perzyna and Campbell [20]. In these models the plastic strain rate is no limited to finite value and therefore, strength increases linearly with respect to logarithmic strain rate. It should also be noted that effect of non-proportional loading history on flow stress are not considered in this model.

The Johnson-Cook relation considers the effect of strain, strain rate and temperature in an uncoupled manner, as seen in Equation 4.2, the first term describes the flow stress as a power law of strain. The second term represents the logarithmic effect of strain rate, and the third term expresses the effect of temperature through thermal softening. Since these terms are uncoupled it implies

that the strain rate sensitivity is independent of temperature, which is typically not true for metals.

Holmquist and Johnson introduced a modified version of the Johnson-Cook relation based on evidence that the influence of strain rate of material strength is no a linear function of the natural log. They suggested that it is better represented as a exponential function. The flow stress in the modified Johnson-Cook relation is represented as;

$$\bar{\sigma} = (A + B\bar{\varepsilon}_p^{\,n})(\dot{\varepsilon}^*)(1 - T_h^m) \tag{45}$$

where the parameters are as above [21, 22].

Also Rule and Jones [23] proposed a modified version for ductile materials. Many ductile materials display an enormous increase in yield stress for strain rate in excess of 10^3 s^{-1}. The aim of this modification is to enhance the high strain rate sensitivity of the Johnson-Cook model while minimizing changes to the model for those loading regimes where it has clearly been shown to be effective. The proposed form of the model is;

$$\bar{\sigma} = (A + B\bar{\varepsilon}_p^{\,n})\left[1 + C\ln\dot{\varepsilon}^* + D\left(\frac{1}{E - \ln\dot{\varepsilon}^*} - \frac{1}{E}\right)\right](1 - T_h^m) \tag{46}$$

where D, and E are additional empirical coefficients.

4.2. Zerilli-Armstrong Constitutive Relationship

Zerilli and Armstrong introduced two dislocation-mechanics based constitutive relations that describe the von Mises flow stress as a function of strain, strain rate, temperature, and grain size in a coupled manner. Based on the concept of thermal activated motion of dislocations and the nature of dislocation interactions, one relation was developed to describe the deformation of FCC copper and the other for BCC iron. Although the constitutive relations introduced by Zerilli and Armstrong were developed for copper and iron, it was intended that they would be applicable for a wide range of FCC and BCC materials since they were developed from physical principles inherent to each crystallographic structure.

For BCC metals, the motion of dislocations is governed predominantly by the interaction produced by the overall lattice potential (Peierls-Nabarro stress), which leads to minimal strain hardening. For FCC metals the predominant interaction is at dislocation intersections, which leads to substantial strain hardening. The Equation for BCC metals is;

$$\bar{\sigma} = \sigma_a + Be^{-\beta T} + B_0 \bar{\varepsilon}^n \tag{4.7}$$

and for FCC metals it is;

$$\bar{\sigma} = \sigma_a + B_0 \bar{\varepsilon}^{1/2} e^{-\alpha T} \tag{4.8}$$

where $\bar{\varepsilon}$ is the equivalent plastic strain, and T is the absolute temperature. The parameter σ_a represents the athermal component of the flow stress and is determined mainly from the effects of solutes and grain boundaries. It is expressed as;

$$\sigma_a = \sigma_G + kd^{-1/2} \tag{4.9}$$

where, σ_G represents the influence of solute and the original dislocation density on the effective stress. The second term known as the Hall-Petch term, calculates the stress associated with the plastic flow between grain boundaries at low temperatures. The variable k represents the microstructural stress in density and the variable d is the average grain diameter.

The terms α and β are expressed as;

$$\alpha = \alpha_0 - \alpha_1 \ln \dot{\varepsilon} \tag{4.10a}$$

$$\beta = \beta_0 - \beta_1 \ln \dot{\varepsilon} \tag{4.10b}$$

where, $\dot{\varepsilon}$ is the equivalent strain rate and the variables $B, B_0, \beta_0, \beta_1, \alpha, \alpha_0$, σ_G, k, d and n are material constants that are determined from experimental data.

Zerilli Armstrong stated that their original relation for BCC metals, expressed in Equation 4.7, was incomplete since it did not account for the effect of twinning, which is important in BCC materials. An improved version for the BCC relation was introduced, which incorporated a simple deformation-twinning model. It was

suggested that plastic flow by slip could be replaced by twinning at high strain rates in the presence of large grains. To account for this effect, they modified the Hall-Petch term in Equation 4.7 to be;

$$\sigma_a = \sigma_G + kd^{-1/2}\left[(N_T + 1)^{1/2} - 1\right] \quad (4.11)$$

where N_T represents the average number of twins per grain. Further developments are still made on this constitutive relationship [20, 24].

4.3. Discussion of Constitutive Models

In the Johnson-Cook model, temperature and strain rate give the same influence to the yield stress and work hardening of materials, because of the consecutive multiplication of its three components. Liang and Khan [17] mentioned that the Johnson-Cook model for both copper and iron predicts the "fan-out" stress-strain curves. In BCC metals, however, the effects of temperature and strain rate on the stress-strain curve usually produce an approximately parallel translation (upwards or downwards), whereas the stress-strain curves should "fan out" in FCC metals, because of the different rate-controlling mechanism of the thermal component of the flow stress. This indicates that in bcc metals the effects of temperature and strain rate on work hardening are smaller than those on yield stress. Even in FCC metals, the amplitudes of temperature and strain effects on yield stress and work hardening may not necessarily be equal. In most cases, the strain-rate sensitivity parameter in thermally activated regime is constant. However, these characteristics are not represented by the Johnson-Cook model. The Johnson-Cook model is especially inadequate for BCC metals below room temperatures where yield stress is highly sensitive to the temperature change. The large difference in effects of temperature on yield stress and work hardening forbids the achievement of sensible fit of this model to the experimental data [7]. However, for medium and high strain rates of deformation, Johnson-Cook Model exhibits good correlation between experimental studies, especially with split Hopkinson Pressure bar [21, 22, 25, 26]. Also it should be noted that the stress relaxation due to the temperature rise during the deformation is included in the constitutive relation. Moreover, the ballistic studies mostly used this relationship. Because of these advantages, Johnson-Cook model is selected to model the material behavior in this thesis.

Although the above problems are virtually overcome in the Zerilli-Armstrong models, the form of work hardening behavior adopted by Zerilli-Armstrong models, especially

the BCC model remains the same as that of Johnson-Cook model, which is originally proposed by Ludwik. The mandatory insensitivity of work hardening rate to temperature and strain rate is adopted in Zerilli-Armstrong bcc model. However, it has been shown that for most metals work hardening increases with increasing strain rate. The inherent nature of this form of mathematical function gives a monotonic increase of stress with strain. If the parameters of Johnson-Cook and Zerilli-Armstrong models are optimized for high strains, it is usually the case that at small strain the prediction of flow stress and yield stress is lower than the experimental values [7].

MTS model can provide a better prediction for the stress-strain relationship over a large strain range even if it is established in low strain regime. There are two reasons for MTS model to be success. First, it embodies the saturation concept. Second, it utilizes the differential form of the work hardening law. Another drawback to the MTS model is a great amount of experimental effort required to determine the evolution of structure during the deformation.

Aldo, as mentioned above there are lots of proposed constitutive models available in the literature, which are successful with agreement of the predicted values other than these [27-29]

5. HIGH STRAIN RATE TESTING

High strain rate testing had a slow beginning in the early 19th century. The first dynamic experiment was conducted by Bertram Hopkinson on steel and he concluded that the dynamic strength was at least twice as high as its slow-strain-rate strength.[1] A surge in the study of high strain rate deformation began around World War II. This activity has been reviewed numerous times. Thus some effects of high strain rate on material properties have been well established in the high strain rate community since the early 1950's. However the impact of these effects on the larger scientific community has been much slower.

This chapter reviews the high strain testing techniques used to characterize dynamic material properties. These techniques can be classified according to experiment mode (Figure 5.1), or according to strain rates (Figure 5.2).

Mode	Applicable strain rate, s^{-1}	Testing technique
Compression	<0.1	Conventional load frames
	0.1 to 100	Special servohydraulic frames
	0.1 to 500	Cam plastometer and drop test
	200 to 10^4	Hopkinson pressure bar in compression
	10^4 to 10^5	Taylor impact test
Tension	<0.1	Conventional load frames
	0.1 to 100	Special servohydraulic frames
	100 to 10^4	Hopkinson pressure bar in tension
	10^4	Expanding ring
	$>10^5$	Flyer plate
Shear	<0.1	Conventional shear tests
	0.1 to 100	Special servohydraulic frames
	10 to 10^3	Torsional impact
	100 to 10^4	Hopkinson (Kolsky) bar in torsion
	10^3 to 10^4	Double-notch shear and punch
	10^4 to 10^7	Pressure-shear plate impact
Fracture toughness (rates are stress intensification rates, $\dot{K}$, $MPa\sqrt{m}\ s^{-1}$)	2.75 to 2×10^5	Plane-strain fracture toughness testing
	10^5	Charpy test
	10^5 to 10^6	One-point bend
	2×10^6	Dynamic notched round bar
		Crack arrest
Fatigue	0.1 to 100	Ultrasonic fatigue

Figure 5.1 Schematic classification of testing techniques according to modes [34].

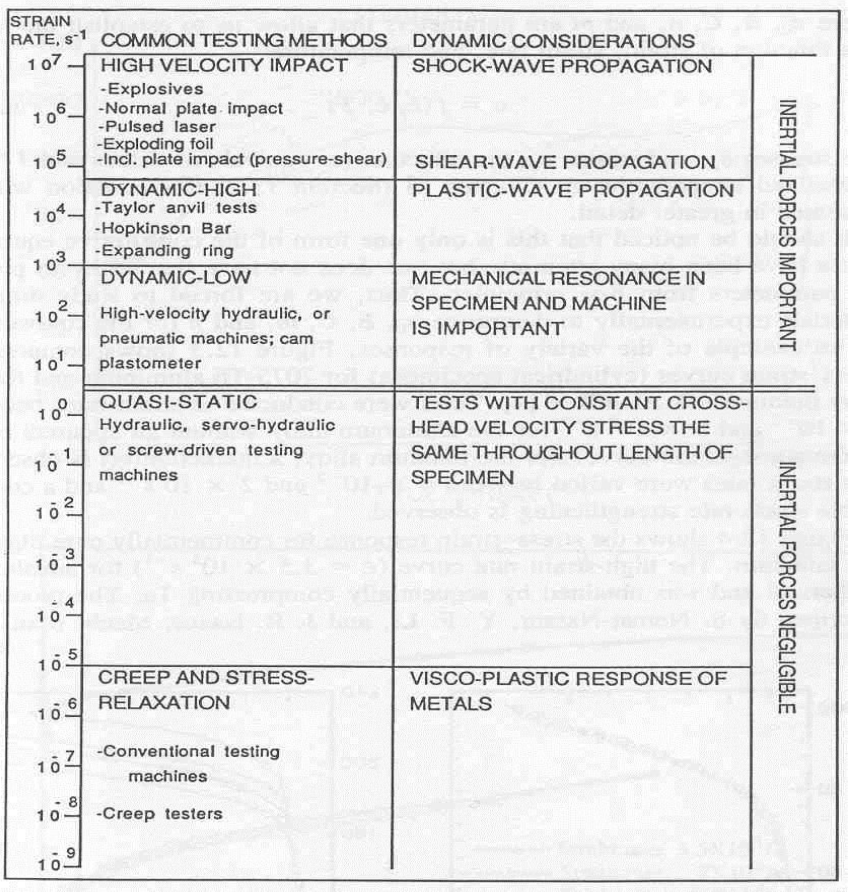

Figure 5.2 Schematic classification of testing techniques according to strain rate [1].

The techniques seen in Figure 5.1 are at various stages of standardization. For example Charpy Test is currently a standard test. All other test methods currently are not standardized by ASTM.

Of three major considerations intrinsic to high strain rate testing, wave propagation has been the most troublesome. Wave propagation becomes important in testing when the time interval of the applied force is so short and the dimensions of the specimen are such that the inertia force in the material is locally comparable to the local force for deformation. As the size of the specimen and strain rate increase, the effects of wave propagation generally become more significant, because the time available for a stress wave to propagate and reflect multiple times becomes a significant portion of the test duration time. In addition, the stress wave may not propagate with a constant waveform. Consequently, the intended applied stress form is modified quickly. Alternations of specimen dimensions to avert these problems eventually are ineffective at higher strain rates. Wave propagation effects must then be accounted for in an analog manner. Most of the effort to develop high strain rate testing has concentrated on accounting for wave propagation or modifying specimens to eliminate its effects.

The second major consideration in high strain rate testing is the influence of strain rate on deformation and failure modes of materials. The influence of temperature in changing deformation mode from slip to twinning in body centered cubic metals is well known. Other factors such as crystal orientation also influence this change.

The third general consideration in performing high strain rate tests is the direct effect of high strain rate on properties. Even if wave propagation is properly handled and no change in deformation or failure mode occurs over the range of strain rate of interest, an increase in strength and a decrease in toughness usually occurs. The effect of strain rate on properties varies for each material. These general trends are well known, but because the magnitude of the change in properties with strain rate are so varied for each material, no general quantitative theory exists that satisfactorily predicts the mechanical properties of materials over a wide range. This subject is closely related with constitutive relations, which were discussed before. [30]

5.1. Historical Background of High Strain Rate Testing

As the 19th century progressed, there was an increasing awareness that the properties of materials under impact differed from those under static or quasi-static loading.

Experimental investigations were hampered by lack of suitable instrumentation but considerable theoretical progress was made in the understanding of the propagation of stress waves in bounded media such as circular rods. It is generally considered that John Hopkinson in 1872 made the first experimental demonstration that metals can withstand a larger impulsive tensile load than they can under static tensile loading. However, Dunn in 1897 was credited with constructing the first true high strain-rate testing machine. Bell also discusses in his book the contribution of H Tresca.

After John Hopkinson's tragic death in an Alpine climbing accident along with three of his six children, his son Bertram Hopkinson was elected to carry on his father's work as Professor of Engineering at Cambridge. He invented an ingenious ballistic pendulum method for determining the shapes of pulses caused by the impact of bullets or the detonation of explosive charges at one end of a long rod in 1914. By using momentum traps of different lengths, he was able to build up a picture of how much momentum passed down the rod as a function of time for different classes of event (assuming that these types of event are repeatable). Because he performed

the pioneering work on determining the shapes of impulses traveling down rods, the device consisting of a long rod to convey a force pulse to a force transducer became known as the Hopkinson pressure bar. This was rapidly put to use in the First World War, and is still used to this day in its original configuration in blast wave loading studies. These achievements of the Hopkinsons were reviewed by G.I. Taylor in a lecture he gave in 1946.

With the development of the continuous strip mill in the 1920s there was renewed interest in determining the dynamic properties of steels both in tension and in torsion, particularly at high temperatures. Very little work seems to have been performed on dynamic compressive loading before the Second World War, although G.I. Taylor had been thinking of a method of estimating the dynamic strength of materials in compression towards the end of the 1930s. His method consists of firing a solid cylinder of the material against a massive and rigid target. The dynamic flow stress of the cylinder material can be estimated by measuring the overall length of the impacted cylinder and the length of the undeformed (rear) section of the projectile by means of the following simple formula:

$$\sigma = \frac{\rho V^2 (L - X)}{2(L - L_1)\ln(L / X)} \tag{5.1}$$

where σ is the dynamic yield stress of the material of the projectile, ρ its density, V its impact velocity, and L, X and L_1 are defined in Figure 5.3.

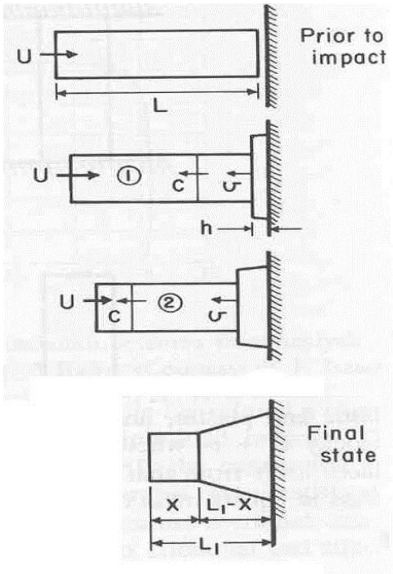

Figure 5.3 Sequence of deformation after impact of cylindrical projectile against rigid wall [32].

One of the assumptions made in deriving this expression was that the rear of the projectile undergoes constant deceleration. Taylor & Whiffin knew that this assumption is not true, but an analysis taking account of the variation in acceleration yields a set of expressions that are transcendental in the yield stress and in which the plastic wave speed acts as a free variable. Taylor and Whiffin's method of solving these equations consisted of numerically determining the plastic wave speed consistent with both the measured deformation and their theory. This then allowed the yield stress to be determined. In order to use this more exact method routinely, Taylor presented it as a set of graphs yielding multiplicative correction factors to Equation 5.1. Whiffin showed that the correction factor was velocity dependent.

The publication of this method occurred just before Kolsky's famous paper on the use of two Hopkinson pressure bars to measure the dynamic properties of materials in compression [31]. This device became known as the split Hopkinson pressure bar (SHPB) and soon became the standard technique for obtaining high strain rate properties of materials, having the advantage over the Taylor test of loading the material under nearly uniform stress and strain rate.

However, the Taylor test, or variants on it such as rod-on-rod impact, has been used and developed to the present day. It has not often been used to obtain dynamic yield stresses of materials but for studying the propagation of plastic waves, and for checking constitutive models by comparing the shapes of recovered cylinders with computer predictions. It has also been used for its original purpose in obtaining the dynamic properties of polymers at room temperature and energetic materials. [32]

Other methods for obtaining dynamic stress-strain curves that have been developed include the cam plastometer, hydraulically driven mechanical testing machines, drop-weight towers and the expanding ring test. With the exception of the expanding ring test, these other methods produce somewhat lower strain rates than the SHPB (10^2 s^{-1} or less) as opposed to 10^3 s^{-1} or greater [32].

5.2. Split Hopkinson Pressure Bar (SHPB) Test

Development of test techniques based on the Hopkinson bar has led to significant advances in high strain rate testing capabilities. These techniques yield the highest possible strain rates in a uniaxial compression test under uniform deformation conditions. In addition, the determination of stress within the deforming specimen is made without use of a load cell, and the measurement of strain is made without directly monitoring the specimen length.

5.2.1. Historical perspective

The Hopkinson bar derives its name from its developer, who in 1914 used a long elastic bar to study the pressures produced by the impact of a bullet or by the detonation of an explosive. In designing this experiment Hopkinson recognized that, as long as the pressure bar remains elastic, the displacements in the pressure bar are directly related to the stresses and that the length of the wave in the bar was related to the duration of the impact through the velocity of sound in the bar, a quantity that was well known. A significant feature of this work was that the pressures were estimated by measuring the momentum (with a ballistic pendulum) acquired bay a small section of the bar placed in contact with the bar at the far end.

Further developments in the experimental techniques occur a few decades after these original experiments, when Davies [33], and Kolsky [31] designed condensers to measure displacements in pressure bars. Kolsky also introduced the split Hopkinson pressure bar technique, in which the specimen is sandwiched between two pressure bars. He demonstrated how stress and strain within the deforming specimen are related to displacements in the pressure bars. Because of these contributions, the split Hopkinson pressure bar is often referred to as the Kolsky bar.

In the last two decades, there have been numerous advances in experimental procedures based on the Hopkinson bar. The use of strain gages to measure surface displacements on the elastic pressure bars was the first reported in 1961, and a technique for performing elevated-temperature tests was described in 1963. The Hopkinson bar was first configured for torsional loading in 1966. Lindholm introduced a unique procedure for testing in tension and has provided reviews of Hopkinson bar testing techniques that have become standards for current procedures [34]. There are still developments made to obtain more accurate results [29, 35, 71].

5.2.2. Basic principles

As identified by Hopkinson, the use of a long, elastic bar to study high-rate phenomena is feasible, because the wave propagation behavior in such a geometry is well understood and mathematically predictable. Thus, the displacements or stresses generated at any point can be deduced by measuring the elastic wave at any point as it propagates along the bar.

There are two basic configurations of the Hopkinson bar for compression testing. The most widely used is the split Hopkinson pressure bar, shown in Figure 5.4.

Several investigators have recently used single pressure bar configuration. The basic principles of the two techniques are similar.

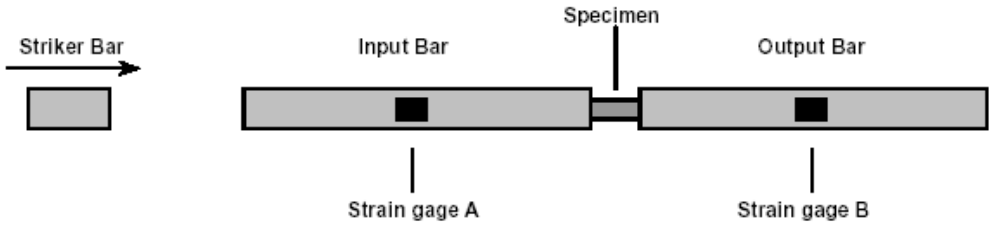

Figure 5.4 Schematic of SHPB apparatus.

The split Hopkinson pressure bar consists of two elastic pressure bars that sandwich the specimen between them. Typically, a striker bar is propelled toward the incident bar. Upon impact, an elastic compressive wave is generated within the incident bar, and the time-dependent strain in the pressure bar is measured at strain gage A, located at the midpoint of the incident bar. At the incident bar/specimen interface, the wave is partially reflected and partially transmitted into the specimen. The portion that is reflected travels back along the incident bar as a tensile wave, and the strain, $\varepsilon_R(t)$, is measured by strain gage A.

The strain gage on the incident bar is located at the bar midpoint so that the incident and reflected waves can be measured independently. If the strain gage were located close to the incident bar/specimen interface, the leading edge of the reflected wave could interfere with the trailing edge of the incident wave. The compressive strain, $\varepsilon_T(t)$, associated with the portion of the wave that is transmitted through the sample into the output bar is measured by strain gage B, located at the midpoint of the output bar.

When the specimen is deforming uniformly, the strain rate within specimen is directly proportional to the amplitude of the reflected wave. Likewise, the stress within the sample is directly proportional to the amplitude of the transmitted wave. These two signals can be recorded, the former integrated to yield strain, and combined to give the dynamic stress-strain curve. Figure 5.5 shows a typical SHPB response.

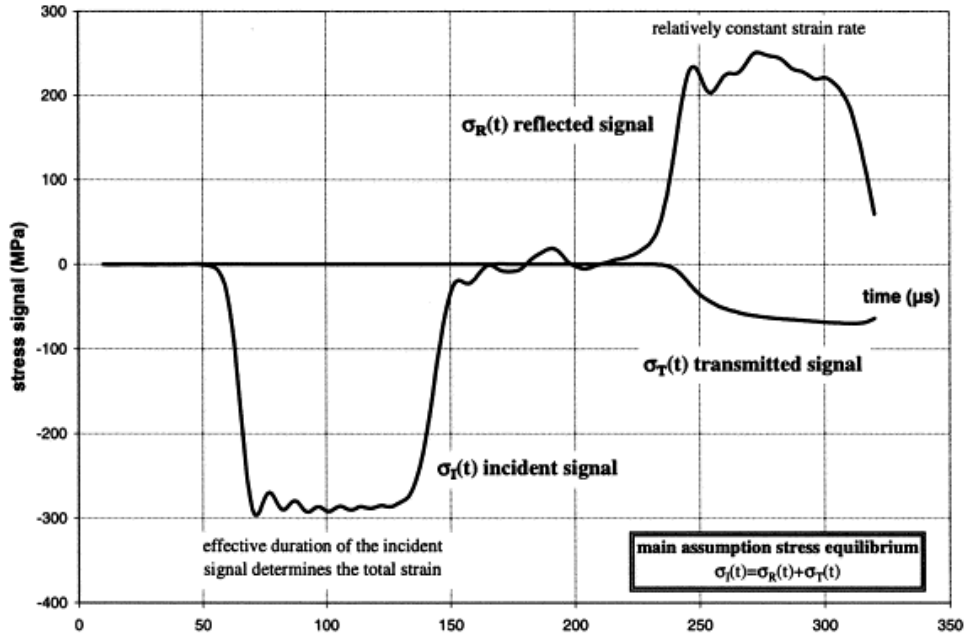

Figure 5.5 Strain signals recorded by strain gauges and converted into stress [55].

5.2.3. The derivation of related formulas for SHPB

In order to arrive at an equation for the specimen stress, it is necessary to consider the forces imparted on the specimen during the initial loading of the SHPB. This is shown below in Figure 5.6.

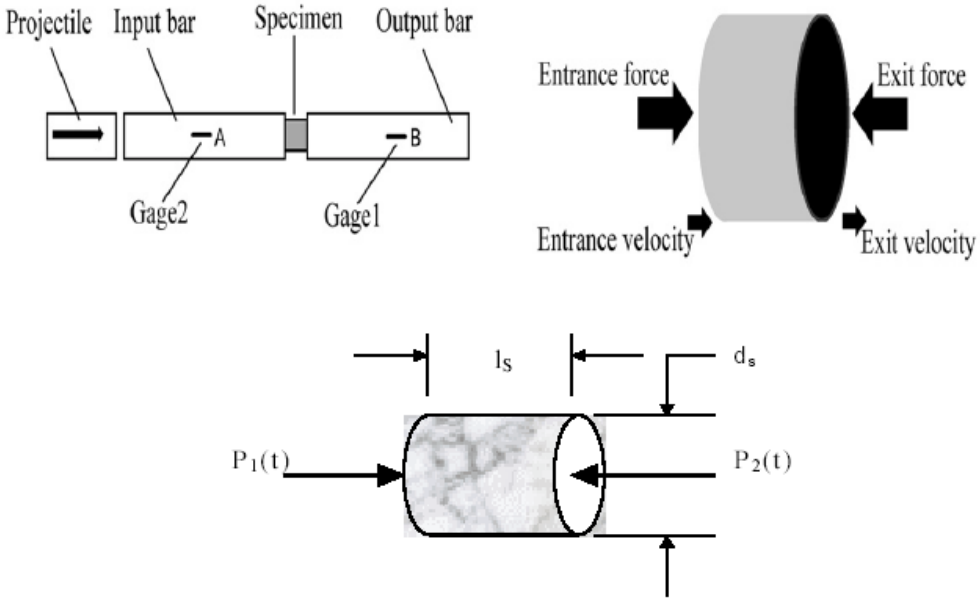

Figure 5.6 Cylindrical specimen in uniaxial stress state.

In Figure 5.6, the forces $P_1(t)$ and $P_2(t)$ are the result of the contact between the input and output pressure bars and the test specimen and d_s and l_s are the diameter and length of the test specimen, respectively. These forces are shown as functions

of time since, during the dynamic event, the forces vary during the loading and unloading of the specimen. Noting that the forces developed in the specimen are compressive in nature, the average specimen stress can be computed. Thus:

$$\sigma_{AVG}(t) = \frac{\frac{P_1(t) + P_2(t)}{2}}{A} = \frac{P_1(t) + P_2(t)}{2\frac{\pi d_s^{\,2}}{4}} \tag{5.2}$$

Equation 5.2 is actually the relation for the average specimen stress as the specimen is originally in an equilibrium state prior to the application of the uniaxial load. Analyzing the equilibrium state of the specimen during the loading event, the forces `P1(t)` and `P2(t)` can be replaced by the corresponding incident and reflected pressure bar strains. Consequently, with a pressure bar diameter `dbar`,

$$P_1(t) = E\left[\varepsilon_I(t) + \varepsilon_R(t)\right]\frac{\pi d^{\,2}_{bar}}{4} \tag{5.3}$$

$$P_2(t) = E\left[\varepsilon_T(t)\right]\frac{\pi d^{\,2}_{bar}}{4} \tag{5.4}$$

In Equation 5.3 and 5.4, $\varepsilon_I(t)$ is the input bar incident strain signal, $\varepsilon_R(t)$ is the input bar reflected strain signal and $\varepsilon_T(t)$ is the transmitted strain signal. In order to generate a more useful equation, the average specimen stress must be related to the incident, reflected and transmitted strain histories $\varepsilon_I(t)$, $\varepsilon_R(t)$, and $\varepsilon_T(t)$. This can be accomplished by substitution of Equations 5.3 and 5.4 into Equation 2.8. The simplified result of this substitution is shown below in Equation 5.5:

$$\sigma(t) = \frac{E d^{\,2}_{bar}}{2 d_s^{\,2}}\left[\varepsilon_I(t) + \varepsilon_R(t) + \varepsilon_T(t)\right] \tag{5.6}$$

Recalling one of the primary assumptions made in this analysis, namely that of uniform uniaxial deformation, conservation of momentum requires that the total strain in the input bar ($\varepsilon_I(t) + \varepsilon_R(t)$) equals the total strain in the output bar $\varepsilon_T(t)$. Thus,

$$\varepsilon_I(t) + \varepsilon_R(t) = \varepsilon_T(t) \tag{5.7}$$

Substitution of 5.7 into 5.6 yields the simplified equation for average specimen stress with reduced form:

$$\sigma_{AVG}(t) = \frac{E d_{bar}^2}{d_s^2} \varepsilon_T(t) \tag{5.8}$$

Thus, the average specimen stress is proportional to the total strain transmitted through the specimen. It also shows that changing the average stress imparted on the specimen is accomplished simply by changing the ratio of the pressure bar-specimen diameter. This will serve as the primary equation for calculating average specimen stress throughout the rest of this analysis.

To derive the expressions for the specimen strain and strain rate, it is necessary to review the equation of motion of a differential element in the uniformly deforming, uniaxially loaded bar:

$$\frac{\partial^2 u_1}{\partial t^2} = C_0^{\,2} \frac{\partial^2 u_1}{\partial x^2} \tag{5.9}$$

Assuming that the stress and strain are harmonic in nature, the particle acceleration in Equation 5.9 can be rewritten in terms of the particle velocity, v:

$$\frac{d^2 u_1}{dt^2} = \frac{dv}{dt} \tag{5.10}$$

Further simplification yields Equation 5.11

$$E \frac{\partial}{\partial x}\left(\frac{\partial u_1}{\partial x}\right) = \frac{\partial p}{\partial x} \tag{5.11}$$

in which p is the pressure across the homogeneous cross section. Finally, the equation of motion can be rewritten in terms of the pressure and velocity across the bar cross section as;

$$-\frac{\partial p(x,t)}{\partial x} = \rho \frac{\partial v}{\partial t} \tag{5.12}$$

Notice from Equation 5.12 that to solve for the particle velocity in a bar requires knowledge of the pressure in the bar. If we assume a positive traveling harmonic wave of the form

$$p(x,t) = Pe^{i(wt-kx)} \tag{5.13}$$

in which P is the amplitude of the pressure pulse, w is the pulse frequency, t is the temporal index, k is the wave number ($k = w/C_0$), and x is the spatial location of the wave, an expression for the instantaneous particle velocity can be computed. Taking the first derivative of Equation 5.13 with respect to x, Equation 5.14 results:

$$\frac{\partial p(x,t)}{\partial x} = -ikPe^{i(wt-kx)} \tag{5.14}$$

Substitution of 5.14 into Equation 5.12 after some arrangement yields;

$$v(x,t) = \frac{1}{\rho C_0} p(x,t) \tag{5.15}$$

For the uniaxial, elastic state of stress found in the pressure bars, the pressure is equal to the applied load divided by the cross sectional area of the pressure bar. Therefore, $p(x,t)$ can be written in terms of the bar strain as;

$$p(x,t) = \varepsilon(x,t)E \tag{5.16}$$

Substitution of Equation 5.16 into Equation 5.15 yields an expression for the particle velocity in terms of the pressure bar strain, as shown below by Equation 5.17:

$$v(x,t) = C_0\varepsilon(x,t) \tag{5.17}$$

Before proceeding further, it is necessary to recall the dynamics of the SHPB. At the input bar-specimen interface, the stress pulse is partially transmitted and partially reflected. As such, the reflected wave now behaves as a tensile stress pulse since it is traveling in the opposite direction of the incident pulse. Thus, for a wave propagating in the opposite (-x) direction, the instantaneous particle velocity v is merely the inverse of 5.17, namely

$$v(x,t) = -C_0\varepsilon(x,t) \tag{5.18}$$

With instantaneous particle velocity equation now written in terms of the pressure bar strains, specimen strain rate can be calculated. Referring back to the test specimen shown in Figure 5.6, Equations 5.16, 5.17 and 5.18 can be combined to generate Equation 5.19, the average instantaneous strain rate in the test specimen:

$$\frac{\partial \varepsilon}{\partial t} = \frac{v_{so} - v_{IS}}{l_s} \tag{5.19}$$

In Equation 3.33, v_{IS} is the particle velocity at input bar - test specimen interface while v_{so} is the particle velocity at the test specimen - output bar interface. Recall also that l_s is the length of the test specimen. The velocity at the input bar - test specimen interface (v_{IS}) is comprised of the incident wave (+x direction) and the reflected wave (-x direction). Thus,

$$v_{IS} = C_0(\varepsilon_I - \varepsilon_R) \tag{5.20}$$

Computation of the velocity at the test specimen - output bar interface (v_{so}) follows in much the same fashion as input bar - test specimen velocity calculation except that only the transmitted strain history ε_T is needed. Thus,

$$v_{so} = C_0 \varepsilon_T \tag{5.21}$$

By substituting these interface velocities into the expression for the specimen strain rate, an expression for the specimen strain rate in terms of the pressure bar strains can be found. This is shown below in Equation 5.22:

$$\frac{d\varepsilon_{specimen}}{dt} = -\frac{C_0(\varepsilon_T - \varepsilon_I + \varepsilon_R)}{l_s} \tag{5.22}$$

The negative sign in 5.22 is due to the fact that the test specimen is in a state of compression. Since the uniformly, uniaxially deforming specimen assumption is still in use, Equation 5.7 still holds true and Equation 5.22 can be reduced to

$$\frac{d\varepsilon_{specimen}}{dt} = -\frac{2C_0}{l_s}\varepsilon_R \tag{5.23}$$

With the equation defining the specimen strain rate known, the specimen compressive strain can be found through integration of Equation 5.24:

$$\varepsilon_{specimen}(t) = -\frac{2C_0}{l_s}\int \varepsilon_R(t)dt \qquad (5.24)$$

Equations 5.23 and 5.24 will form the basis for calculation of specimen strain rate and strain throughout this research. Coupled with the equation for specimen stress (Equation 5.8), these three relationships provide the SHPB scientist with a means to characterize the mechanical properties of materials using conventional strain gage instrumentation at strain rates up to and including 10^4 s^{-1}.

Summary of Equations: For a uniformly deforming specimen, the expressions relating pressure bar strains to specimen properties are greatly reduced. Before discussing the implementation of these expressions, an overview of the physics behind the test is necessary. After the striker bar impacts the input bar, elastic compressive wave is generated that propagates towards the specimen. Upon reaching the specimen, part of the wave is reflected while the remainder is transmitted through the specimen and into the output bar. By mounting strain transducers to the surfaces of the pressure bars, the reflected and transmitted waves can be recorded for use in equations 5.25;

$$\frac{d\varepsilon_{specimen}}{dt} = -\frac{2C_0}{l_s}\varepsilon_R$$

$$\varepsilon_{specimen}(t) = -\frac{2C_0}{l_s}\int \varepsilon_R(t)dt \qquad (5.25)$$

$$\sigma_{specimen}(t) = E\frac{A_0}{A}\varepsilon_T(t)$$

Many testing conditions greatly affect the implementation and effectiveness of equations 5.25. For instance the length of the impact pulse determines how much the specimen may be deformed. As mentioned the waves are dispersed, which in effect smears the waveforms. The fundamental assumption that the specimen deforms uniformly must be enforced by lubricating the specimen - pressure bar interfaces and choosing appropriate specimen dimensions. By carefully addressing these issues, dynamic stress-strain relations can be found for a broad range of

materials using equations 5.25. As a sum up Figure 5.7 shows the steps to obtain stress-strain diagram form split Hopkinson pressure bar test.

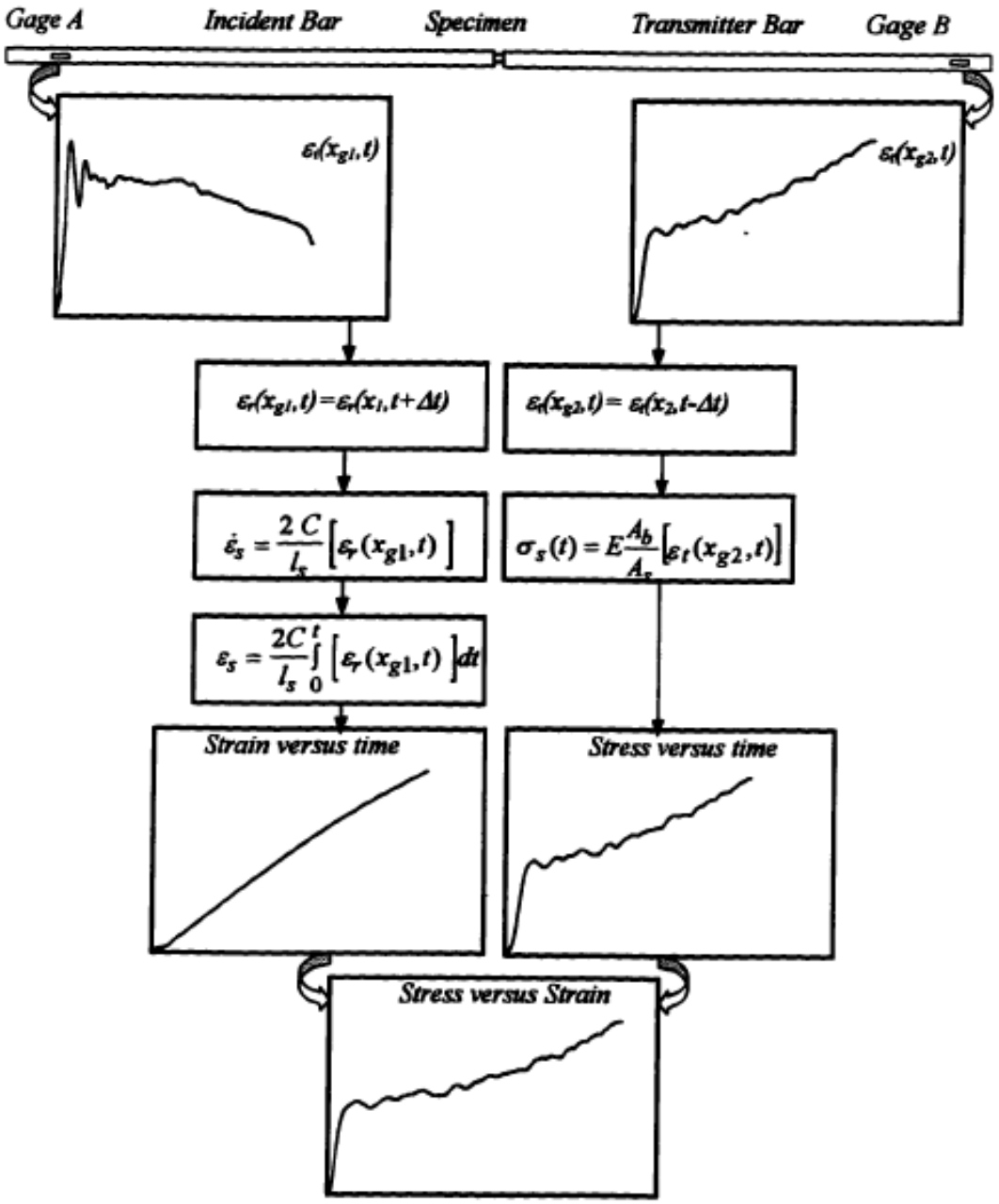

Figure 5.7 Flowchart showing the data reduction steps in SHPB test [52].

5.2.4. Wave propagation in elastic pressure bars

When the striker bar impacts the incident bar, the wave that is generated in the latter is highly complex because of end effects due to non-uniformities at the striker

bar/incident bar interface and the propagation of other types of elastic waves. However these end effects quickly dampen after the wave has propagated about ten bar diameters.

There are additional consequences of the predicted wave propagation behavior. If the wave is a pure cosine wave of wavelength λ, then axial displacements and stresses are uniform over the cross section of the bar as long as $R/\lambda << 1$, where R is the radius of the bar. In fact, when $R/\lambda < 0.1$, the displacements at the surface of the bar differ from those along the bar axis by less than 5% The majority of the energy in waves generated in the split Hopkinson bar is contained in wavelengths that exceed 10R, thus the wave can be assumed to be one-dimensional, and surface displacement measurements are accurate indicators of axial displacements in the pressure bar.

Another important consequence of wave propagation in the pressure bars is that the longitudinal velocity varies with the wavelength, which leads to wave dispersion. For $R/\lambda << 1$ the propagation velocity is the well-known longitudinal sound velocity (which was derived in Chapter 2) $C_0 = \sqrt{E/\rho}$, but as λ approaches R, the velocity of these short wavelength components decreases to $0.576C_0$ (for a bar material with a Poisson's ratio of 0.29). The lower velocity of the short wavelength components causes dispersion of the initial wave and leads to the appearance of oscillations, called Pochhammer-Chree oscillations that ride waves and build during propagation down the bar. These oscillations are simply short wavelength frequency components that lag behind the leading edge of the wave [36]. These oscillations have only a minor influence on the predicted stress-strain behavior. For more details on stress wave propagation and oscillation in rods, reader can refer to [37-41].

5.2.5. Conditions satisfying uniform deformation

Whereas wave propagation in the elastic pressure bars has been shown to be predictable mathematically, it has been far more difficult to establish conditions for uniform deformation within the sample, because this involves plastic wave propagation and the consideration of frictional constraint. In terms of Hopkinson bar testing, when the stress wave enters the sample, particles of sample are accelerated both longitudinally and radially. The first consideration is the time t required for the stress to equilibrate within the sample. It has been estimated [34] that this requires three reverberations of the stress wave, which for a plastically deforming solid obeying the Taylor-von Karman Theory yields [12];

$$t = \frac{\pi^2 \rho_s L^2}{\frac{d\sigma}{d\varepsilon}} \tag{5.26}$$

where ρ_s is the density of the specimen, L is the specimen length, and $d\sigma/d\varepsilon$ is the slope of the true stress/true strain curve. At times less than that given by Equation 5.26, the sample may not be assumed to be deforming uniformly, and stress-strain data may be in error.

An important consideration in split Hopkinson pressure bar testing is the design of the experiment, such that the time t from Equation 5.26 is reached early in the test. One way to decrease t is to decrease specimen length. Because other considerations, described below, limit the length-to-diameter ratio of the specimen, the specimen length may not be decreased alone without a decrease in the specimen and bar diameters. The use of smaller diameter bars to achieve higher strain rates is a common practice in split Hopkinson pressure bar testing [42]. An additional benefit of decreasing the radius of the bar is that this also decreases the ratio R/λ, which reduces the effects caused by dispersion discussed above.

Because the value t from Equation 5.26 can't be decreased significantly, an alternate method that will yield valid data at earlier strains is to increase the rise time of the incident wave. A symmetric impact between the striker bar and the incident bar yields a short rise time pulse that approximates a square wave. The rise time of this wave is likely to be less than t in Equation 5.26, but if the rise time of the wave is increased to a value more comparable with t, then the data will be valid at an earlier strain than if a short rise strain pulse is used. Furthermore, because the highly dispersed short wavelength components arise from the leading and trailing edges of the waves, a long rise time pulse will contain fewer of these components than will a sharply rising pulse. Experimental techniques to shape the pulse to increase the rise time will be discussed later.

The two material properties in Equation 5.26 are the density and the slope of the stress-strain curve. The latter is important because it can vary significantly from material to material. Thus, certain experimental conditions of strain rate and bar and specimen dimensions may satisfy Equation 5.26 for a strongly strain-hardening material such as copper, but these same conditions may not satisfy Equation 5.26 for a weakly strain-hardening material or for a material exhibiting a yield point phenomena.

In addition, Gorham [45] suggested that specimen dimensions should be small enough for neglecting inertia errors. He found that there is no specimen aspect ratio which causes effective cancellation of inertia terms. Although in any particular case it is possible to minimize the total contribution by selecting an appropriate geometry, the presence of inertia may be causing other errors by creating non-uniform deformation.

Even when the specimen is determined to be deforming uniformly, longitudinal and radial inertia due to the rapid particle accelerations imposed at high strain rates can influence the predicted stress-strain behavior. The errors due to both longitudinal and radial inertia have been analyzed, and corrections have been derived for these errors [12]. This approximate analysis resulted in;

$$\sigma(t) = \sigma_m(t) + \rho_s \left[\frac{l_s^2}{6} - \upsilon_s \frac{d_s^2}{8} \right] \frac{d^2 \varepsilon(t)}{dt^2} \tag{5.27}$$

where σ_m is the measures stress, ρ_s is the density of the specimen, υ_s is the Poisson's ratio. This expression has proved to be useful, because it predicts that errors are minimized if the strain rate is held constant, or if the terminside the bracket is set to zero by choosing specimen dimensions such that;

$$\frac{l_s}{d_s} = \sqrt{\frac{3\upsilon_s}{4}} \tag{5.28}$$

For a Poisson's ratio of 0.33, Equation 5.28 suggests that the optimum l_s / d_s ratio to minimize errors due to inertia is 0.5. However, the total strain in a split Hopkinson pressure bar test is limited to approximately 25% to reduce the area mismatch between the specimen and the pressure bar. Thus, it is not expected that a l_s / d_s ratio of 0.5 will introduce serious errors, provided that the interfaces are well lubricated. The subject of friction is discussed later in this chapter.

5.2.6. Equipment and test method

The split Hopkinson pressure bar test apparatus consists of the pressure bars, associated mounting and alignment hardware, gas gun or alternate method producing the compressive wave, strain gage or condenser for measuring the waves, and the associated instrumentation and data acquisition system. (Figure 5.8)

[46-48]. There currently is no standard design for a split Hopkinson pressure bar test apparatus. Thus, the following discussion is as general as possible.

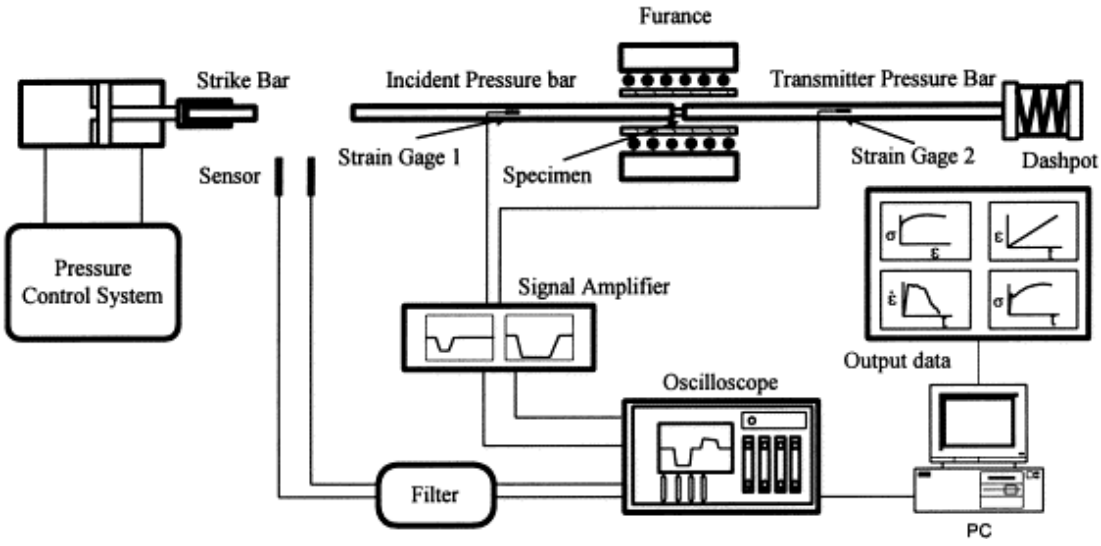

Figure 5.8 A detailed presentation of the split Hopkinson pressure bar apparatus [58].

Pressure bars should be constructed from a high-strength material; AISI 4340 steel or maraging steel are common choices. The yield strength of the pressure bar determines the maximum stress attainable within the deforming specimen, because the cross-sectional area of the specimen approaches that of the pressure bar during deformation. The length, l_{bar}, and diameter, d_{bar}, of the pressure bars are test variables. The diameter chosen depends on the strain rate desired; the highest strain rate tests require the smallest diameter bar. The length of the pressure bars is determined by conditions required for one-dimensional wave propagation, which requires approximately 10 bar diameters. Thus, each bar should exceed an l_{bar}/d_{bar} ratio of 20.

A second consideration affecting the bar length is the amount of strain desired in the specimen, which is related to the length of the incident wave. The pressure bar must be at least twice as long as the incident wave if the incident and reflected waves are to be measured independently. To obtain strain as high as 25%, it may be necessary to specify an ratio l_{bar}/d_{bar} of 100 or more.

Another important consideration for the pressure bars is the minimization of axial curvature. This can be a particular problem for materials that are hardened by heat treatment and for bars with high aspect ratios. However, optimum alignment is essential to the split Hopkinson pressure bar test technique, and the amount of curvature within the pressure bar affects the alignment. [34]

Accurate bar alignment is required for ideal one-dimensional wave propagation within the pressure bars and for uniaxial compression within the specimen. However, alignment cannot be forced by over constraining the pressure bars, because this violates the boundary conditions for one-dimensional wave propagation in an infinite cylindrical solid. This is one reason for a tight specification on curvature in the pressure bars. Generally the pressure bars are mounted to a rigid beam. Mounting brackets with bearings, through which bars pass, are spaced every 100 to 200 mm, depending on the bar diameter, and are designed so that each can be individually translated for alignment adjustment.

An optical bore scope at the near end of the beam is used to set and regularly verify alignment. The bearings in the mounting brackets should designed such that the diameter should be greater than the bar diameter to allow radial expansion. A simple check of alignment is to verify that each pressure bar translates and rotates freely through the mounting brackets and that faces of the incident and output bars meet identically when brought together without the specimen in place. [34]

Generating the Incident Wave is another consideration of the split Hopkinson pressure bar test. The most common method of generating the incident wave is to propel a striker bar toward the incident bar. Waves also can be generated by the detonation of explosives at the free end of the incident bar. However, it is more difficult to ensure a one-dimensional excitation within the incident bar using explosive techniques.

For the striker bar configuration, the projectile can be propelled using stored elastic energy of, for example, a spring, but the use of a gas gun is most common. The striker bar is fabricated from the same material and is of the same diameter as the pressure bars. The length and velocity of the striker bar are chosen to yield the desired total strain and strain rate within the specimen. At a constant strain rate, the maximum strain in the specimen is directly proportional to the length of the striker bar, l_{stbar};

$$\varepsilon = 2\dot{\varepsilon}\frac{l_{stbar}}{C_0} \tag{5.29}$$

From inspection of Equation 5.29 and consideration of momentum conservation between the striker and incident bars, it can be shown that;

$$\dot{\varepsilon} \leq \frac{V_0}{l_s} \tag{5.30}$$

where V_0 is the velocity of the striker bar. The equality condition in Equation 5.30 is approximated for soft metals at high impact velocities. Equation 5.29 and 5.30 can be used to approximate the striker bar length and velocity required for a desired strain and strain rate.

The need for a long rise time pulse was discussed above concerning the conditions required for the equilibration of stress within the specimen. Experimentally, the rise time of the incident wave can be increased by placing a soft, deformable disk at the striker bar/incident bar interface. The choice of material and thickness for this disk depends on the strain rate and the strength of the specimen. Typically, the disk is the same material as the specimen and is 0.1 to 2 mm thick. An additional benefit of this layer is that it often provides a more uniform strain rate experiment.

It should be mentioned here that, in the normal SHPB method the strain and strain rate are dependent on the relative impedances of the bars and specimen, and on the speed of projectile; tests over a range of strain rates are achieved by changing the projectile speed. An average strain rate is ascribed to each test by dividing the total strain during loading by its time of application. However, this averaging masks the detailed behavior since during a test the instantaneous strain can be appreciably higher than the average because of the shape of the loading pulse [49].

Friction is an important consideration in all compression testing. The optimum l_{bar}/d_{bar} ratio for a split Hopkinson pressure bar compression test specimen is approximately one half that determined to be most favorable for the minimization of errors due to friction [34]. Thus, lubrication is required at the specimen/pressure bar interfaces. However, the presence of a layer of lubricant at these interfaces can affect the timing between the waves recorded on the incident and output pressure bars.

For example, consider the test of a 5 mm long specimen at a strain rate of $5 \times 10^{1}\ s^{-1}$. Equation 5.30 indicates that, for these conditions, the projectile velocity, and thus the particle velocity in the incident bar, must be at least 25 m/s. For a 25 μm layer of lubricant at the specimen/incident bar interface, approximately 0.5 μs is required for the incident bar, traveling at this velocity, to contact the specimen. There will be a similar delay at the specimen/output interface. These delays are not negligible and can alter the timing relation between the reflected and transmitted waves used to

compute stress and strain within the deforming specimen. Consequently, it is important to maintain a thin layer of lubricant.

The use of an oil-based molybdenum disulfide lubricant is successful for room temperature testing. Typically, the lubricant is applied to the faces of the specimen, and the excess is lightly removed. For elevated temperature tests, a thin layer of fine boron nitride powder can be used to lubricate the specimen/pressure bar interfaces.

Measurement of Displacement in the Pressure bars is also important in split Hopkinson pressure bar testing. Equations 5.25 showed that the strain rate and stress within the samples are related to axial strains in the pressure bars, and it also was shown that, for conditions of most split Hopkinson pressure bar tests, the surface strains accurately reflect the axial strains. There are two common techniques for measuring these strains. The use of strain gages is most popular. Two gages generally are mounted at diametrically opposite positions on each bar and connected so as to average out any bending strain. Standard strain gage technology has been successful. The major difficulty has been the development of techniques to attach lead wires to the strain gages. These lead wires experience large accelerations and can easily break when the stress wave passes.

The location of the strain gauges is important so that continuous records can be obtained of each pulse without interference from reflections. For this reason the gauges are positioned so that the distance between each gauge and the ends of their respective pressure bars is greater than the length of the striker bar. On the incident pressure bar this allows the complete incident pulse to be recorded as well as the reflected pulse [33]. The strain gage on the output bar is bonded at the same distance from the right end of the bar but near the specimen. This way, a shorter bar can be used because only one wave is measured [50]. Typical strain vs. time records from the pressure bars can be seen in Figure 5.5.

Bonded strain gages do have a finite response capability. The rise time of the gage in response to a step change in displacement increases with the length of the strain gage. Typically, gages attached to pressure bars may be expected to have response times less than 1 μs, which is sufficient for conditions of the split Hopkinson pressure bar test.

Another device used to measure strain in the pressure bars is the coaxial condenser or capacitor. Although the advance in strain gage technology has all but eliminated the use of condensers in the split Hopkinson pressure bar configurations, their use continues for the single pressure bar configuration.

The instrumentation required for the split Hopkinson pressure bar test includes two strain gage signal conditioners and a means of recording these signals. The strain gage signal conditioners must have a frequency response of at least 1 MHz and as high as 10 MHz. Until recently, oscilloscopes were used almost exclusively to capture and record the pulses. The reflected wave may be fed through an analog integrator to yield a signal proportional to strain. Thus, the transmitted wave and integrated reflected wave can be fed to an oscilloscope with x-y capability to directly yield the stress-strain curve.

With the advent of precise, high-speed analog to digital recorders, it is possible to digitize the raw data directly and perform the integration numerically. The availability of the digitized data also facilities adjustment of the timing between the transmitted and reflected waves to account for the transit time through the specimen; this is described in more detail in the section of this study on test limitations.

For the calibration of the system, there are three methods proposed. The first method is to make the calibration of the data-acquisition system. In this method firstly the incident bar without output bar and specimen is tested. The maximum strain occurred in the bar can be calculated as follows;

$$\varepsilon_{b\max} = \frac{V_0}{2C_0} \tag{5.31}$$

where, V_0 is the striker bar velocity. Thus, measuring the strain at the bar the system is checked. Then the output bar added to the test without specimen. Both strains are measured and the system is calibrated again. The second method is to control the uniformity of deformation. For this purpose, it is checked if the total of reflected and incident strains equal to the transmitted strain. Also the uniformity of the deformation can be observed by a numerical solution [43, 44]. The last method is to compare the maximum deformation occurred in the test by measuring the final length of the specimen by a micrometer. [12]

5.2.7. Limitations

Strong interest in the effect of strain rate on mechanical properties has led to the application of split Hopkinson pressure bar testing techniques at strain rates that are at the limit of, and perhaps beyond, conditions for a valid test. Some necessary conditions for a valid test are given in Equations 5.26 to 5.30. However, these expressions are only approximate and do not guarantee accurate test results. The

basic limitation is the condition of uniform deformation within the sample. It has been emphasized that this problem cannot be circumvented simply by decreasing the length of the sample, because the aspect ratio of the specimen is specified by consideration of frictional constraint and the balancing of error due to radial and axial inertia [34].

As discussed above SHPB technique fails in two testing situations because the maximum strain attained is insufficient. One case is when the desired maximum strain (or total relative displacement) is very important. For example, in the study of the dynamic behavior of polymeric or metallic foam, the desired maximum strain is often up to 80% to investigate the densification phenomenon of those materials. A large displacement during the test is also required for the study of the dynamic buckling of thin metallic tubes. In fact, specimens are effectively submitted to the desired strains (because of their low resistance) during the total time remaining after the observation window, but measurements are no longer possible after this time limit in a standard SHPB [51]. So some modifications should be made. An example study for polymeric materials SHPB testing can be found in [52]. Another case is when the desired strain rate is in the medium rate (5-50 s^{-1}). The technique cannot be applied because the maximum measurable strain becomes too small.

Determination of test validty in the split Hopkinson pressure bar experiment has stimulated a number of analyses of wave propagation in the split Hopkinson pressure bar test configuration. The most extensive of these was a two-dimensional finite difference analysis. This analysis considered the effects of wave shape, friction, strain rate, and length to diameter ratio [34].

The optimum design of a split Hopkinson pressure bar test would call for a long rise time during the elastic loading of the specimen so that the specimen would be deforming uniformly when the yield stress was reached. However, this is rarely possible to achieve, and at high strain rates it is likely that the data may not be valid until a strain of 5 or 10% is achieved. The problems associated with establishing uniform deformation within the sample make it very difficult to accurately determine the dynamic yield strength using the split Hopkinson pressure bar.

The timing between the reflected and transmitted waves strongly affects interpretation of the test results at high strain rates. Typically, strain gages are placed equidistant from the sample, and it is assumed that these waves arrive at the respective strain gages at the same instant. There are two sources of error that affect this assumption. The first is the transit time through the specimen, which is

determined by the elastic sound velocity and the specimen length. This error is predictable, decreases with the bar diameter (for a constant aspect ratio specimen), and is easily incorporated into the data reduction procedure.

However, another source of error is the transit time at the imperfect specimen/pressure bar interfaces. This error is far less reproducible, does not scale with bar diameter, and may be as large as 1 or 2 μs. Uncertainty in the timing between the reflected and transmitted waves affects the predicted stress-strain curve, because the strain and stress are derived from these signals. This error increases the uncertainty in the measurements as the strain rate increases and sets the practical limit of split Hopkinson pressure bar testing closer to a strain rate of 10^4 s^{-1} than to 10^5 s^{-1}.

5.2.8. Other techniques of Hopkinson bar

The Hopkinson bar is also used in tension, torsion and shear. A number of experimental fixtures have been developed, and some of them are shown in Figure 5.9a (for tension). In Figure 5.9(b) the compressive pulse ''bypasses'' the specimen because of a collar. It is allowed to reflect at a free surface and returns as a tension pulse. Another arrangement, using an inertial bar, is shown in Figure 5.9(c). The striker tube (on the left) impacts the main tube, causing a compression pulse. This compression pulse acts on the specimen, pulling it to the right. The inertial bar counteracts this. The result is tension acting on the specimen.

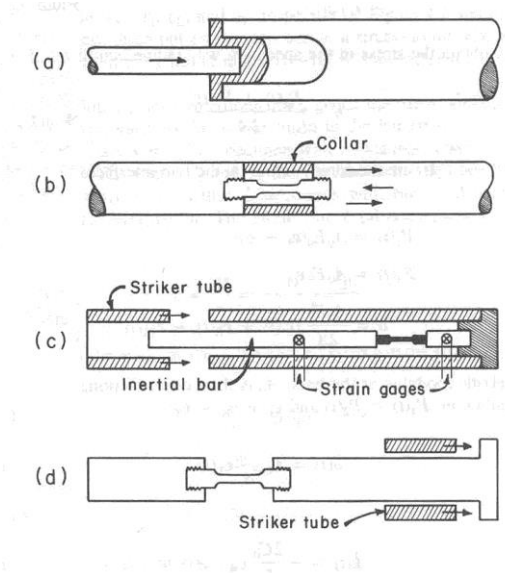

Figure 5.9 Some setups for testing specimens in Hopkinson bar in tension mode: (a) hat-shaped specimen; (b) collared specimen; (c) inertial-bar configuration; (d) collar impacting bolt head [1].

For shear stress-shear strain data, torsional bar (Figure 5.9(a))is the proper instrument. Torsional energy is released by braking a clamp. A tubular specimen is sheared by this wave. One can also create shear stresses in a split Hopkinson pressure bar by using a hat-shaped specimen, shown in Figure 5.10 (b).[1]

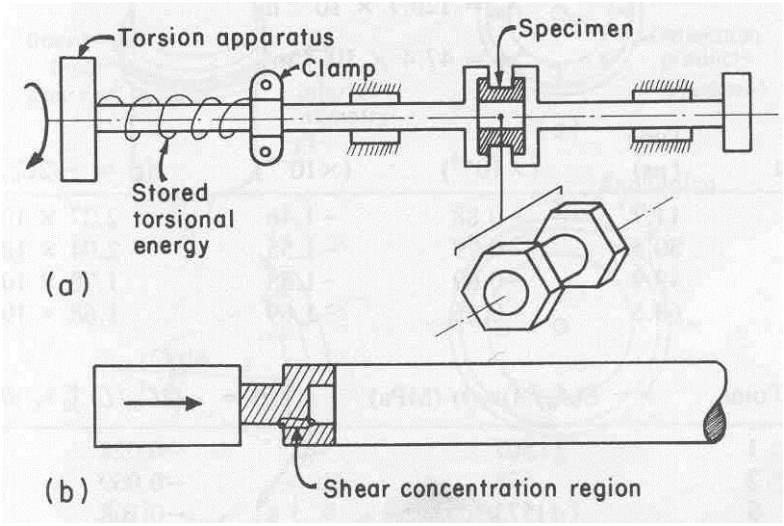

Figure 5.10 (a) Torsion Hopkinson bar for pure shear configuration; (b) hat-shaped specimen for shear stresses in split Hopkinson Pressure Bar [1].

5.3. Other high strain rate experiments

5.3.1. Rod Impact (Taylor) Test

The main aim of the Rod Impact Testing is to determine high strain rate constitutive behavior of materials. In 1947 the first method was that (Figure 5.11(a)) a rod was accelerated into a ''rigid'' plate. The plastic deformation at the impact end shortens the rod, and the fractional change in rod length can, by one-dimensional rigid-plastic analysis, be related to the dynamic yield strength. This relationship was shown to be independent of both the rod aspect ratio and the impact velocity for a wide variety of materials, including copper, lead, and various steels [34].

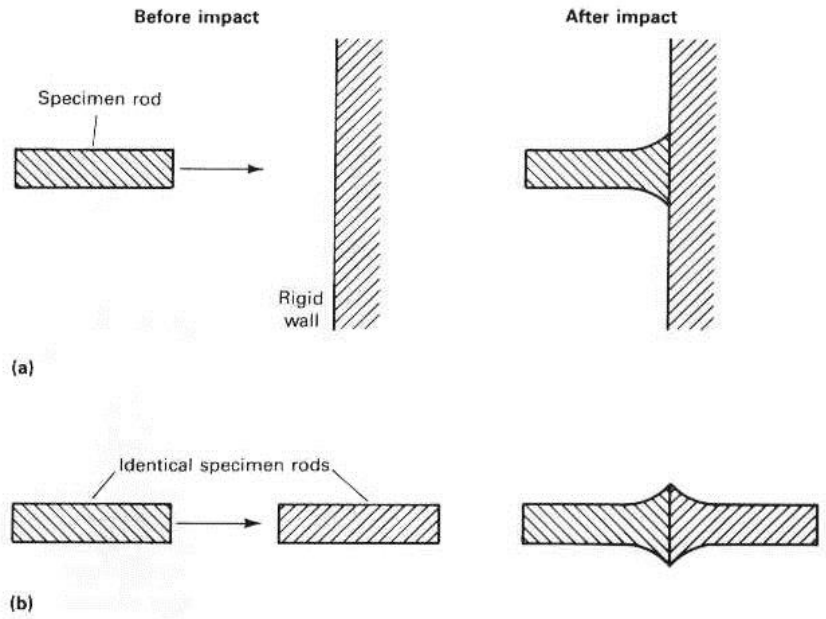

Figure 5.11 Symmetric rod impact tests at ambient temperature [1].

Twenty-five years after the original Taylor tests, the use of two-dimensional wave propagation codes enabled a better understanding of and renewed interest in this technique. In 1972, Wilkins and Gunian [53], using a two dimensional finite difference code and an elastic-plastic model with work hardening, were able to correctly simulate the final shapes and final lengths of Taylor test specimens of several metallic alloys at ambient temperatures. Their results showed good correlation between the dynamic yield strength and the fractional change in rod length for a wide range of impact velocities and rod aspect ratios, thus confirming many of the original test conclusions.

Recently, Symmetric and Asymmetric types of Rod Impact Testing is developed. The Symmetric Rod Impact Testing has importance because of the main modification that was made the fundamental changes. This was the second modification of the Taylor Test. The second modification was to replace the rigid plate with another rod of the same geometry and the material as the impacting rod (Figure 5.11(b)). This arrangement allows the impacting ends of the two specimen rods to deform together symmetrically, thus eliminating boundary condition uncertainties in the analysis that arise from the unknown friction conditions at the rod/plate interface and from the deformation of the rigid plate adjacent to that interface.

In both symmetric and asymmetric rod impact tests, the heater assembly (for elevated temperature tests) and the specimen recovery pipe are placed in near the muzzle of the gas gun. The target alignment plate is adjusted so that it is concentric

with that of the gun barrel, and on it the target assembly containing the specimen rod is mounted, positioned to be concentric with the front target support plate. The projectile is inserted at the breech of the gun, and the target chamber is closed and evacuated to desired pressure. The gas gun breech is then pressurized, and the specimen is preheated to the desired temperature. The firing sequence then begins. The deformation during the experiment is recorded by a high-speed camera. Then the profiles of the deformed rods (Figure 5.12) are digitized for subsequent comparison with computer simulations.

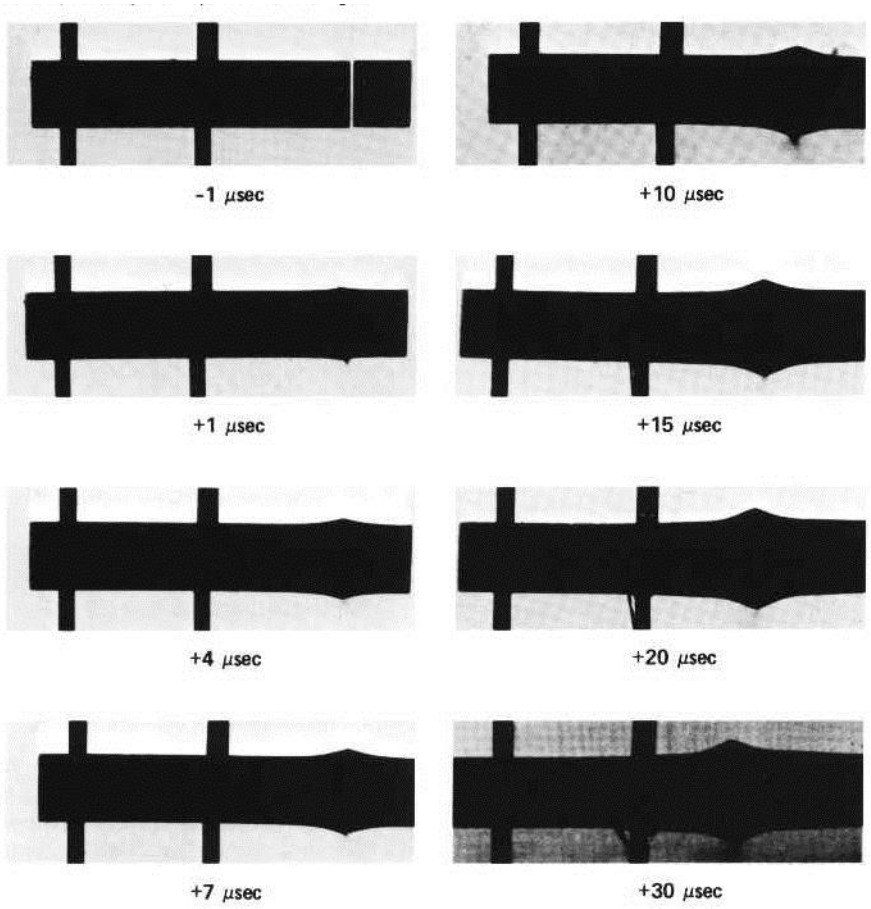

Figure 5.12 Silhouettes of 4340 steel rods during symmetric impact at 457 m/s [34]

Determination of the dynamic flow curve of a material from a rod impact test is made by computationally simulating the experiment with a two-dimensional wave propagation computer code. The flow parameters are varied until the computed profiles agree with those determined experimentally at various times during the deformation history.

The specimen rods are divided into a series of rectangular zones, or computational cells, each of which, in the cylindrical geometry appropriate to the rod impact test, represents an annulus of revolution about the rod axis. The corners, or rods, of the cells are given an appropriate initial velocity. Then the subsequent node velocities and the resulting rod deformation are determined by solving the Lagrangian equations of motion for a continuous medium. Figure 5.13 shows the original, an intermediate, and the final cell profiles for a typical test simulation.

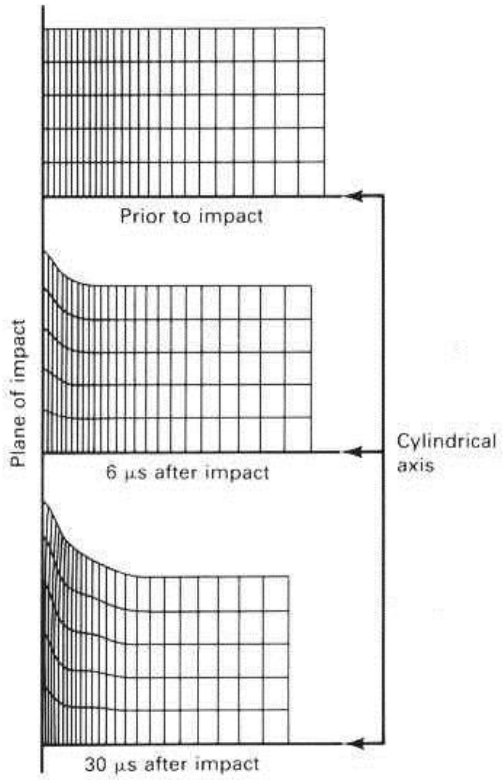

Figure 5.13 Cell outlines at three times during simulation of symmetric rod impact [1].

A rate-independent elastic-plastic model with work hardening is used to describe the plastic deformations in each cell. Various flow curves are tried. A quasi-static compressive or tensile flow curve is a good starting point because there are few dynamic curves to be found in the literature. The computed results are then compared with the experimental results until agreement within the experimental error is obtained.

Computer simulations have confirmed that the plastic strain rate, as well as the total strain and the temperature resulting from the local plastic work, varies significantly as a function of time and axial and radial position within the specimen rod. For a particular axial location, strain rates (either peak or average) along the rod axis are

often three to four times higher than those near the periphery. Also, there is often an order of magnitude difference in the strain rates among locations near the impact interface and locations one-rod diameter distant.

The experimentally measured rod thickness at a particular axial position is not the result of a region of material undergoing deformation at a specific strain rate, but rather the result of various regions of material deforming at a range of strain rates. Therefore, the rod impact technique should not he viewed as a method for accurately determining the strain rate sensitivity of the flow curve over the range of strain rate observed in the test, namely between about 10^4 and 10^5 s^{-1}, but rather as a means of determining the average flow curve over that range.

5.3.2. Expanding ring test

The other common method in high strain testing is Expanding Ring Test. The main difference of this test from others is that, the load type is tension in this technique. The expanding ring test is a highly sophisticated technique for subjecting metals to tensile strain rates over 10^4 s^{-1}. Although the testing principle is simple, its performance requires specialized equipment available in only a few laboratories. The ring test can determine the high-rate stress-strain relationships, but a simplified, more widely used version can be employed to determine ultimate strain only [54].

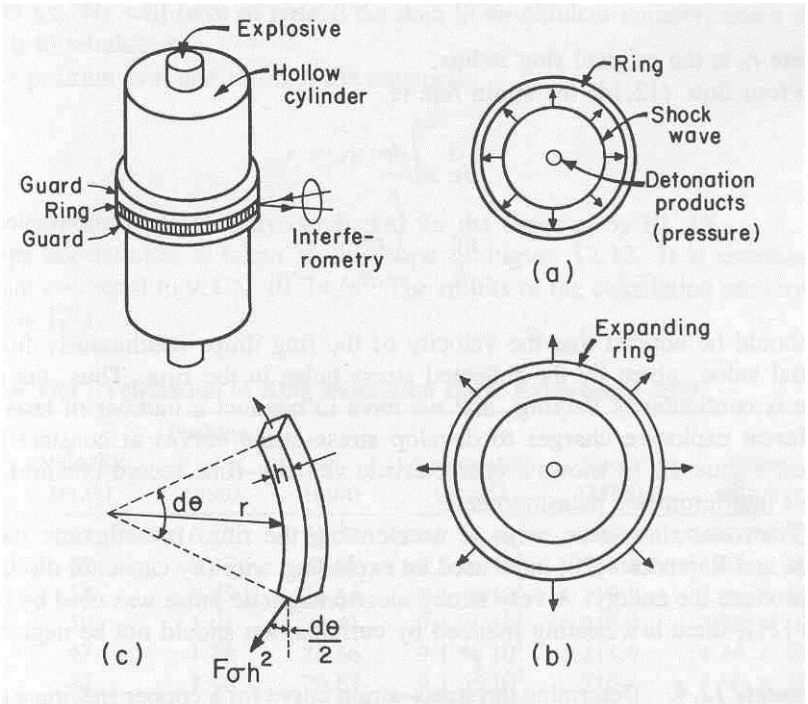

Figure 5.14 Expanding ring technique: (a) steel block with explosive in core; (b) sections of cylinder just after detonation and during flight of ring; (c) section of ring [1].

Figure 5.14 shows a possible arrangement of the expanding ring. The steel cylinder has a core, in which we detonate an explosive. A shock wave travels outward and enters the metal ring, propelling it in a trajectory with an expanding radius (Figure 5.14(c)). By measuring the velocity history of the expanding ring by laser interferometry, one can determine the stress-strain curve of this ring at the imposed strain rate. The mathematical derivation of these equations is straightforward and is given below. Let us consider a small segment of a circular ring with radius r [Fig. 5.14(c)]. The ring is subjected, during flight, to Newton's second law, just like any other moving object. The stress acting on the ends of this segment is σ. If the instantaneous cross-sectional area is A, the force is σ_A. If ρ is the density of the material, we have:

$$F = ma$$

$$2F \sin\frac{d\theta}{2} = \rho A r d\theta \ddot{r} \qquad \text{(Eqn. 5.32)}$$

yielding to:

$$\frac{d\varepsilon}{dt} = \frac{1}{R}\frac{dR}{dt} \qquad \text{(Eqn. 5.33)}$$

To obtain stress-strain data, radial displacement as a function of time must be calculated. Ring displacement can be obtained through the use of high-speed photography, streak cameras, displacement interferometers, or other methods for measuring radius as a function of time.

The ring test has two principal advantages. The expanding ring test subjects the material to a state of dynamic uniaxial stress without the wave propagation complications that accompany other high strain rate tests. Also, the maximum strain rate available in the ring test is higher than in any other common tension tests involving large plastic strains.

Strain rate in the expanding ring test is not usually constant. The strain rate is computed from $(dR/dt))/R$, and both of these terms vary continually. Strain rate is usually greatest at the start of ring deceleration, when strain is smallest. Values in excess of 10^4 s^{-1} are readily obtained. If the ring does not rupture, the strain rate falls to zero at the end of the test.

Ring specimens also experience a compressive preload in the radial direction that often exceeds the yield stress during the acceleration phase. Because load history is known to affect the subsequent stress-strain behavior of many materials, data obtained from expanding ring tests do not always agree with results from other tests at slightly lower strain rates.

The difficulties, expense, and limitations of the expanding ring test preclude its use as a standard test technique for generating high strain rate stress-strain data in tension. However, if subjecting a material to high strain rates in tension without determining stress-strain data is of primary interest, the expanding ring test is much easier to conduct. Here, the accurate determination of radial displacement versus time is not as critical, because stresses are not calculated. Less precise displacement data provide reasonably accurate determinations of strain rate. The ambiguity arising from possible strain rate history effects still exists when the expanding ring test is used in this simpler manner.[1]

5.4. Reasons for the Selection of SHPB Test for the Study

Firstly it should be mentioned that, at the beginning of the literature review Split Hopkinson pressure bar is found to be the most used experimental method for obtaining high strain rate behavior of materials, in this area of research. After having further knowledge about the subject, the split Hopkinson pressure bar test is selected for design because of the following reasons:

- Since split Hopkinson pressure bar test is the first developed one among others, there have been numerous researches on this technique. Thus, the principle and weaknesses of the technique is well understood. Also relatively more literature source is available.
- The main difference of the Split Hopkinson pressure bar among others is that, we do not consider the wave propagation in the specimen, but in the pressure bars. So we do not need to deal with the plastic waves, instead the elastic wave theory became major subject in the evaluation. Moreover, elastic wave theory is more developed and easier to understand than the plastic theory. Also computation of elastic behavior variables is relatively easier.
- As discussed earlier, in split Hopkinson pressure bar test one-dimensional wave propagation is enforced. So theory of the test is the most understood and developed one due to the easiness of equations of one-dimensional wave theory.

- Recently, the instrumentation for measuring elastic deformation is easier and cheaper than the instrumentation for measuring plastic deformation. Thus data acquisition became easier and faster. It should be noted that there is a huge difference between instrumentation price for measuring elastic and plastic deformation.
- Also the apparatus of the split Hopkinson pressure bar is relatively easy to modify for different type of material testing.

6. DESIGN OF A SPLIT HOPKINSON COMPRESSION BAR APPARATUS FOR TESTING STEELS UNDER DYNAMIC LOADING

The detailed structure of split Hopkinson pressure bar testing was discussed in Chapter 5. It can be clearly understood that some components of the test are coupled with each other, in terms of design issues. These components are specimen, striker, incident and output bar. Therefore these components should be designed according to the desired material. All the other components such as gas gun, support system, and other data instrumentation are stationary. In this chapter the design of a split Hopkinson Pressure bar testing for steels is made.

The selected strain rate range is between 10^3 s^{-1} - 10^4 s^{-1}, and the design is made so that the maximum strain is obtained at the specimen, which is between 20 % 25 % for the SHPB test.

6.1. Design of Specimen and Pressure Bars

The length and the diameter of the cylindrical specimen are selected based on the literature review [55-62] and the l_s/d_s ratio (which is 0.5) to minimize the friction effects. The dimension of the specimen can be seen in Figure 6.1.

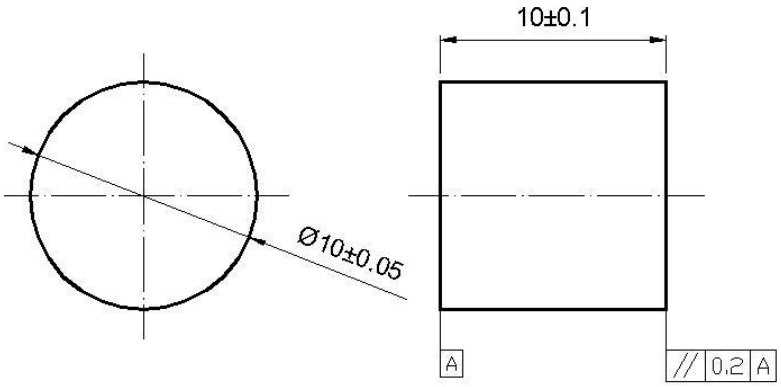

Figure 6.1 Cylindrical specimen dimensions for SHPB

Our suggestion is to make the specimen diameter as a variable for observing the effects of l_s / d_s ratio on the results.

The material of the bars is selected as AISI Grade 350 Maraging steel, which has a yield strength of 2500 MPa, elasticity modulus of 190 Gpa and density of 8 g/cm^3. The velocity of elastic wave in bars can be calculated as follows;

$$C_0 = \sqrt{\frac{190x10^6}{8}} = 4873 m/s$$

As mentioned before permanent deformation in bars should be avoided. Moreover the maximum strain occurred in the bars is calculated as follows;

$$\varepsilon_{b\max} = \frac{\sigma_y}{E} = \frac{2500}{190x10^3} = 0.013$$

Also from Equation 5.31, the allowable striker bar velocity can be calculated as follows;

$$V_{0\max} = 2x0.013x4873 = 127 m/s$$

The length of the striker bar can be calculated by the equations 5.29 and 5.30;

$$\text{for } \dot{\varepsilon} = 10^4/s,\ l_{striker\,bar} \geq 48mm$$

$$\text{for } \dot{\varepsilon} = 10^3/s,\ l_{striker\,bar} \geq 480mm$$

So the length of the striker bar is selected as 480 mm. To satisfy the propagation of one-dimensional elastic wave propagation R_{bar} / λ value should be too much smaller than 1, where λ is the wavelength and equals to $2l_{striker\,bar}$. The value of R_{bar} / λ is selected as 0.01. So the diameter of the bars can be calculated as follows;

$$\frac{R_{bar}}{2l_{striker\,bar}} = 0.01 \Rightarrow R_{bar} = 9.6mm \Rightarrow d_{bar} = 19.2mm$$

Now lets calculate the final diameter of specimen after deformation to see if the diameter of the bars is adequate to ensure the full contact at the final diameter. Note that the final diameter of the specimen is calculated with regard to the desired maximum strain, which is 25%.

$$\varepsilon = \ln(\frac{l_{final}}{l_0}) = 0.25 \Rightarrow l_{final} = 7.786mm$$

Now the final specimen diameter can be calculated according to constancy of volume as follows;

$$\frac{\pi d_0^{\,2}}{l_0} = \frac{\pi d_{final}^{\,2}}{l_{final}} \Rightarrow d_{final} = 11.33mm$$

It can be seen that selecting the bar diameters as 19 mm would both ensure full contact of bars and specimen and satisfy one-dimensional elastic wave propagation.

Therefore the length of the bars can be calculated as follows to enforce the maximum strain;

$$\frac{l_{bar}}{d_{bar}} = 100 \Rightarrow d_{bar} = 1900mm$$

Note that since only one wave is measured at the output bar the length of the bar can be smaller than the incident bar. So the length of the output bar can be selected as 1500 mm.

The designed dimensions of the specimen and bars are summarized in the table below.

Table 6.1. SHPB Component dimensions

Component	Length (mm)	Diameter (mm)
Specimen	10	10
Incident bar	19	1900
Output bar	19	1500
Striker bar	19	480

6.2. Assembly and Other Components

In figure 6.2, the schematic view of SHPB apparatus can be seen. The range between bearings is selected as 250 mm and between ground supports is selected as 500 mm. The strain gages are located 1 m far from the specimen on the two bars.

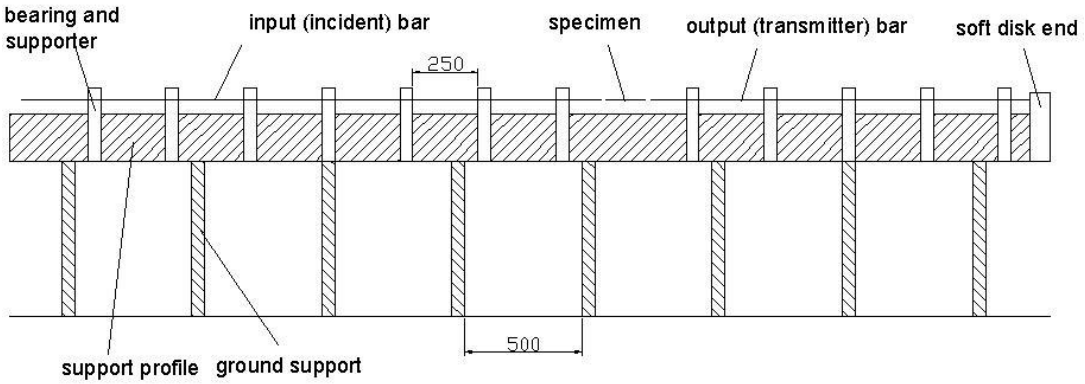

Figure 6.2 Schematic view of components of SHPB

The support profile is the supporter for the whole system. The dimensions of the support profile are selected as in Figure 6.3.

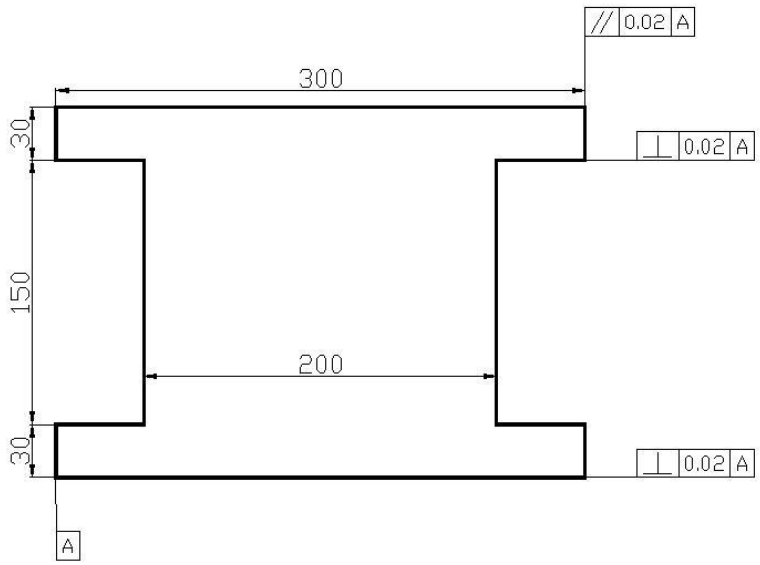

Figure 6.3 The dimensions and geometry of the support profile

The length of the support profile is selected as 4000 mm, in order to handle specimen, input and output bar and the soft end. Also the material of the profile is selected as St 50. Since the alignment of the system is very important in order to satisfy one-dimensional wave propagation, the flatness of the upper and lower faces should have close tolerances, which is selected as 0.02 mm.

Another component in the apparatus is the bearing supporter. The designed dimensions and geometry of the bearing supporter can be seen below in Figure 6.4

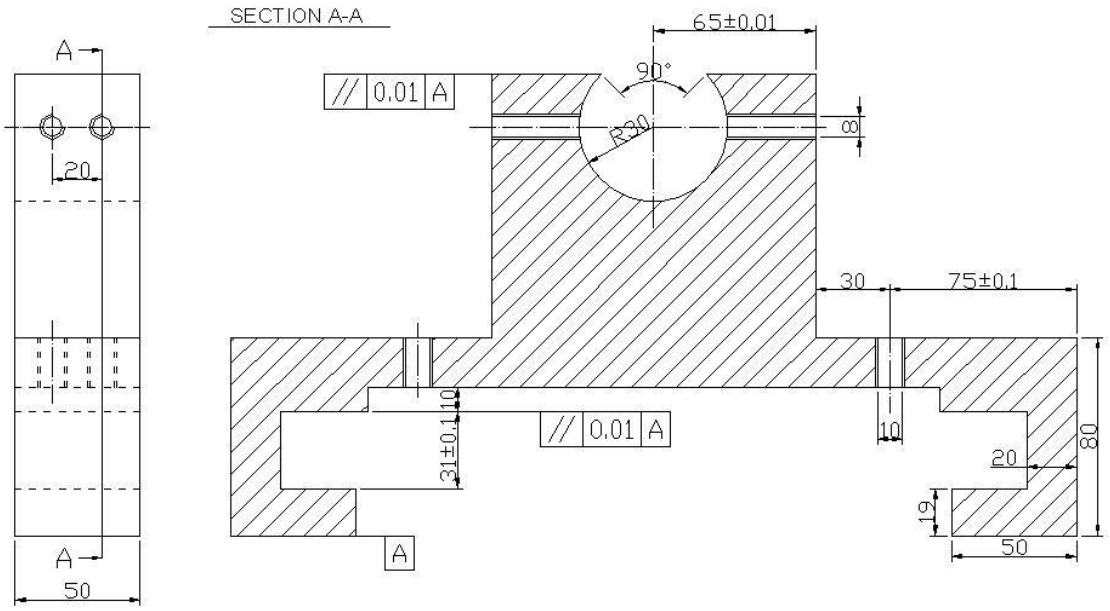

Figure 6.4 The dimensions and geometry of the bearing supporter.

The material of the bearing supporter is selected as St 37. The diameter of the location, where bearing is mounted, is selected as 60 mm, which is much higher than bars' diameters. This selection is made for the system flexibility. For other experiments, the bars' dimensions can be changed and with the suitable bearing this supporters can be used again.

The designed linear bearing for the actual bar dimensions can be seen in Figure 6.5. The material of the bearing is selected as teflon.

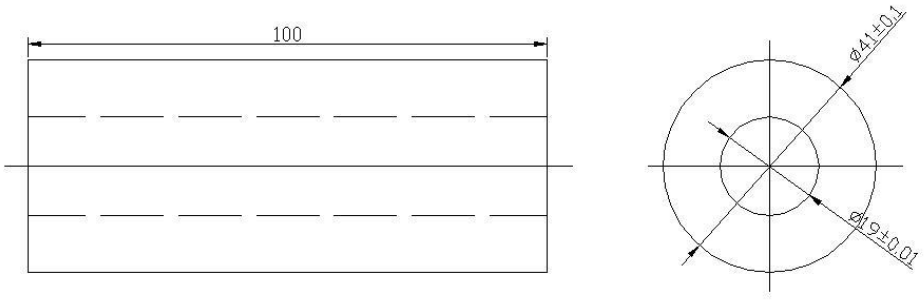

Figure 6.5 Linear bearing dimensions.

The assembly of the bar with bearing and the bearing with supporter systems can be seen in Figure 6.6. The bar is assembled with the bearing by a clearance fit of 0.1 mm. The bearing is mounted to bearing supporter by 4 bolts, 2 replaced at two sides. This is done to arrange the horizontal alignment of the bars. The bearing supporter is mounted to the support profile by a middle supporter and 4 bolts. The material of the middle supporter is selected as St 37. There are two reasons to use this middle supporter. The first reason is to avoid the ware of support profile upper face, because it is machined to be flat and parallel. The second reason is to arrange vertical alignment of the bars with the nuts. A dial indicator is used to check alignment of the bars.

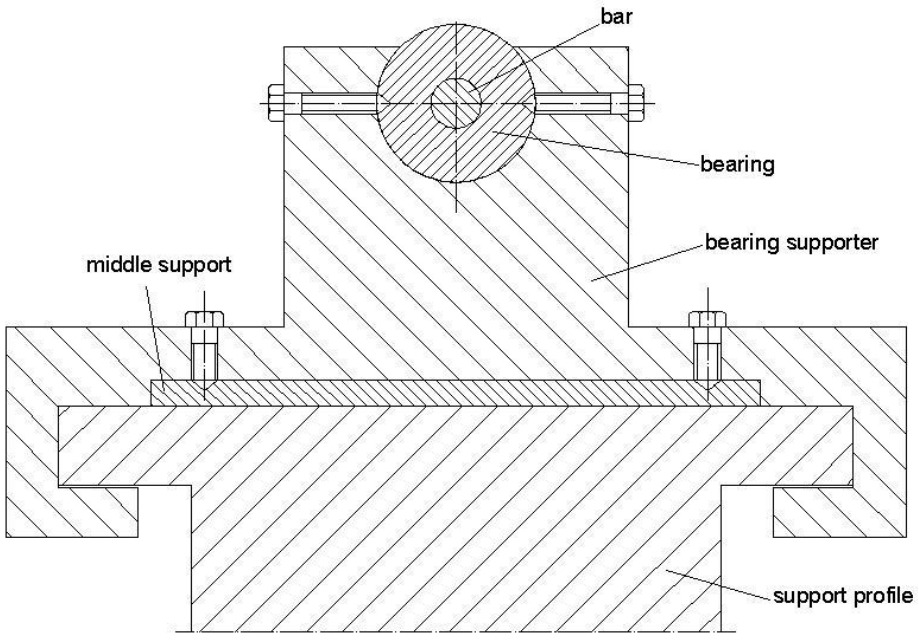

Figure 6.6 Assembly of bearing components and bar.

A ground support with a square cross section is used for standing the apparatus. A schematic view of this arrangement can be seen in Figure 6.7. The ground support components are mounted with welding and ground support is mounted to the support profile by two nuts.

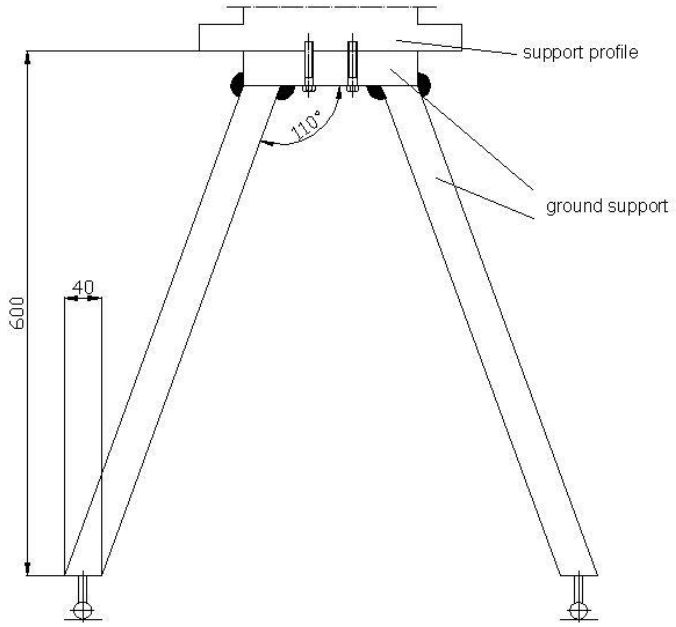

Figure 6.7 Schematic view of support profile and ground support assembly.

A detailed view where the ground support meets ground can be seen in Figure 6.8. Two-nut system is used between the ground support and wheel. This is done to arrange alignment of the support profiles. This alignment is checked by a spirit level.

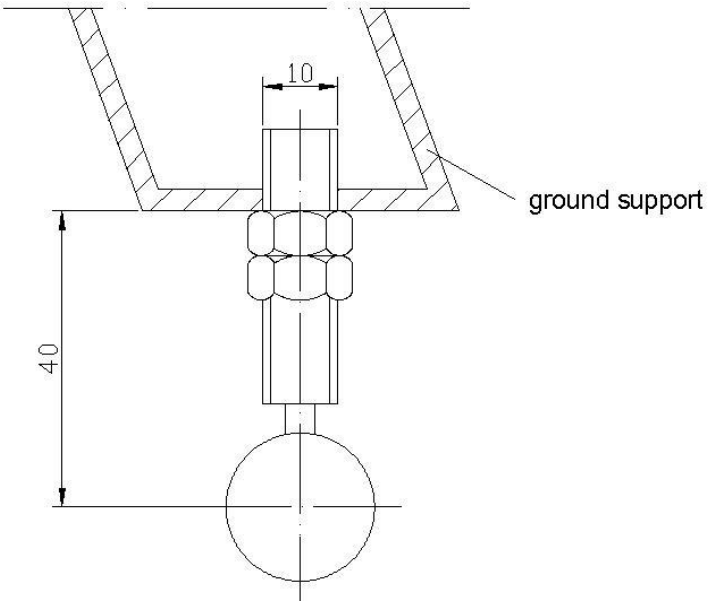

Figure 6.8 the detail of ground support end.

At the end of the system, the output bar meets with a cylindrical soft disk of a polymeric material with a diameter of 60 mm. The soft disk support component can be seen in Figure 6.9. The soft disk is mounted to the component by four nuts, two replaced at two sides.

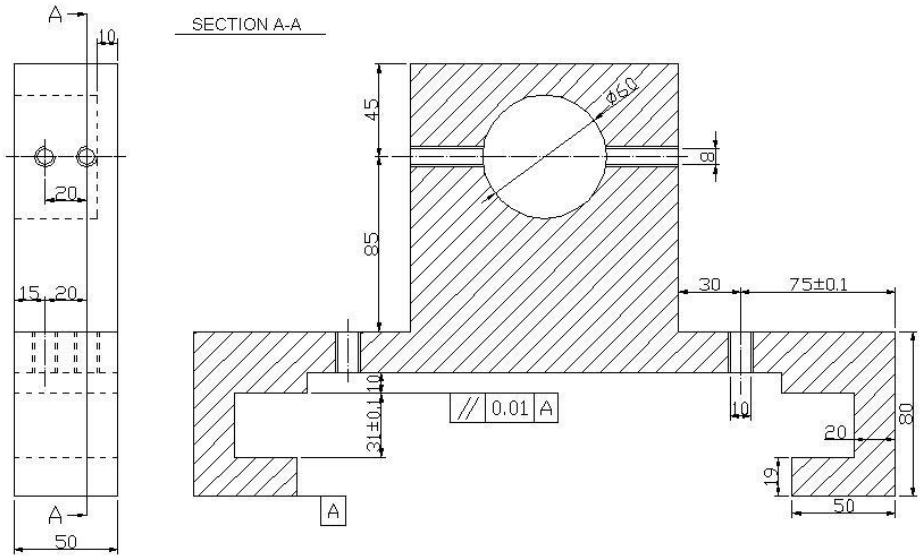

Figure 6.9 Soft disk support component.

To arrange the alignment of the specimen, the tool seen in Figure 6.10 is desigined. Firstly, the specimen is replaced to the output bar with the help of this stod. Then the input bar meets the specimen. And then the tod is pulled out. The specimen stands in its place by lubricant, which is selected as molybdenum disulfide by a literature review. The cross-section is selected as semi-circle to make pull out non-destructive.

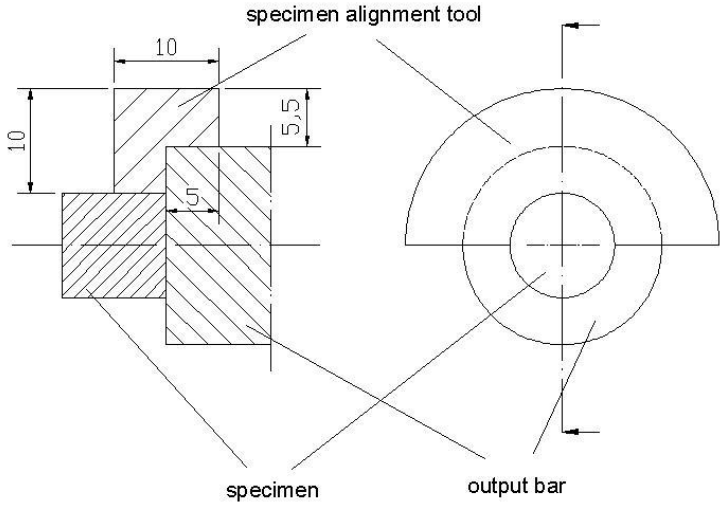

Figure 6.10 Specimen alignment tool.

6.3. Gas Gun

Two mostly used systems are proposed for the gas gun. The first system can be seen in Figure 6.11. There are three major parts: a breech containing gunpowder; a pump tube filled with a light gas, typically hydrogen; and a barrel for guiding a high-velocity projectile to the target. When the projectile hits the target, the impact produces a high pressure. These types of guns are driven in two stages, first with gunpowder and then with a light gas such as hydrogen, helium, or nitrogen. The smaller guns can also be used as a single-stage gun driven only by gas. Hot gases from the burning gunpowder drive a heavy piston down the pump tube, compressing hydrogen gas. This gas, the second-stage driving medium, is compressed before the gas breaks the rupture valve. The gas then accelerates projectile down the barrel to a muzzle.

Hydrogen is used as the second-stage driving gas because it produces the highest projectile velocities, ranging from 4 to 8 kilometers per second. When hydrogen is used as a single-stage gun, the velocities of the smaller guns range from 100 meters per second to 1 kilometer per second. Velocities are determined by carefully selecting the gun firing parameters: the type and amount of gunpowder, the driving gas (helium and nitrogen are used for velocities below 4 kilometers per second), the pressure required to open the rupture valve, the diameter of the barrel, and the mass of the projectile. Note that in our system the desired velocity of the striker bar is 127 m/s. So a single stage gas gun driven with hydrogen will be enough for the system[63].

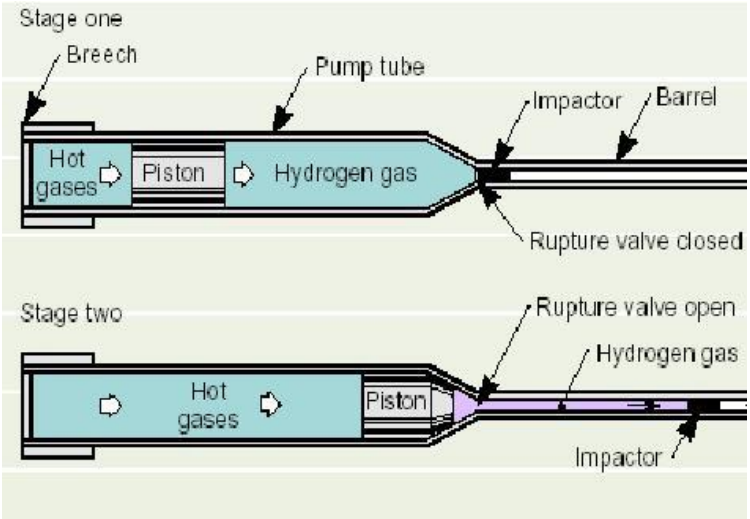

Figure 6.11 Two-stage gas gun [63].

Another proposed gas gun system could be seen in Figure 6.12. This gas gun consists of four major components. The piston, accumulators, gun bushing and the gun barrel. To prepare for firing, the piston is pushed to the far end of the gun barrel. The striker is positioned as shown between the piston and the gun bushing. The accumulators are pressurized with nitrogen. The two o-rings on the piston prevent the gas from entering the gun barrel. To fire the gas gun, the piston is pushed forward by flowing nitrogen through the bleed hole in behind the piston. This flow is contrdled using a solenoid valve placed at the end of the bleed line so that the line can be fully charged before the valve is opened. Once the piston is pushed forward, the seal between the rear o-ring and the gun barrel is breached and the pressurized nitrogen in the accumulators enters the gun barrel. The expanding gas propels the piston along the length of the gun barrel until it impacts the end of the gun bushing. The piston then stops, releasing the striker to travel the length of the gun bushing where it will impact the incident bar. A soft buffer is placed between the piston and gun bushing to cushion the impact. After firing, the coupling nut is removed and the gun barrel is pulled off of the gun bushing so that the piston and striker can be pushed back into firing position. The sun barrel is mounted onto a rail system which allows the gun barrel to slide on and of the gun bushing so that the striker bar and piston can be repositioned [64].

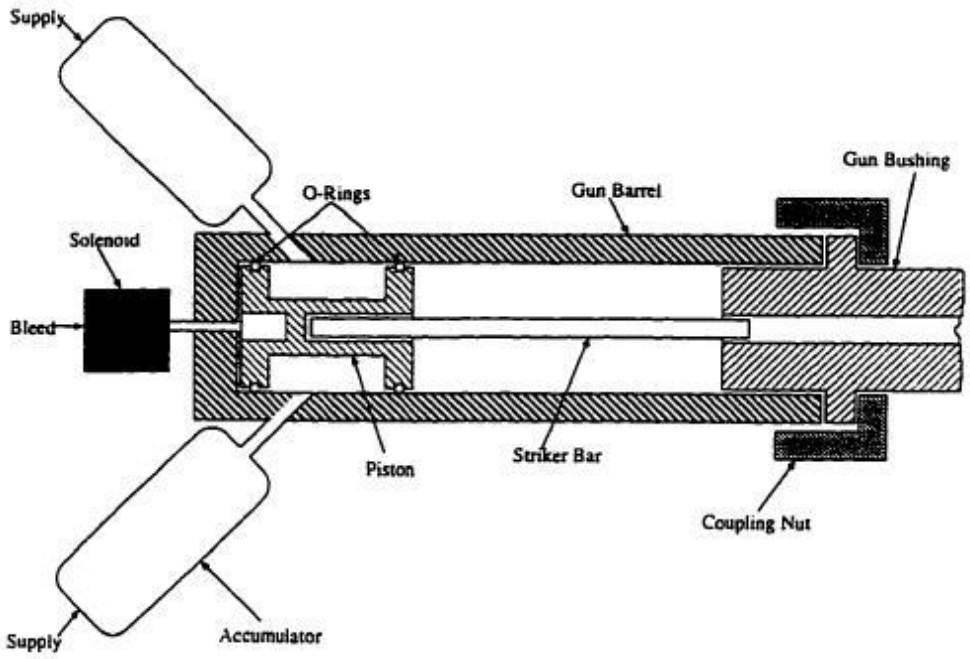

Figure 6.12 Gas gun system [64].

7. MATERIAL CHARACTERIZATION BY THE DATA OBTAINED FROM SPLIT HOPKINSON PRESSURE BAR EXPERIMENT

In this chapter, the material characterization by the data obtained from split Hopkinson pressure bar test and the fitting of Johnson-Cook constitutive equation is shown.

7.1. Forming the Stress-Strain Diagram

The figure below is a typical response of split Hopkinson pressure bar test. The tested material is copper [1].

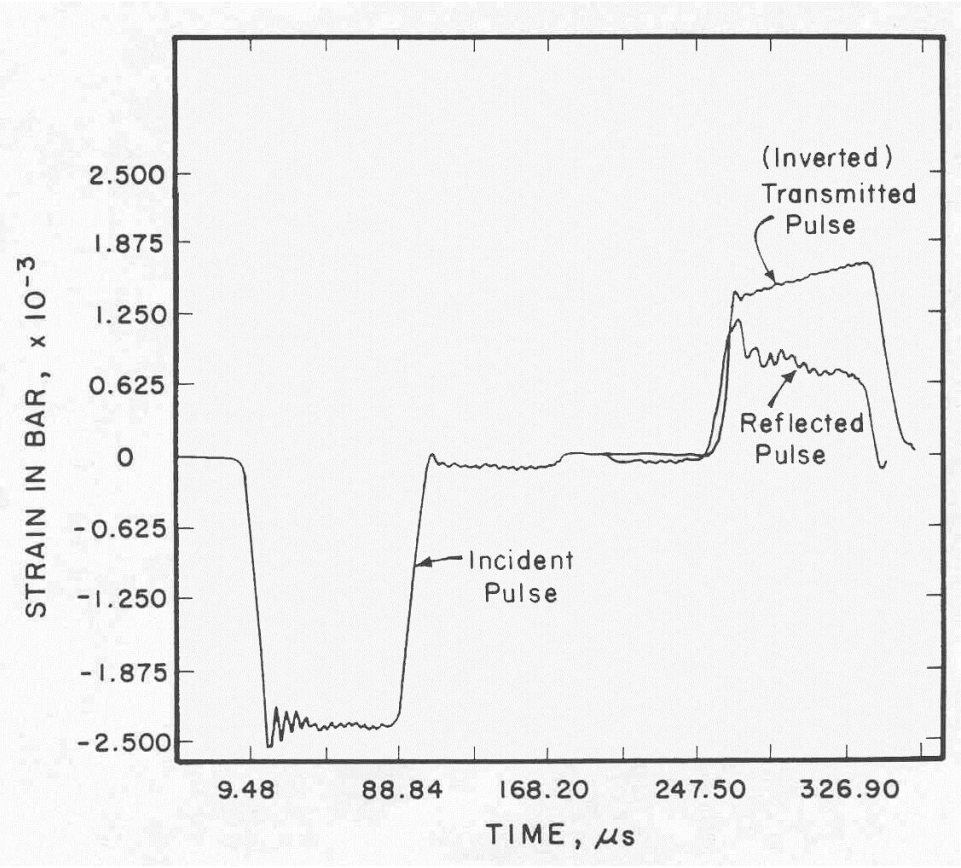

Figure 7.1 Split Hopkinson Pressure bar data for copper [1].

The bar and specimen dimensions with the mechanical properties are as follows:

Sample: Copper (E=130 GPa)

Compression bars: Maraging steel (E=210 GPa)

Sample diameter: 7.7 mm

Sample length: 10 mm

Density of Sample: 8.9 g/cm^3

Density of bars: 7.9 g/cm^3

Bar diameter: 12.7 mm

Firstly lets find the velocity of the elastic wave, C_0, in the bars;

$$C_0 = \sqrt{\frac{E_{bar}}{\rho_{bar}}} = \sqrt{\frac{210x10^9}{7900}} = 5160m/s$$

The areas of the bars and the specimen are as follows;

$$A_b = A_0 = \frac{\pi 12.7^2}{4} = 126.7x10^{-6}m^2$$

$$A_s = A = \frac{\pi 7.7^2}{4} = 47.4x10^{-6}m^2$$

Now lets take five points for a sample calculation of stress and strain:

Table 7.1. Sample points for determining stress-strain diagrams.

Point	Time (μs)	ε_R	ε_T
1	268,087	0,0013942	0,0010096
2	271,028	0,0014087	0,0008413
3	273,969	0,0014087	0,0009135
4	276,91	0,0014423	0,0008413
5	279,851	0,0014519	0,0007692

Referring to Equations 5.25 the stress and strain occurred in the specimen for the selected points can be calculated as follows. Note that, the integral value in the strain formulate is found by calculating the area under the reflected wave curve.

Table 7.2 Calculated stress-strain values.

Point	$\sigma = E(A_0 / A)\varepsilon_T(t)$ (MPa)	$\varepsilon(t) = -(2C_0 / L)\int_0^t \varepsilon_R dt$
1	481	0,03671237
2	486	0,04369075
3	486	0,05033539
4	498	0,05698002
5	501	0,06304818

The calculations were furthered to obtain the stress strain data for the copper and the following graph is found:

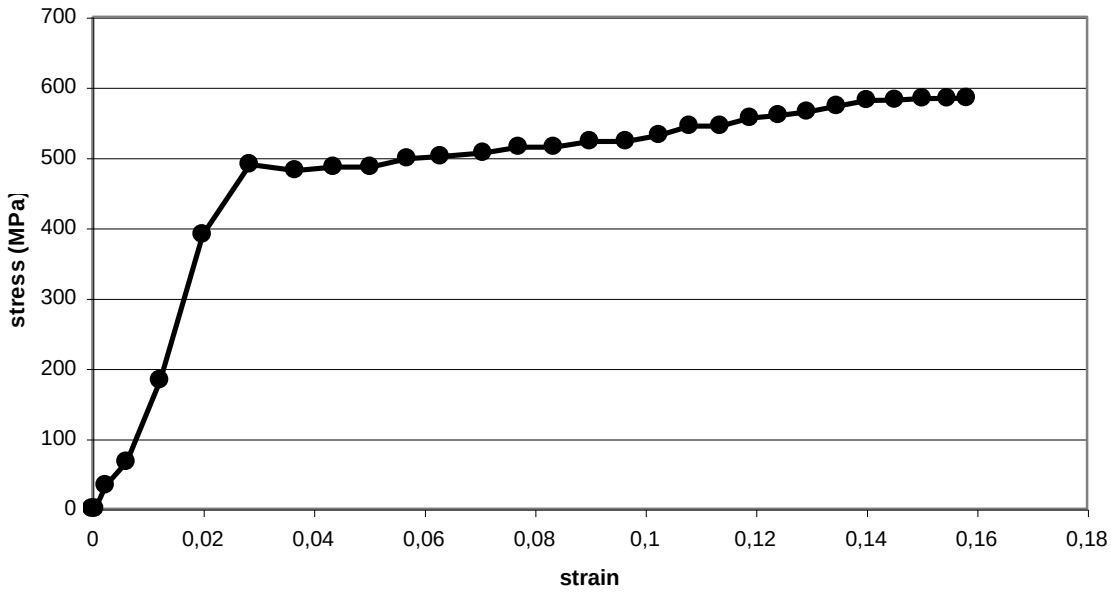

Figure 7.2 Stress-Strain curve obtained by the data from SHPB

7.2 Analysis of Stress-Strain Diagrams Obtained at Different Strain Rates and Temperatures

In this chapter the data taken from reference [25] is used. This stress-strain data is obtained with SHPB test for AISI 4340 steel, at different strain rates and temperatures by Lee and Yeh. The data is read from the graph in the paper and re-plot on the next page.

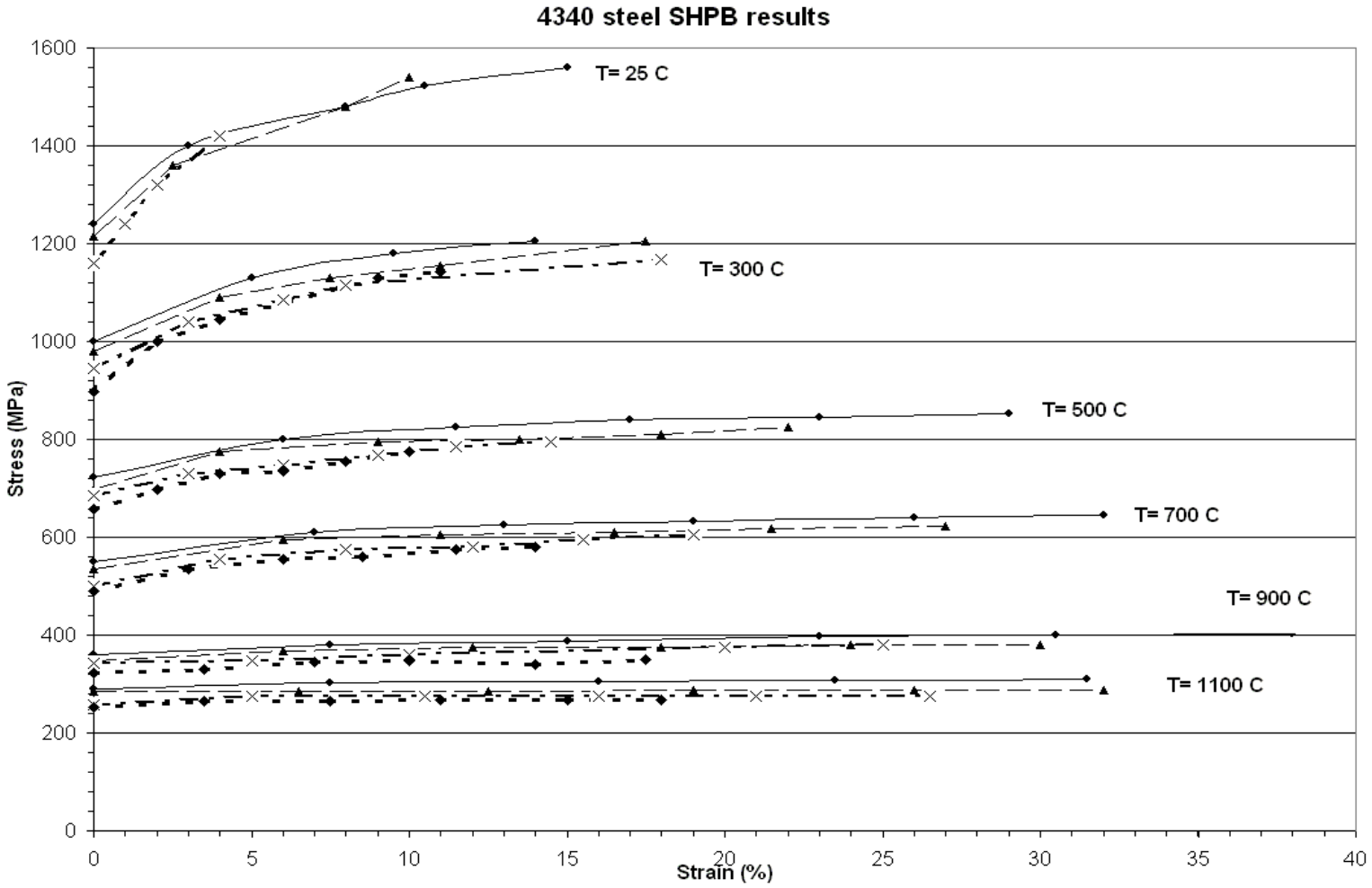

Figure 7.3 Stress-strain curves for AISI 4340 steel, obtained at different strain rates and temperatures with SHPB.

T (°C)	Strain rate (1/sn)			
	●	▲	X	◆
25	1531	1043	836	503
300	1954	1507	1109	716
500	2424	1891	1200	810
700	2715	2269	1631	1216
900	3216	2558	2114	1437
1100	3330	2718	2236	1583

7.3. Evaluation According to the Work Hardening Law

The stress-strain curves in Figure 7.3 can be described by a general empirical work-hardening law with different material constants, as proposed by Ludwik;

$$\sigma = A + B\varepsilon^n \qquad (7.1)$$

where A represents a constant, often yield strength; n is the strain-hardening exponent; and B is a proportional factor.

All the curves in Figure 7.3 are fitted to Equation 7.1 and constants are obtained. Firstly according to this model, the effects of the strain rate and temperature on the yield strength can be seen on Figure 7.4.

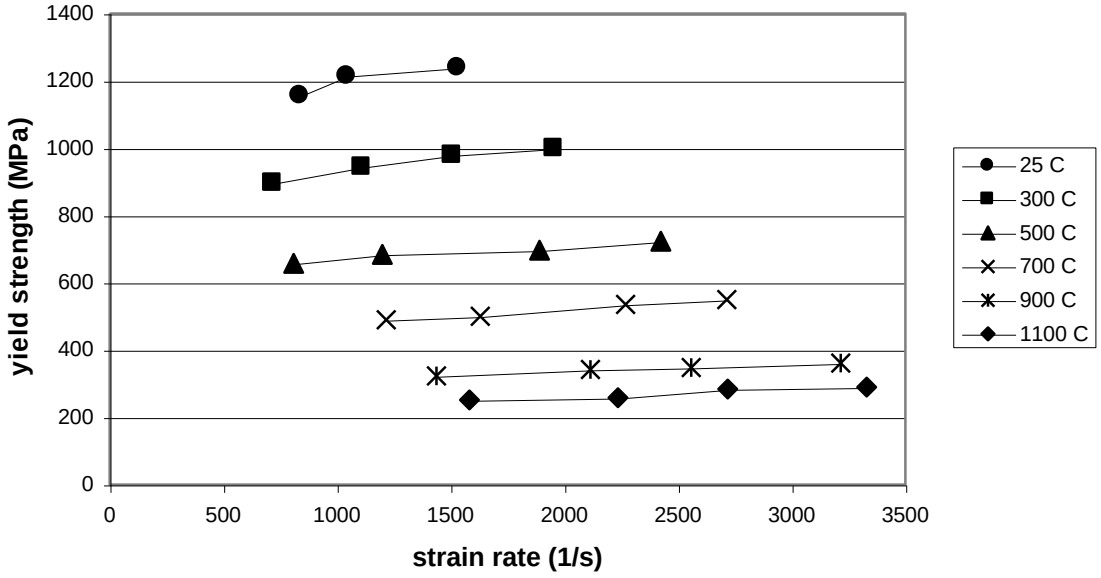

Figure 7.4 The variation of yield strength of AISI 4340 steel with strain rate for different test temperatures.

Secondly observing Figure 7.5, the material constant B tends to decrease with increase of the strain rate and temperatures except 900 and 1100°C. At room temperature constant B dramatically decreases with strain rate but at elevated temperatures it is independent of the strain rate.

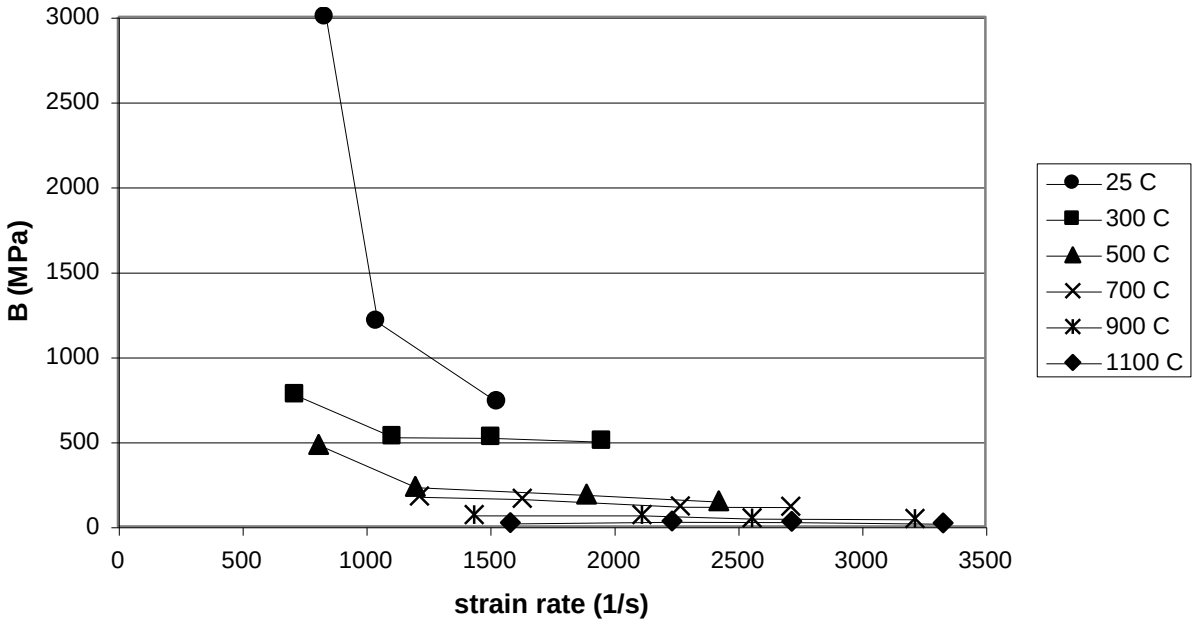

Figure 7.5 The variation of material constant B with strain rate for different test temperatures.

Finally, the variation of the strain-hardening exponent (n) with the strain rate can be seen at Figure 7.6.

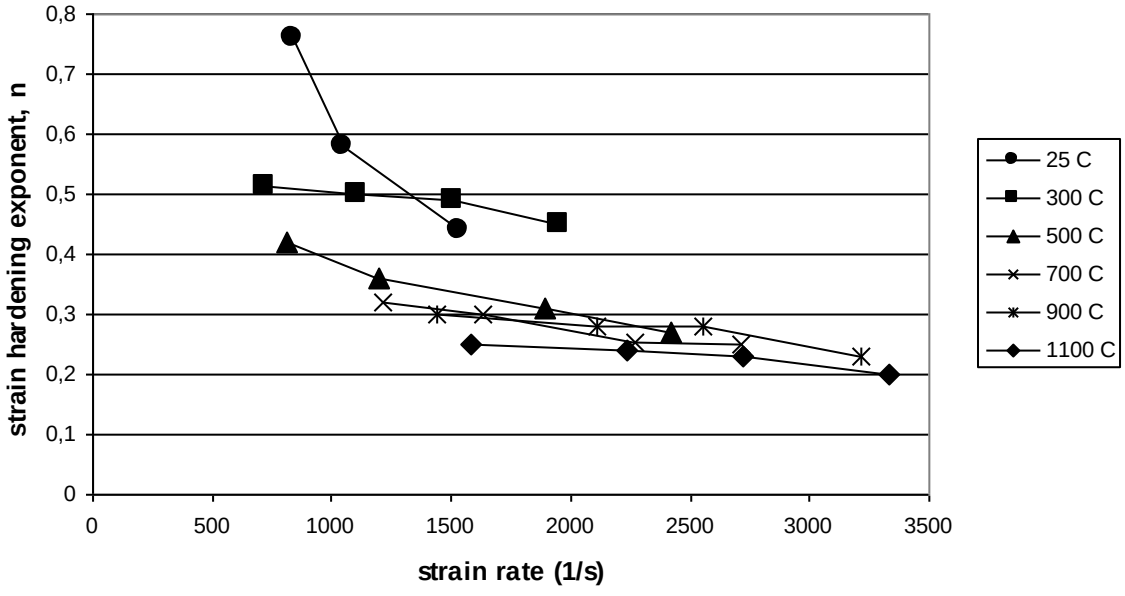

Figure 7.6 The variation of strain-hardening exponent, (n), with strain rate for different test temperatures.

7.4 Strain Rate Sensitivity

The dependence of flow stress on the strain rate can also be presented quantitatively by a parameter called the strain rate sensitivity. For a material deforming with athermal behavior, this value has a very low value, as explained in Chapter 3. The strain rate sensitivity, m, is defined as follows:

$$m = \frac{\ln(\sigma_1 - \sigma_2)}{\ln(\dot{\varepsilon}_1 - \dot{\varepsilon}_2)} \qquad (7.2)$$

From the data in Figure 7.3 the strain rate sensitivity variation with strain at 300° C and 900° C is obtained and can be seen in Figure 7.7 and 7.8.

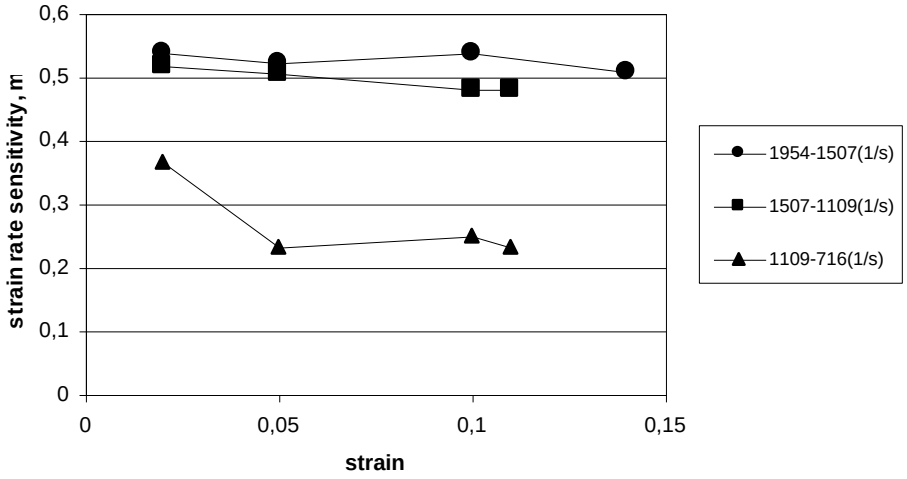

Figure 7.7 The variation of strain sensitivity with strain and strain rate at 300° C

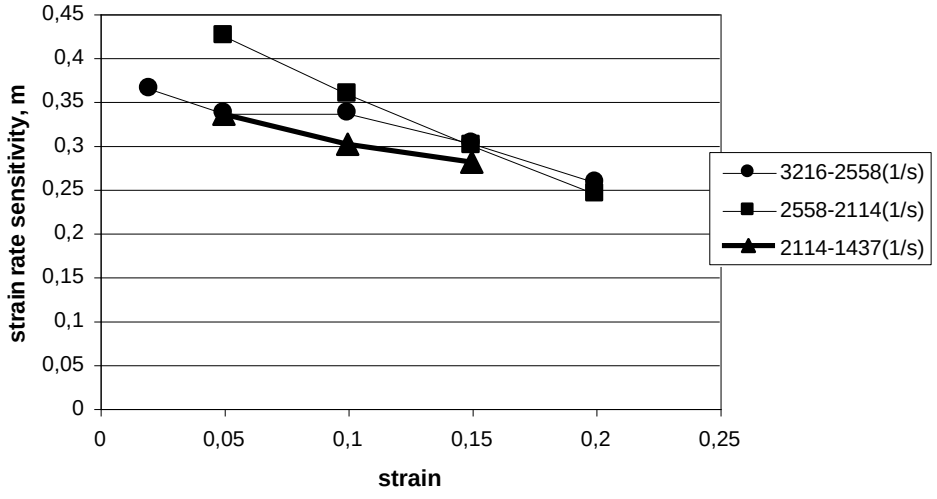

Figure 7.8 The variation of strain sensitivity with strain and strain rate at 900° C

7.5. Determining Johnson-Cook Equation Constants

The data taken from Figure 7.3 is fitted to Johnson-Cook deformation constitutive relation (Equation 4.2). The reference strain is taken as 504 /s and melting temperature of AISI 4340 is taken as 1473 K.

Non-linear regression analysis is used for data fitting. For this purpose there are several software available. However, NCSS 2001 is found to be the most suitable software, which can easily fit the data for a given equation.

The Johnson-Cook equation constants for AISI 4340 steel is found as follows;

A =1140 MPa

B = 634 MPa

n = 0.2731439

C = 0.02618754

m= 0.8884877

and, equation became as below;

$$\bar{\sigma} = (1140 + 634\bar{\varepsilon}_p^{\,0.273})(1 + 0.0262 \ln \dot{\varepsilon}^*)(1 - T_h^{\,0.8885})$$

According to the computed constants the error variation with strain can be seen in Figure 7.9. Note that ''residual'' refers to error, which is the difference between the measured and calculated stress.

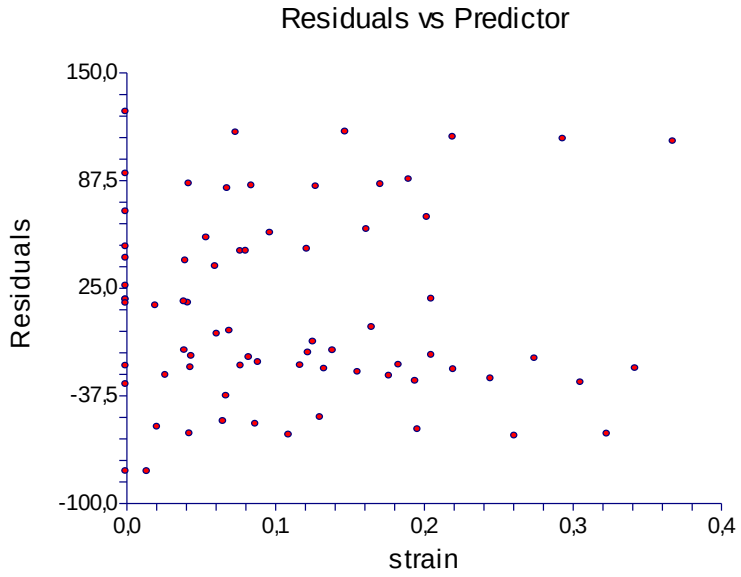

Figure 7.9 The variation of errors with strain according to the calculated constants.

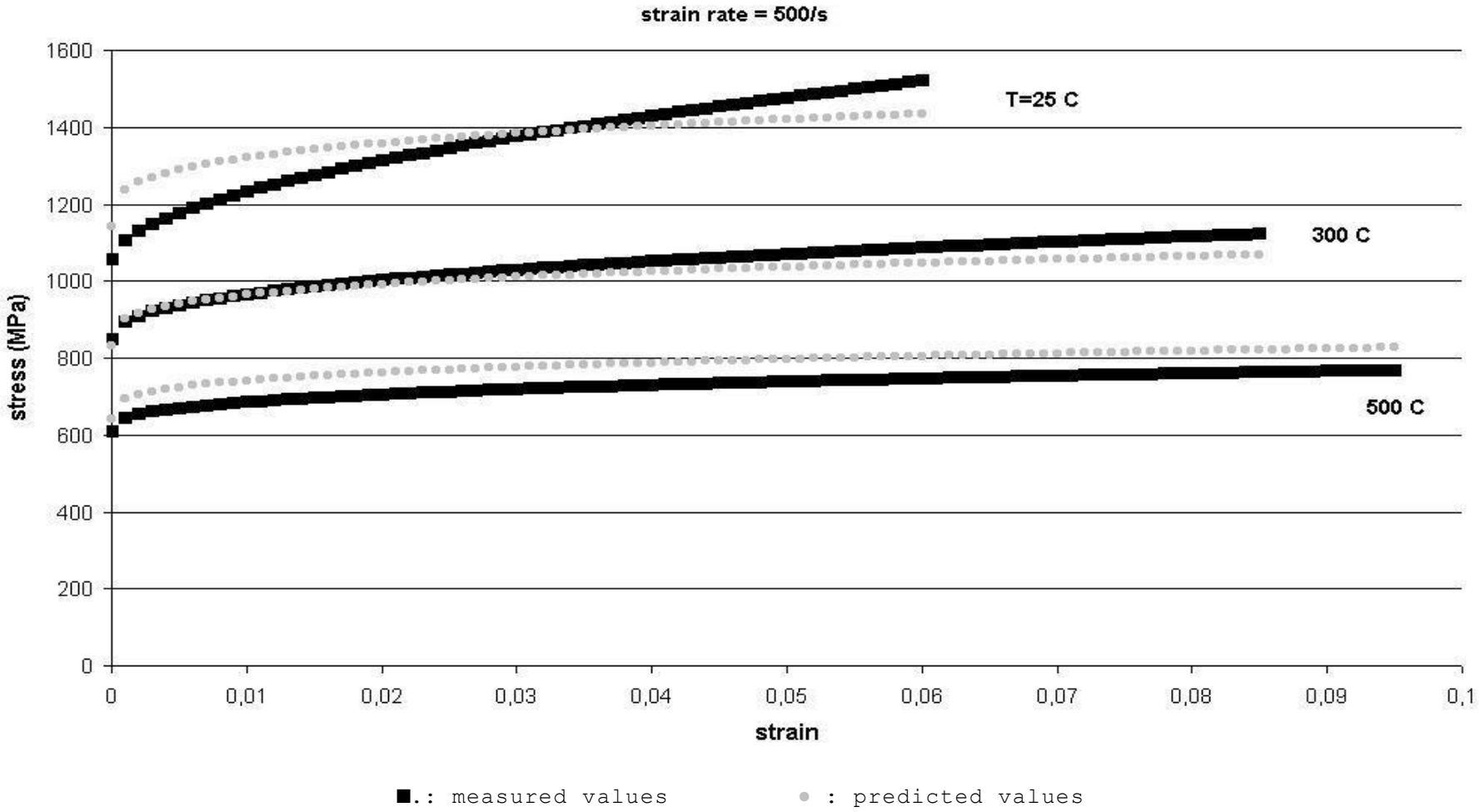
strain rate = 500/s
1600
1400
1200
1000
800
600
400
200
0
stress (MPa)
T=25 C
300 C
500 C
0
0,01
0,02
0,03
0,04
0,05
0,06
0,07
0,08
0,09
0,1
strain
■.: measured values
● : predicted values

Figure 7.10 The comparison of predicted and measured values for AISI 4340 steel deformed at a strain rate of 500 s^{-1}

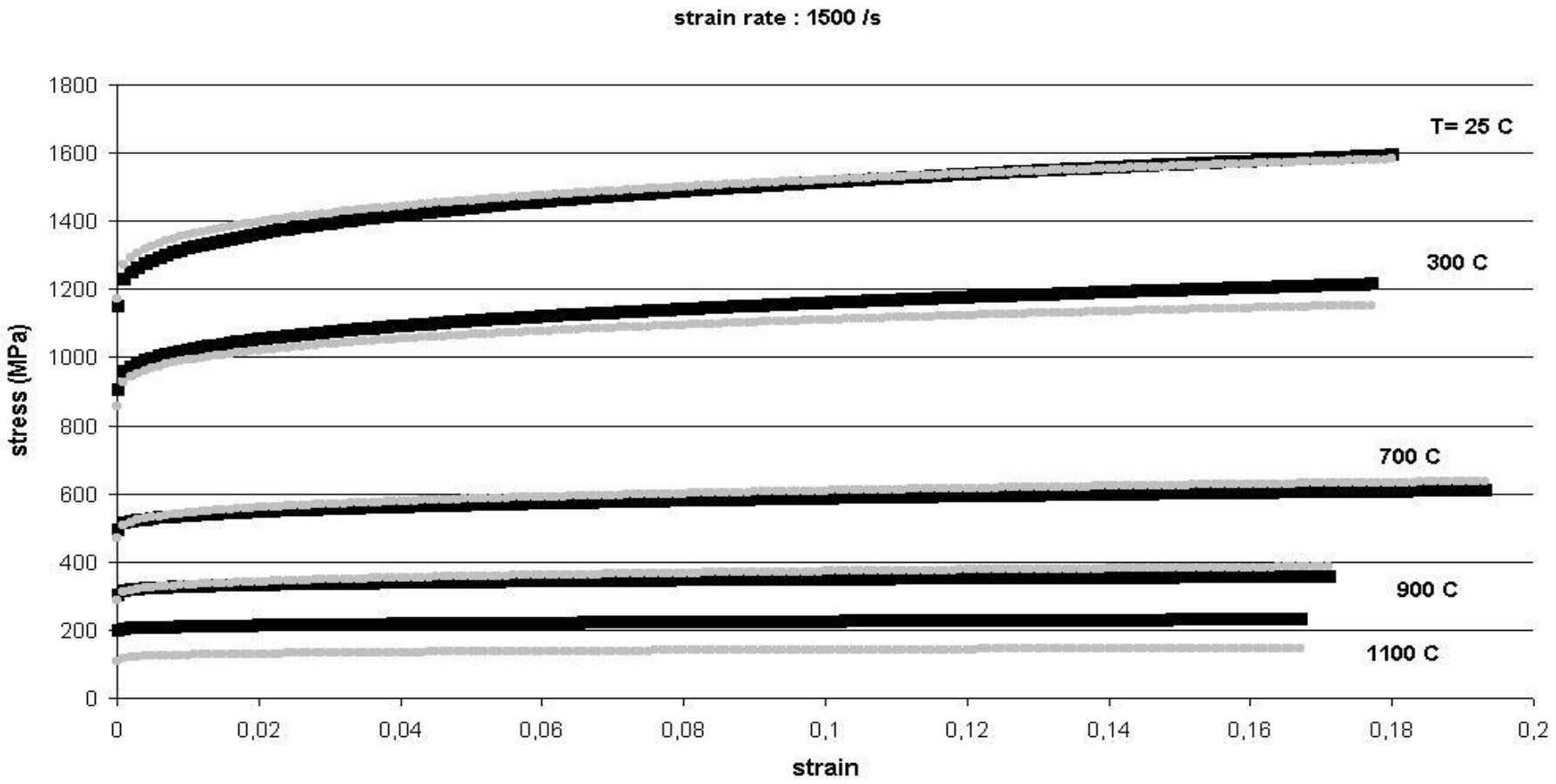

■.: measured values ● : predicted values

Figure 7.11 The comparison of predicted and measured values for AISI 4340 steel deformed at a strain rate of 1500 s^{-1}

The measured values and calculated values are plot below for observing the fitting clearance. From Figure 7.10, 7.11 and 7.12 the measured and calculated values for AISI 4340 steel at strain rates of 500 s^{-1}, 1500 s^{-1} and 2500 s^{-1} respectively, can be compared.

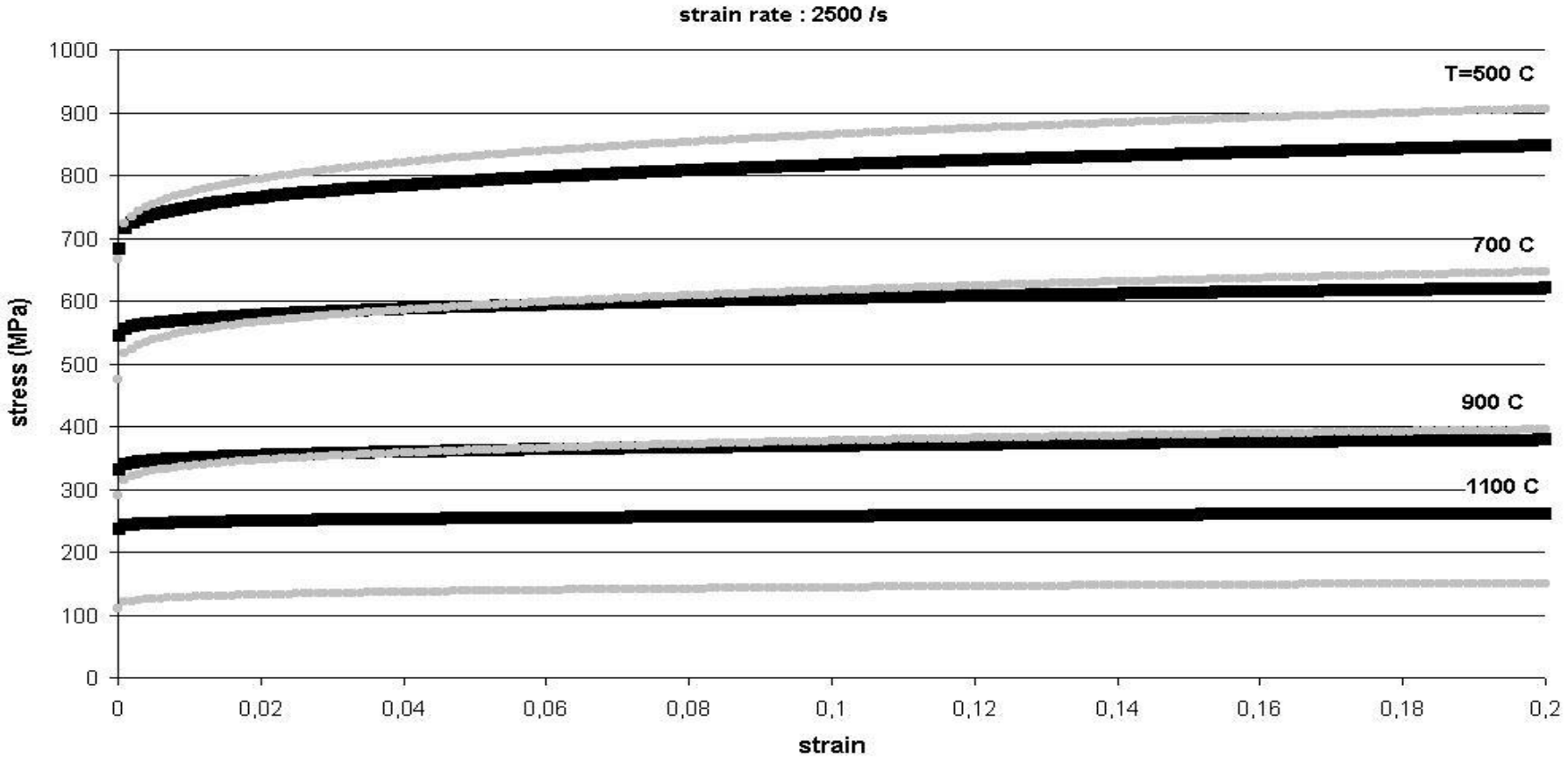

Figure 7.12 The comparison of predicted and measured values for AISI 4340 steel deformed at a strain rate of 2500 s^{-1}

8. APPLICATION OF JOHSON-COOK EQUATION IN A BALLISTIC PENETRATION PROBLEM

8.1. Definition of the Case Study

The aim of this case study is to observe the penetration of a ''bullet'' with a high velocity, namely 1000 m/s, to a ''target'' by Explicit Finite Element Analysis. Ansys7.0 LS-Dyna module is used for analysis. The geometries of the target and bullet (Figure 8.2) can be seen below

The major dimensions are as follows:

Table 8.1. The major dimensions in the model.

Bullet	Radius: 15 mm
Target	Radius: 100 mm
	Height: 5 mm
Distance between bullet and target:	15 mm

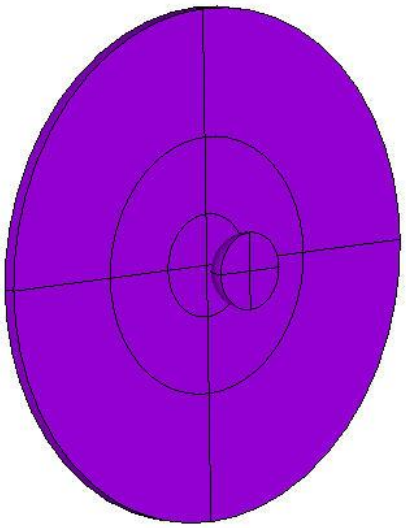

Figure 8.1 The bullet and the target.

8.2. Element Type and Meshing

Both the bullet and target are modeled in with 3-dimensional elements, namely SOLID 164. Also Mesh Facet 200 null element is used for uniform meshing. Firstly the base geometries are created and meshed with MESH 200 (Figure 8.2), and then these 2-D models are rotated by the axis (Figure 8.3). The 3-D meshed model of the bullet and target is obtained by replacing the Mesh Facet element by SOLID 164 element during rotation.

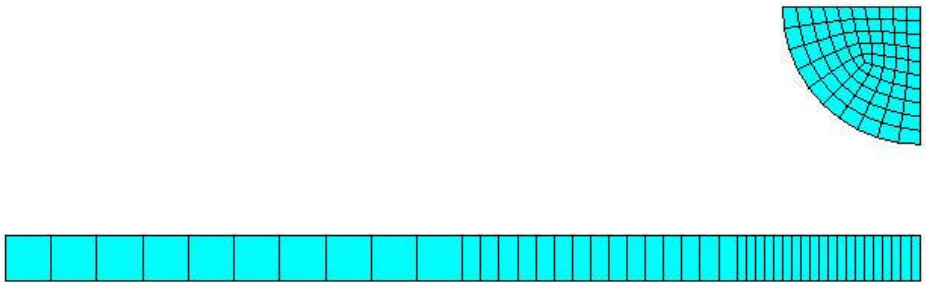

Figure 8.2 The 2-D model meshed with Mesh Facet Element.

There are 5453 nodes and 3840 elements in the model. In the first analysis, the thickness of the target is meshed with one element. In further analysis, the height of the target is divided into three elements.

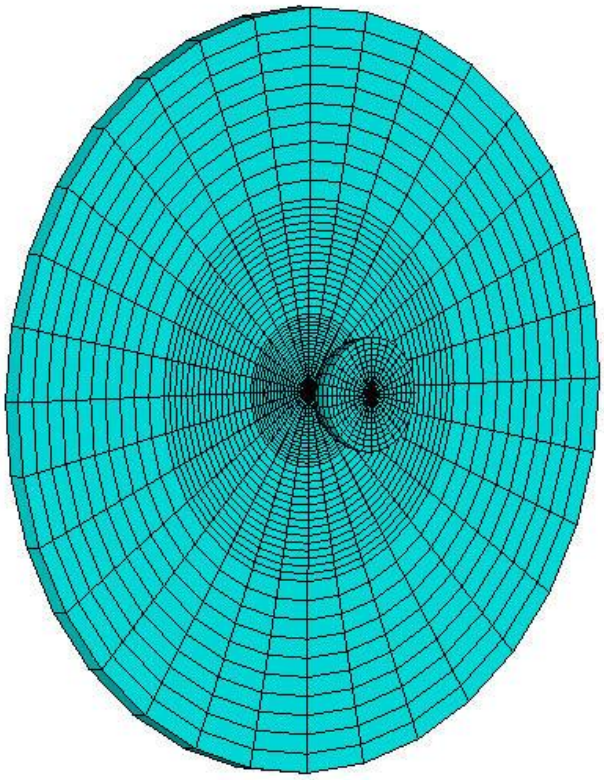

Figure 8.3 The bullet and target meshed with SOLID 164 element.

8.3. Material Model, Failure Criteria, and Contact

AISI 4340 steel is selected as the material of bullet and target. Plastic kinematic hardening material model and Johnson-Cook material models are used to simulate the behavior of bullet and target, respectively. LS-Dyna has these models readily and the material constants, which can be seen in Table 8.2 and 8.3 are used.

Table 8.2 Plastic kinematic hardening material model constants for AISI 4340 steel [72]

Modulus of Elasticity (MPa)	210000
Density (kg/ m^3)	7850
Poisson Ratio	0.3
Yield Stress (MPa)	792
Tangent Modulus (MPa)	21000
Strain Rate Parameter (C)	40
Strain Rate Parameter (P)	5
Failure strain	0.15

Table 8.3. Johnson-Cook material model constants for AISI 4340 steel [72]

Modulus of Elasticity (MPa)		210000	**Fracture model constants**	D_1	-0.8
Density (kg/ m^3)		7850		D_2	2.1
Poisson Ratio		0.3		D_3	-0.5
Deformation model constants	**A (MPa)**	910		D_4	0.002
	B (MPa)	586		D_5	0.61
	C (MPa)	0.014	**Mie-Gruneisen constants**	S_1	164
	n	0.26		S_2	294
	m	1.03		S_3	500
				γ_0	1.16

In both two models, when the critical value is reached, the damaged elements are removed from mesh. The critical value for plastic kinematic hardening model is the failure strain. When the equivalent plastic strain reaches the value of 0.15, failed elements are removed from mesh.

In Johnson-Cook material model fracture constants and the following cumulative damage law are used to simulate failure.

$$D = \sum \frac{\Delta \varepsilon}{\varepsilon_p} \qquad [8.1]$$

where,

$$\varepsilon_f = \left[D_1 + D_2 \exp\left(D_3 \sigma^*\right)\right]\left[1 + D_4 \ln \varepsilon^*\right]\left[1 + D_5 T^*\right] \qquad [8.2]$$

where $\Delta\varepsilon$ is the increment of effective plastic train during an increment in loading and σ^* is the mean stress normalized by the effective stress. The parameters D_1, D_2, D_3, D_4, and D_5 are the fracture constants. When D=1, the elements failed and removed from the mesh.

In the analysis, the ''eroding'' and ''failure with tied nodes'' surface to surface contact algorithm is used to simulate contact between bullet and target.

8.4. Constraints and Initial Velocity

The lateral surface of the target is constrained by setting all degrees of freedom to zero. Also 500 m/s and 1000 m/s of initial velocity is applied to the bullet during the analysis.

8.5. Some Results

Some of the results obtained with the initial velocity can be seen in Figure 8.5 and 8.6. Figure 8.5 is the model with a mesh with three elements thorough the thickness; the initial velocity of the bullet is 500 m/s, and the time is 85 μs.

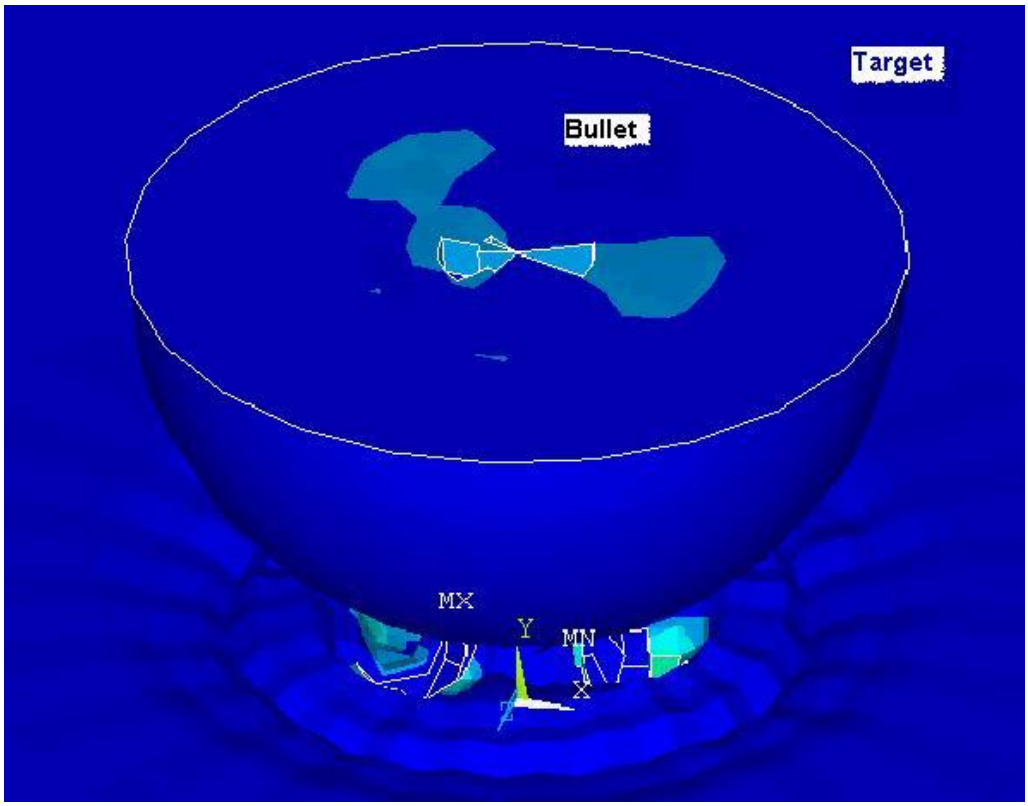

Figure 8.4 The plastic strain distribution at time 85 μs with a bullet speed of 500 m/s.

Figure 8.6 is the model with a mesh with one element thorough the thickness; the initial velocity of the bullet is 1000 m/s, and the time is 56 μs.

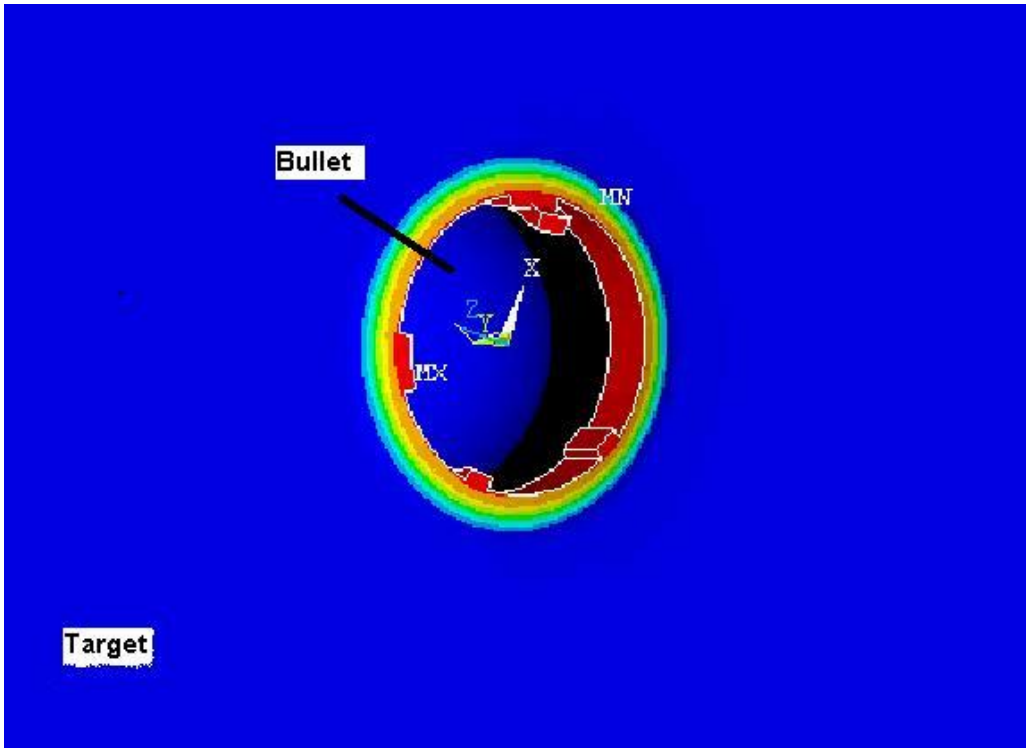

Figure 8.5 The stress distribution at time 56 μs with a bullet speed of 1000 m/s.

In this chapter, only the applied study is explained for further knowledge on explicit finite element analysis reader can refer to [14, 65-70].

9. CONCLUSIONS

9.1. Conclusions

The following are the major conclusions made from the present research:

- When the strain rate of the deformation is high (>100 s^{-1}), the deformation becomes dynamic. Therefore, stress waves should be taken into account in order to understand and explain the behavior of solids.

- At high strain rates and various temperatures, deformation mechanisms change. Long and short-range barriers are the major barriers at strain rates lower than ~3500 s^{-1}. Above this rate phonon drag mechanisms came into play. Above than strain rates of 10^7 s^{-1}, the effects of dislocations on deformation mechanisms diminish and lattice itself became important. This different mechanisms affects the mechanical properties of materials. The resistance of material against plastic deformation increases with the increasing strain rate.

- The split Hopkinson Pressure Bar facility can be used to test materials at different strain rates (between 500 - 10^4 s^{-1}) and temperatures and to obtain corresponding stress-strain diagrams.

- Two major assumptions should be satisfied during the design of the split Hopkinson pressure bar apparatus. First one is to ensure one-dimensional elastic wave propagation, which is related to dimensions and alignment of the bars and specimen. The second one is to ensure the uniform deformation at the specimen, which is related to initial wavelength and the rise time of the wave.

- Johnson-Cook constitutive equation with the computed parameters by non-linear regression analysis gave good agreement between measured and predicted values of flow stress of AISI 4340 steel.

- Zerilli-Armstrong constitutive equation gave very bad agreement with the measured values.

- LS-Dyna can be used to model the ballistic penetration of a bullet to a target. • In modeling ballistic penetration meshing uniformity, finer meshing and contact algorithms should be well studied. **The Topics which have not been Realized Yet**

There are three topics, which were not realized due to lack of economical issues and knowledge. The first is that, the application and construction of split Hopkinson pressure bar facility couldn't be made. Secondly the design of gas gun system couldn't realized, however two gas gun systems proposed. The last is that, Accurate results for ballistic penetration cannot be obtained. **Recommendations for Further Studies**

The following recommendations are proposed on the findings of the present research:

- The split Hopkinson pressure bar apparatus should be constructed with the given design to realize tests.
- A gas gun system should be designed in order to create an incident wave.
- The topic of shear band mechanism and dynamic fracture should be studied in order to model the behavior and mode of fracture at high strain rates.
- The split Hopkinson bar apparatus should be rearranged to observe shear band localization phenomena.
- A numerical solution can be made to validate the results of split Hopkinson pressure bar test.
- A more accurate validation can be made by conducting high velocity penetration experiments and comparing the results with the numerical solutions by the deformation behavior of material obtained from split Hopkinson pressure bar test.
- For later studies, shock waves should be studied.
- For later studies, an original constitutive equation related to both deformation and fracture behavior of the desired material should be created.
- Ballistic penetration modeling using Finite Element Analysis should be furthered and accurate results should be realized.

REFERENCES

[1] **Meyers, M.A,** 1994. Dynamic Behavior of Materials, John Wiley&Sons.

[2] **Kolsky, H,** 1953. Stress Waves in Solids, Oxford, Clarendon Press.

[3] **Karman T., Duwez P.**, 1950, Journal of Applied Physics, **21**, 987.

[4] **Kinslow R. Ed.,** 1970. High- Velocity Impact Phenomena, Academic Press, New York.

[5] **Cristescu, N,** 1967. Dynamic Plasticity, North-Holland Publishing Comp.

[6] **Murr, L.E, Staudhammer, K.P., Meyers, M.A**, 1986. Metallurgical applications of shock-wave and high-strain-rate phenomena, Marcel Dekker Inc., New York and Basel.

[7] **Chen, Y.,** 1998. High-Strain, High-Strain Rate Deformation of Tantalum; *PhD Thesis*, University of California, San Diego.

[8] **Lennon, A.M,** 1998. Rate-Dependent Thermomechanical Behavior and Shear Localization in a BCC material, *PhD Thesis*, The John Hopkins University, Maryland.

[9] **Stevenson, M.E,** 2001. Grain Size Effects on the High Strain Rate Deformation of Copper, *PhD Thesis*, The University of Alabama, Alabama.

[10] **W.G. Ferguson, A. Kumar, and J.E. Dorn,** 1967. *Acta Metall*, **38**, 1863-1869.

[11] **Blazynski, T.Z,** 1987. Materials at high strain rates, Elsevier Applied Science, London and New York.

[12] **Lindholm, U.S,** 1964. Some Experiments with the split Hopkinson Pressure Bar, *J. Mech. Phys. Solids*, **12**, 317-335.

[13] **Regazzoni, G, Kokcs, U.F., Follansbee, P.S,** 1987. Dislocation Kinetics at High Strain Rates, *Acta Metall*, **35**, No.12, 2865-2875.

[14] **Espinoza H.D, Zavattieri, P.D, Emore, G.L,** 1998. Adaptive FEM computation of geometric and material nonlinearities with application to brittle failure', *Mechanics of Materials*, **29**, 275-3305.

[15] **Clifton, R.J.,** 1990. High strain rate behavior of metals, *Applied Mechanical Revolutions*, **43**, No.5, Part 2, S9-S22.

[16] **Meyers, M.A, Benson, D.J., Vöhringer, O., Kad, B.K, Xue, Q., Fu, H,** 2002. Constitutive description of dynamic deformation: physically-based mechanisms, *Materials Science and Engineering*, A 322, 194-216.

[17] **Liang, R., Khan, A.S,** 1999. A critical review of experimental results and constitutive models for BCC and FCC metals over a wide range of strain rates and temperatures, *International Journal of Plasticity*, **15**, 963-980.

[18] **Armstrong, R W, Zerilli, F.J.,** 1995. Finite Deformation Plasticity, *Proc. of ASME Materials Division*, ASME, **69-I**, 417-428.

[19] **Rosenfield, A R, Hahn, G T., Bement, A L., Jaffee, R I.**, 1968. Dislocation Dynamics, McGraw-Hill, NY

[20] **Redford, D D.,** 2000. Mechanical and Constitutive Behavior of Zr-2.5 Nb Pressure Tube **Material** at High Rates of Tensile Strain, Carleton University, Canada.

[21] **Lee, W, Lin, C,** 1998. Plastic deformation and fracture behaviour of Ti-6Al-4V alloy loaded with high strain rate under various temperatures, *Materials Science and Engineering*, **A241**, 48-59.

[22] **Lee, W, Lin, C,** 1998, High-temperature deformation behaviour of Ti 6Al 4V alloy evaluated by high strain-rate compression tests, *Journal of Materials Processing Technology*, **75**, 127-136.

[23] **Rule, W K,** 1998. A revised form for the Johnson-Cook strength model, *International Journal of Impact Engineering*, **21**, No. 8, 609-624.

[24] **Lee, W, Lin, C,** 2001. Impact properties and microstructure evolution of 304L stainless steel, *Materials Science and Engineering*, **A308**, 124-135.

[25] **Lee, W, Yeh, G,** 1997. The plastic deformation behaviour of AISI 4340 alloy steel subjected to high *temperature* and high strain rate loading conditions, *Journal of Materials Processing Technology*, **71**, 224-234.

[26] **Noble, J. P., et. al.,** 1999. The use of Hopkinson bar to validate constitutive relations at high *rates* of strain, *Journal of the Mechanics and Physics of Solids*, **47**, 1187-1206.

[27] **Lee, W, Lam, H,** 1996. The deformation behavior and microstructure evolution of high-strength alloy steel at high rate of strain, *Journal of Materials Processing Technology*, **57**, 233-240.

[28] **Picu, R C, Majorell, A,** 2002. Mechanical behavior of Ti-6Al-4V at high and moderate temperatures- Part II: constitutive modeling, *Materials Science and Engineering*, **A326**, 306-316.

[29] **Macdougall, D A S Harding, J.,** 1999. A constitutive relation and failure criterion for Ti 6Al 4V alloy at impact rates of strain, *Journal of the Mechanics and* Physics *of Solids*, **47**, 1157-1185.

[30] **Staker, M R**, Introduction to High Strain Rate Testing, *Metals Handbook*, **8**, 3rd edition.

[31] **Kolsky, H,** 1949. An Investigation of the Mechanical Properties of Materials at very High Rates of Loading, *Proc. Phys. Soc.*, **62B**, 676-700.

[32] Review of Experimental Techniques for High Rate Deformation Studies, *http://www.etca.fr/dymat/html/highstrain.html*.

[33] **Davies E D H, Hunter S C,** 1963. The Dynamic Compression Testing of Solids by the Method of the Split Hopkinson Pressure Bar, *J. Mech. Phys. Solids*, **11**, 155-179.

[34] **Follansbee, P. S**, High Strain Rate Compression Testing, *Metals Handbook*, **8**, 3rd edition.

[35] **Ogawa, K,** 1984. Impact-tension Compression Test by Using a Split Hopkinson Bar, Experimental *Mechanics*, June, 81-86.

[36] **Follansbee, P. S, Frantz, C,** 1983. Wave propagation in the Split Hopkinson Pressure Bar, *Journal of* Engineering *Materials and Technology*, **105**, 61-66.

[37] **Bodner, S. R, Aboudi, J.,** 1983. Stress Wave Propagation in Rods of Elastic-Viscoplastic Material, *Int. J. Solids Structures*, **19**, 305-314.

[38] **Jones, O. E, Norwood, F. R,** 1967. Axially Symmetric Cross-Sectional Strain and Stress **Distributions** in Suddenly Loaded Cylindrical Elastic Bars, *Transactions of the ASME*, September, 718-724.

[39] **Bodner, S. R, Clifton, R. J.,** 1967. An Experimental Investigation of Elastic-Plastic Pulse Propagation in Aluminum Rods, *Journal of Applied Mechanics*, March, 91-99.

[40] **Berthdlf, L. D,** 1967. Numerical Solution for Two-Dimensional Elastic Wave Propagation in Finite Bars, *Journal of Applied Mechanics*, September, 725-734.

[41] **Zhao, H, Gary, G,** 1995. A three dimensional analytical solution of the longitudinal wave propagation in an infinite linear viscoelastic cylindrical bar. Application to experimental techniques, *Journal of the Mechanics and Physics of Solids*, **43**, No. 8, 1335-1348.

[42] **Gilat A, Cheng C,** 2002. Modeling torsional split Hopkinson bar tests at strain rates above 10000 s^{-1}, *International Journal of Plasticity*, **18**, 787-799.

[43] **Meng, H, Li, Q M,** 2003. Correlation between the accuracy of a SHPB test and the stress uniformity based on numerical experiments, *International Journal of Impact Engineering*, **28**, 537-555.

[44] **Zhao, H,** 2003. Material behavior characterization using SHPB techniques, tests and simulations, Computer *and Structures*, **81**, 1301-1310.

[45] **Gorham, D. A,** 1989. Specimen inertia in high strain-rate compression, *Journal of Physics D* Applied *Physics*, **22**, 1888-1893.

[46] Hopkinson split bar, *http://web.tut.fi/units/ms/elmlaitteet/hopkinson (eng).htm*

[47] High Strain Rate Laboratory / Split Hopkinson Pressure Bar, *http://www.me.mtu.edu/~subbash/*

[48] Split Hopkinson Bar Facility, *http://diva.me.gatech.edu/facilities/hopbar2.shtml*

[49] **Ellwood, S,** Griffiths, **L. J., Parry, D. J.,** 1982. Materials testing at high constant strain, *Journal of Physics E: Scientific Instrumentation*, **15**, 280-282.

[50] **Ferreira, F. J., Vaz, M. A., Simoes J. A,** The role of specimen geometry for accurate characterization of bone properties using Split

Hopkinson Pressure Bar, *www.demist.utl.pt/~bonemec/ABSTRACT-ferreira_vaz_simoesl.pdf*

[51] **Zhao, H, Gary, G,** 1997. A New Method for the Seperation of Waves. Application to the SHPB Technique for an Unlimited Duration of Measurement, *J. Mech. Phys.* Solids., **45**, 1185-1202.

[52] **Pryzbylo, P. A,** 1999. Experimental Investigation and Constitutive Modeling of Rubbery Polymers, *PhD* Thesis, University of Michigan, Michigan.

[53] **Wilkins M.L.,** Gunian **M. W,** 1973. Impact of Cylinders on a Rigid Boundary, *Journal of Applied Physics*, **44**, 1200-1206.

[54] **Grady, D.E., Benconi, D.A,** 1983. Fragmentation of Metal Rings by Electromagnetic Loading, *Experimental Mechanics*, **28**, 393-400.

[55] **Oosterkamp, L.D., Ivankovic, A., Venizelos G.,** 2000. High strain rate properties of **selected** aluminnium alloys, *Materials Science and Engineering*, **A278**, 225-235.

[56] **Bassim, M.N., Panic, N.,** 1999. High strain rate effects on the strain of alloy steels, *Journal of* **Materials** *Processing Technology*, **92-93**, 481-85.

[57] **Lennon, A.M., Ramesh, K.T.,** 1998. A technique for measuring the dynamic behavior of materials at high temperatures, *International Journal of Plasticity*, **14**, No. 12, 1279-1292.

[58] **Lee, W., Sue W., Lin, C., Wu, C.,** 2000. The strain rate and temperature dependence of the dynamic impact properties of 7075 aluminum alloy, *Journal of Materials Processing Technology*, **100**, Issues 1-3, 116-122.

[59] **Lee, W., Sue, W., Lin, C.,** 2000. The effects of temperature and strain rate on the properties of carbon-fiber-reinforced 7075 aluminum alloy metal-matrix composite, *Composite Science and Technology*, **60**, 1975-1983.

[60] **Pintado, C., Pedraza, C., Castillo, J.M., Benitez, F.G.,** 2001. Experimental investigation of the dynamic response of graphite-epoxy composite laminates under compression, *Composite Structures*, **53**, 493-497.

[61] **Bragov, A.M., Lomunov, A.K.,** 1995. Methodological aspects of studying dynamic material properties using the Kolsky Method, *International Journal of Impact Engineering*, **16**, 321-330.

[62] **Walton, F.S.,** 1997. Adiabacity of High Strain Rate Compression Testing Using the Split Hopkinson Pressure Bar Apparatus, *Msc Thesis*, University of Lethbridge, Canada.

[63] ''Shocking Gas gun Experiments'', Lawrence Livermore National Laboratory, September 2000.

[64] **Mason, R.M.,** 1997. Prediction of Adiabatic Shear in 4340 Steel, Remco and Armco Irons, *Msc* Thesis, Carleton University, Canada.

[65] **Warren, T.L., Tabbara, M.R.,** 2000. Simulations of the penetration of 6061-T6511 aluminum targets by spherical-nosed VAR 4340 steel

projectiles, *International Journal of Solids and Structures*, **37**, 4419-4435.

[66] **Anderheggen, E., Renau-Munoz, J.F.,** 2000. A parallel explicit solver for simulating impact and penetration of a three-dimensional body into a solid substrate, *Advances in Engineering Software*, **31**, 901-911.

[67] **Borvik, T., Langseth, M., Hopperstad, O.S., Malo, K.A.,** 2002. Perforation of 12 mm thick steel plates by 20 mm diameter projectiles with flat, hemispherical and conical noses Part I: Experimental study, *International Journal of Impact Engineering*, **27**, 19-35.

[68] **Borvik, T., Langseth, M., Hopperstad, O.S., Malo, K.A.,** 2002. Perforation of 12 mm thick steel plates by 20 mm diameter projectiles with flat, hemispherical and conical noses Part II: Numerical simulations, *International Journal of Impact Engineering*, **27**, 37-64.

[69] **Simha, C.H.M., Bless, S.J., Bedford, A.,** 2002. Computational modeling of the penetration response of a high-purity ceramic, *International Journal of Impact Engineering*, **27**, 65-86.

[70] **Borvik, T et al.,** 1999. Ballistic Penetration of Steel Plates, *International Journal of Impact Engineering*, **22**, 855-886.

[71] **Meng, H., Li, Q.M.,** 2003. An SHPB set-up with reduced time-shift and pressure bar length, *International Journal of Impact Engineering*, **28**, 677-696.

[72] **Buyuk, M. Kurtaran, H.,** 2003. The effect of material model selection on ballistic impact simulations, *Int. Conf. on the Mech. Behavior of Materials*, **May 25-29**

CURRICULUM VITAE

Emre Ozlu was born on June 1978 in Duzce. His parents Ayse and Ilhan Ozlu raised him in Duzce then where he graduated from Duzce Arsal Anatolian High School in 1996. He entered the Department of Mechanical Engineering at Istanbul Technical University in the fall of 1997. In the fall of 2001 he received his Bachelor of Science in Mechanical Engineering. Immediately following his undergraduate work, Emre continued his education in the masters program at ITU in the Manufacturing Master's Program as a teaching assistant.